

(NASA-SP-290-Vol-3) TURBINE DESIGN AND  
APPLICATION, VOLUME 3 (NASA) 141 P MFT  
\$2.25; SOD HC \$2.10 CSCL 213

N75-24741

G3/C7 25357

Unclass



NATIONAL AERONAUTICS AND SPACE ADMINISTRATION





# TURBINE DESIGN and APPLICATION

VOLUME THREE

Edited by Arthur J. Glassman  
*Lewis Research Center*

U.S. GOVERNMENT PRINTING OFFICE  
1975  
6-15



Scientific and Technical Information Office  
1975  
NATIONAL AERONAUTICS AND SPACE ADMINISTRATION  
Washington, D.C.

---

For sale by the Superintendent of Documents  
U.S. Government Printing Office, Washington, D.C. 20402  
Price \$2.10 Stock Number 3300-00568  
*Library of Congress Catalog Card Number 79-185105*

## PREFACE

NASA has an interest in turbines related primarily to aeronautics and space applications. Airbreathing turbine engines provide jet and turboshaft propulsion, as well as auxiliary power for aircraft. Propellant-driven turbines provide rocket propulsion and auxiliary power for spacecraft. Closed-cycle turbine engines using inert gases, organic fluids, and metal fluids have been studied for providing long-duration electric power for spacecraft. Other applications of current interest for turbine engines include land-vehicle (cars, trucks, buses, trains, etc.) propulsion power and ground-based electrical power.

In view of the turbine-system interest and efforts at Lewis Research Center, a course entitled "Turbine Design and Application" was presented during 1968-69 as part of the In-House Graduate Study Program. The course was somewhat revised and again presented in 1972-73. Various aspects of turbine technology were covered including thermodynamic and fluid-dynamic concepts, fundamental turbine concepts, velocity diagrams, losses, blade aerodynamic design, blade cooling, mechanical design, operation, and performance.

The notes written and used for the course have been revised and edited for publication. Such a publication can serve as a foundation for an introductory turbine course, a means for self-study, or a reference for selected topics. The first volume presented the material covering thermodynamic and fluid-dynamic concepts, fundamental turbine concepts, and velocity diagram design. The second volume presented the material related to blade aerodynamic design and turbine energy losses. This third, and last, volume presents chapters on supersonic turbines, radial-inflow turbines, turbine cooling, and aerodynamic performance testing.

Any consistent set of units will satisfy the equations presented. Two commonly used consistent sets of units and constant values are given after the symbol definitions. These are the SI units and the U.S. customary units. A single set of equations covers both sets of units by including all constants required for the U.S. customary units and defining as unity those not required for the SI units.

ARTHUR J. GLASSMAN



## CONTENTS

CHAPTER	PAGE
<i>PREFACE</i>	iii
9 <i>SUPersonic TURBINES</i> by Louis J. Goldman	1
METHOD OF CHARACTERISTICS	2
DESIGN OF SUPersonic STATOR BLADES	15
DESIGN OF SUPersonic ROTOR BLADES	18
OPERATING CHARACTERISTICS OF SUPersonic TURBINES	24
REFERENCES	29
SYMBOLS	30
10 <i>RADIAL-INFLOW TURBINES</i> by Harold E. Rohlik	31
OVERALL DESIGN CHARACTERISTICS	36
BLADE DESIGN	47
OFF-DESIGN PERFORMANCE	54
REFERENCES	57
SYMBOLS	58
11 <i>TURBINE COOLING</i> by Raymond S. Colladay	59
GENERAL DESCRIPTION	59
HEAT TRANSFER FROM HOT GAS TO BLADE	66
CONDUCTION WITHIN THE BLADE WALL	80
COOLANT-SIDE CONVECTION	82
FILM AND TRANSPERSION COOLING	84
SIMILARITY	92
REFERENCES	97
SYMBOLS	99
12 <i>EXPERIMENTAL DETERMINATION OF AERODYNAMIC PERFORMANCE</i> by Edward M. Szanca and Harold J. Schum	103
TEST FACILITY AND MEASUREMENTS	104
TURBINE PERFORMANCE	126
REFERENCES	139
SYMBOLS	140

**PRECEDING PAGE BLANK NOT FILMED**



## **CHAPTER 9**

# **Supersonic Turbines**

**By Louis J. Goldman**

A supersonic turbine stage is defined as one that operates with a supersonic relative velocity entering the rotor. Supersonic turbines have potential application in systems where high-energy fluids (those having low molecular weights and, consequently, high expansion velocities) are used and/or where high pressure ratios are available. They have been used by NASA in rocket turbopump systems and have been studied for use in open-cycle auxiliary-power systems for space.

Supersonic turbines have the potential for large specific work outputs because of the high pressure ratio. For a given power level, this type of turbine would require a small amount of driving fluid and a small number of stages. It would, therefore, be light-weight and relatively simple. Because of high jet velocities, however, supersonic turbines generally operate at low blade-jet speed ratios (often less than 0.2). As indicated in chapters 2 and 3 (vol. 1), low blade-jet speed ratios correspond to low static efficiencies, primarily because of high exit-kinetic-energy losses. For systems where the primary design criteria are a minimum number of stages along with minimum fluid consumption, the ideal work available from the high pressure ratio could more than offset the lower turbine efficiency and may result in a supersonic turbine being the optimum design choice.

To keep the efficiency of supersonic turbines at the highest possible level, proper design methods must be used. Both supersonic stators and rotors are designed by the method of characteristics. In this chapter, supersonic turbine design and performance are discussed under the following headings: (1) method of characteristics, (2) design

of supersonic stator blades, (3) design of supersonic rotor blades, and (4) operating characteristics of supersonic turbines.

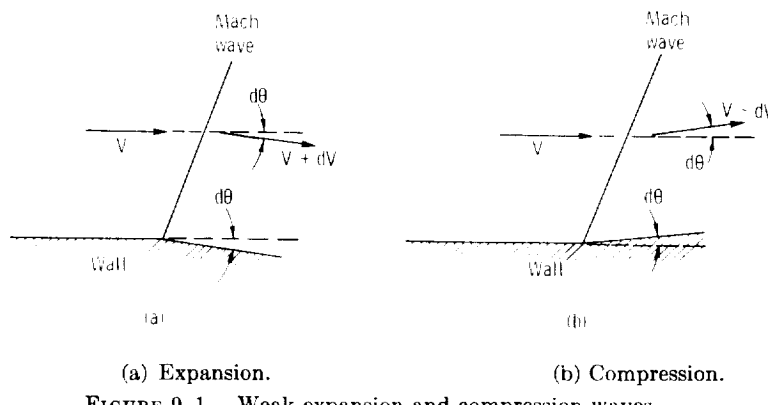
### METHOD OF CHARACTERISTICS

The method of characteristics is a general method for solving a certain type (hyperbolic) of partial differential equation. The equations of motion for the two-dimensional supersonic flow of a perfect gas are of this type. Only this type of flow will be discussed in this chapter. Other types of supersonic flow (i.e., axially symmetric and certain non-steady flows) also can be handled by this method (see ref.1).

The method of characteristics can be developed in two ways: (1) by formal mathematical methods and (2) by simple dynamical considerations. The derivation based on dynamics stresses the physical processes involved. It will be the only one presented here. The mathematical derivation is useful in extending the method to other similar equations. Both developments are given in references 1 and 2.

### Flow Along a Single Wall

The simplest supersonic flow field that satisfies the equations of motion (other than uniform parallel flow) is the flow through a single vanishingly weak standing wave. These waves, called Mach waves, can be considered to be very weak oblique shock waves. The entropy change through the wave is essentially zero. Examples of weak expansion and compression waves are shown in figure 9-1. As will be shown subsequently, an expansion wave is produced when the



(a) Expansion. (b) Compression.

FIGURE 9-1.—Weak expansion and compression waves.

wall bends away from the flow, and a compression wave is produced when the wall bends toward the flow.

The bend (of angular magnitude  $d\theta$ ) in the wall can be considered as a disturbance which produces the wave, which is required if the flow is to follow the wall. The bend in the wall may also be considered as a boundary condition to which one solution is a standing Mach wave with uniform flow fields on both sides of it. The importance of this solution can be appreciated when it is realized that any curved surface may be considered to be made up of a finite number of straight sections. The flow along a curved surface can, therefore, be approximated as the flow through a series of Mach waves. The dynamics of the flow through a weak expansion wave will now be discussed.

Consider the standing Mach wave included at an angle  $\beta$  to the direction of initial velocity  $V$  as shown in figure 9-2. The conservation of mass requires that

$$\frac{w}{A} = \rho V_n = (\rho + d\rho)(V_n + dV_n) = \text{constant} \quad (9-1)$$

where

$w$  mass flow rate, kg/sec; lb/sec

$A$  flow area along Mach wave, m<sup>2</sup>; ft<sup>2</sup>

$\rho$  density, kg/m<sup>3</sup>; lb/ft<sup>3</sup>

$V_n$  velocity component normal to Mach wave, m/sec; ft/sec

Neglecting second-order terms (i.e.,  $d\rho$   $dV_n$ ) gives

$$\rho dV_n + V_n d\rho = 0 \quad (9-2)$$

Conservation of momentum in the tangential direction gives

$$\rho V_n V_t = (\rho + d\rho)(V_n + dV_n)(V_t + dV_t) \quad (9-3)$$

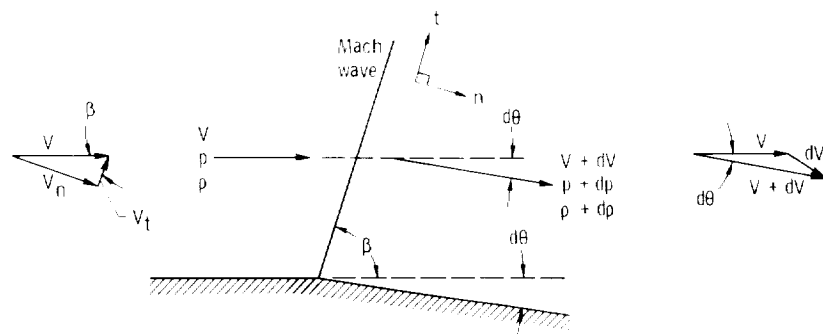


FIGURE 9-2.—Flow through a weak expansion wave, and associated nomenclature.

where  $V_t$  is the velocity component tangent to the Mach wave, in m/sec or ft/sec. Substituting equation (9-1) into equation (9-3) gives

$$\rho V_n V_t = \rho V_n (V_t + dV_t) \quad (9-4)$$

or

$$dV_t = 0 \quad (9-5)$$

This means that the tangential component of velocity remains constant as the flow crosses the wave. Consequently, the velocity change  $dV$  is equal to  $dV_n$  and is directed normal to the Mach wave.

Conservation of momentum in the normal direction gives

$$gp + \rho V_n^2 = g(p + dp) + (\rho + d\rho)(V_n + dV_n)^2 \quad (9-6)$$

where

$g$  conversion constant, 1; 32.17 (lbm)(ft)/(lbf)(sec<sup>2</sup>)

$p$  absolute pressure, N/m<sup>2</sup>; lb/ft<sup>2</sup>

Substituting equation (9-1) into equation (9-6) and expanding yields

$$0 = g dp + \rho V_n dV_n \quad (9-7)$$

Eliminating  $dV_n$  by using equation (9-2) results in

$$V_n^2 = g \left( \frac{dp}{d\rho} \right) \quad (9-8)$$

Equation (1-57) of chapter 1 (vol. 1) states

$$a = \sqrt{g \left( \frac{dp}{d\rho} \right)_s} \quad (9-9)$$

where  $a$  is speed of sound, in m/sec or ft/sec. Since the differential process being considered here is isentropic, substitution of equation (9-8) into equation (9-9) shows that

$$V_n = a \quad (9-10)$$

Therefore, the component of velocity normal to the Mach wave must be equal to the speed of sound. Noting from figure 9-2 that

$$V_n = V \sin \beta \quad (9-11)$$

gives

$$\sin \beta = \frac{V_n}{V} = \frac{a}{V} = \frac{1}{M} \quad (9-12)$$

where  $M$  is the Mach number. The angle  $\beta$  is called the Mach angle and has meaning only for  $M \geq 1$ .

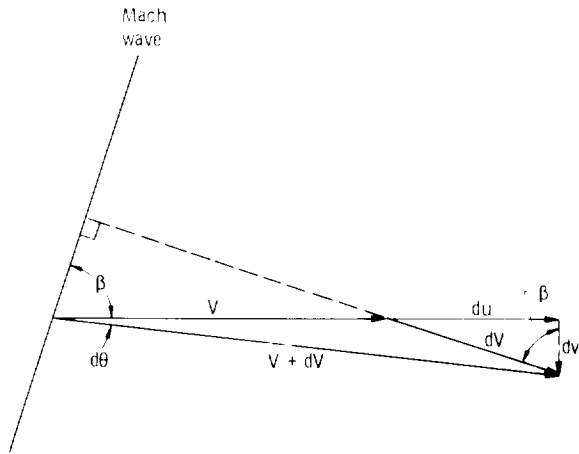


FIGURE 9-3.—Velocity diagram for flow through a weak expansion wave.

The relation between change in flow angle  $d\theta$  and velocity change  $dV$  can be found from the velocity relations shown geometrically in figure 9-3. In the limit ( $d\theta \rightarrow 0$ ),

$$du = dV \quad (9-13)$$

$$dv = V d\theta \quad (9-14)$$

and

$$\tan \beta = \frac{du}{dv} = \frac{dV}{V d\theta} \quad (9-15)$$

where

- |      |  |
|------|--|
| $du$ | component of $dV$ parallel to initial velocity $V$ , m/sec; ft/sec |
| $dv$ | component of $dV$ normal to initial velocity $V$ , m/sec; ft/sec   |

Since, as can be determined from equation (9-12),

$$\tan \beta = \frac{1}{\sqrt{M^2 - 1}} \quad (9-16)$$

equation (9-15) becomes

$$\frac{dV}{V} = \frac{d\theta}{\sqrt{M^2 - 1}} \quad (9-17)$$

It is more convenient if  $dV/V$  is expressed in terms of the critical velocity ratio  $M^* = V/V_{cr}$  rather than Mach number  $M$ . The critical velocity  $V_{cr}$  is equal to the speed of sound at the critical condition ( $M=1$ ) and can be evaluated from equation (1-63) of chapter 1 (vol. 1). The relation between  $M^*$  and  $M$  is given by the equation

$$M = \sqrt{\frac{\frac{2}{\gamma+1} M^{*2}}{1 - \frac{\gamma-1}{\gamma+1} M^{*2}}} \quad (9-18)$$

where  $\gamma$  is the ratio of specific heat at constant pressure to specific heat at constant volume. Since  $V_c$  is constant (because the total temperature is constant),

$$\frac{dV}{V} = \frac{dM^*}{M^*} \quad (9-19)$$

Substituting equations (9-18) and (9-19) into equation (9-17) gives, finally,

$$d\theta = \sqrt{\frac{M^{*2}-1}{1-\frac{\gamma-1}{\gamma+1} M^{*2}}} \frac{dM^*}{M^*} \quad (9-20)$$

This is the differential relation between a change in flow angle and a velocity change through a single weak expansion wave. A similar relation could have been obtained for a single weak compression wave, except that equation (9-20) would have a minus sign.

Let us now consider the flow along a curved (convex) surface, as shown in figure 9-4. Assume that the surface is composed of a number of small bends, each producing a Mach wave. The relation indicated by equation (9-20) will be satisfied through each Mach wave provided the changes in  $\theta$  are small. The combined flow field will, therefore, be a solution to the equations of motion for infinitesimal values of  $d\theta$ . This type of flow is called Prandtl-Meyer flow, or simple wave flow.

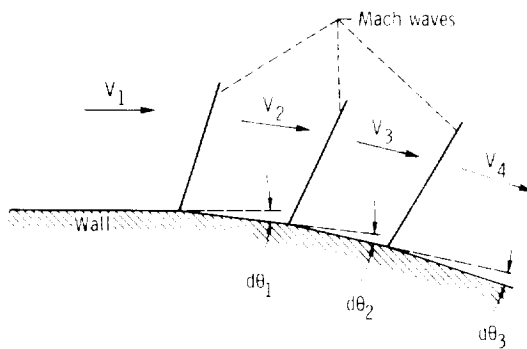


FIGURE 9-4.—Representation of flow along a convex wall.

If the number of segments approaches infinity, the flow field becomes continuous. Integration of equation (9-20) gives

$$\theta = \frac{1}{2} \sqrt{\frac{\gamma+1}{\gamma-1}} \arcsin [(\gamma-1)M^{*2} - \gamma] + \frac{1}{2} \arcsin \left( \frac{\gamma+1}{M^{*2}} - \gamma \right) + \text{constant} \quad (9-21)$$

If the constant is chosen such that  $\theta=0$  when  $M^*=1$  ( $M=1$ ), the angle given by equation (9-21) is called the Prandtl-Meyer angle, and it is tabulated in many references (e.g., ref. 1). The Prandtl-Meyer angle is the angle through which the flow must turn in going from Mach 1 to the required Mach number and is often given the symbol  $\omega$  (or  $\nu$ ). Therefore,

$$\omega = \frac{1}{2} \sqrt{\frac{\gamma+1}{\gamma-1}} \left\{ \frac{\pi}{2} + \arcsin [(\gamma-1)M^{*2} - \gamma] \right\} - \frac{1}{2} \left[ \frac{\pi}{2} - \arcsin \left( \frac{\gamma+1}{M^{*2}} - \gamma \right) \right] \quad (9-22)$$

Note that the change in flow direction ( $\Delta\theta$ ) in going from  $V_1$  to  $V_2$  is given by the change in the respective Prandtl-Meyer angles. That is,

$$\theta_2 - \theta_1 = \Delta\theta = \omega_2 - \omega_1 \quad (9-23)$$

The derivation has been for expansion waves. For compression waves, there would be a minus sign in equation (9-17). Therefore, the velocity decreases ( $M$  decreases) for flow through a compression wave. This means that the Mach angle  $\beta$  increases for flow along a concave wall, shown in figure 9-5. The Mach lines, there-

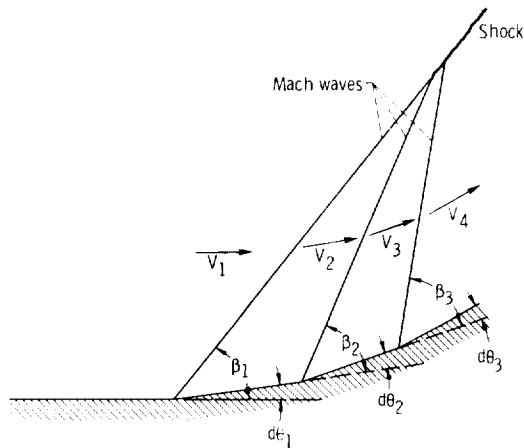


FIGURE 9-5.—Representation of flow along a concave wall.

fore, converge and form a shock as shown in the figure. The derived relations, of course, would be invalid in the shock region because of the entropy increase.

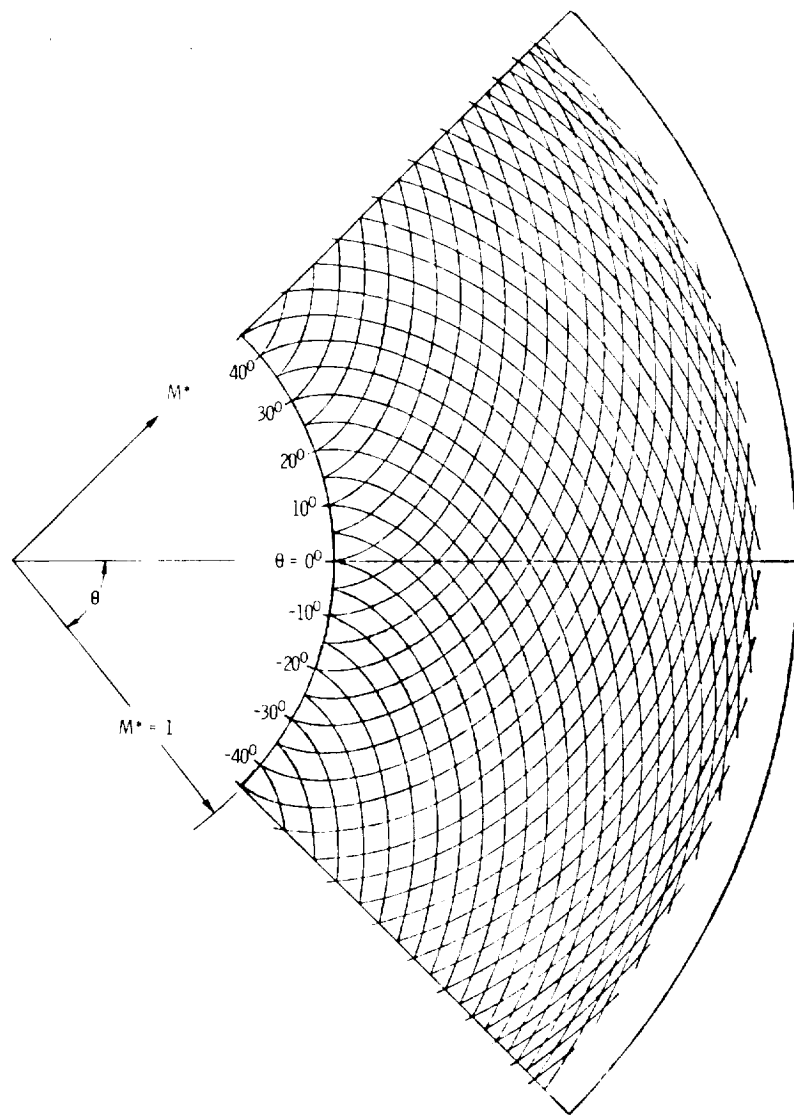


FIGURE 9-6.—Hodograph characteristic curves.

The relation between the flow angle  $\theta$  and the critical velocity ratio  $M^*$  (eq. (9-21)) can be plotted on a polar diagram, as shown in figure 9-6. This type of diagram is called a hodograph plot. The curves of this plot are characteristic of the flow around any two-dimensional convex surface and are called hodograph characteristics. The value of the constant of equation (9-21) has been varied to generate these curves. The curves passing through  $M^*=1$  at  $\theta=0$  represent the variation of Prandtl-Meyer angle with critical velocity ratio as expressed by equation (9-22).

An important property of the hodograph characteristics is that the normals to the characteristics are parallel to the corresponding Mach wave in the physical plane. This allows the flow field to be constructed graphically and is best explained by a simple example. Consider the flow along a curved wall. After the wall is divided into a finite number of segments (fig. 9-7(a)), the initial point  $P_1$  is located on the characteristic curve (fig. 9-7(b)) corresponding to  $V_1$  (line  $OP_1$  parallel to  $\vec{V}_1$ ). Point  $P_2$  is located in the hodograph diagram by drawing the line  $OP_2$  parallel to  $\vec{V}_2$  (or wall segment  $S_2$ ). Note that  $P_2$  must lie on the expansion characteristic curve through  $P_1$ . The Mach wave separating  $V_1$  and  $V_2$  is found by drawing the normal (shown as  $N_1$  in the figure) to the characteristic segment  $P_1P_2$ . This direction is parallel to the Mach wave direction in the physical plane. The preceding process is continued through the additional segments.

The graphical procedure is, at best, cumbersome to use. The procedure may be made entirely numerical if it is recalled that the direc-

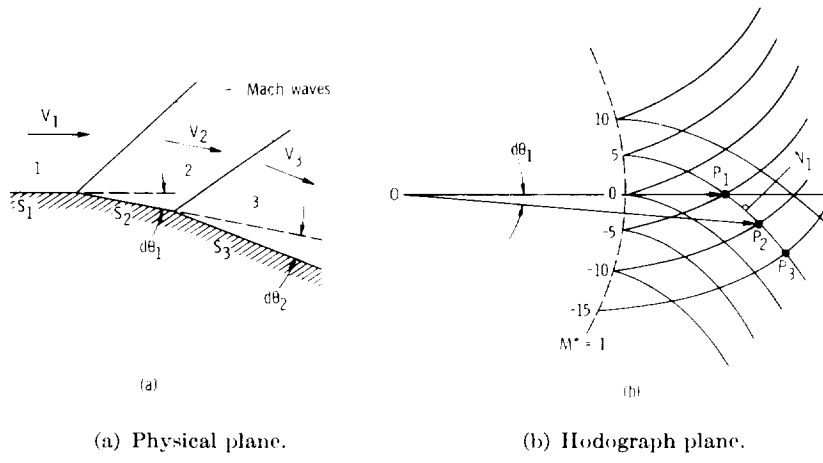


FIGURE 9-7.—Flow along convex wall.

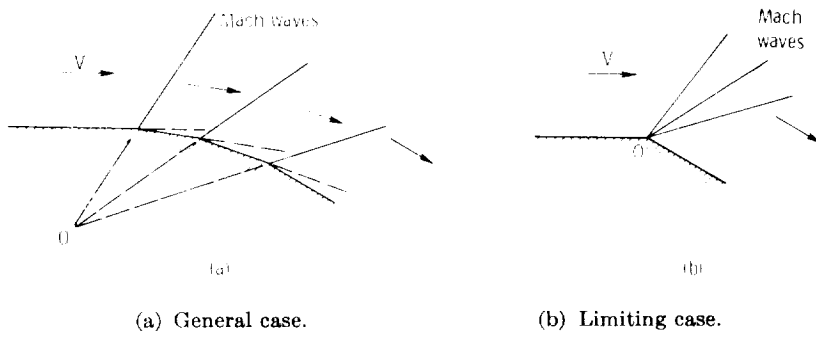


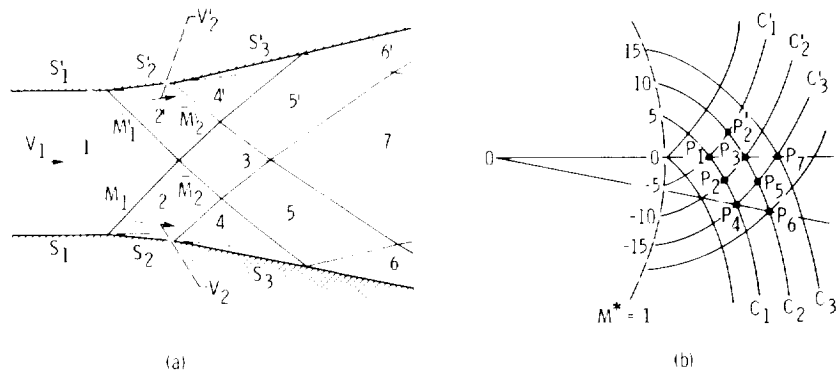
FIGURE 9-8.—Flow along convex wall with Mach waves intersecting at one point.

tion of the Mach wave is given by the Mach angle  $\beta$ . Since finite changes occur in the solution of practical problems, it is usually assumed that the waves lie at the Mach angle corresponding to the average speed between the two points, measured relative to the average direction of the flow between the two points. The flow past a wall may now be constructed completely numerically. The hodograph diagram, though, is still useful for visualization.

A special case of flow along a single wall occurs if the wall is so shaped that the Mach lines pass through a common point, as shown in figure 9-8(a). Now imagine that the wall approaches the common point  $O$ . The limiting case is represented by figure 9-8(b), where it is seen that a single large bend has replaced a number of small bends. This type of flow is often called corner-type flow, or flow around a corner, and as will be seen later, is important to the design of supersonic nozzles with sharp-edged throats. Equation (9-21) is still valid for this case.

### Flow Between Two Walls

The method of solution used for the flow along a single wall can be generalized to handle the flow between two walls. Consider the initially uniform parallel supersonic flow bounded by two walls as shown in figure 9-9. Suppose that both walls are deflected outward the same amount. The flow is symmetric about the centerline of the channel. As before, the flow will be constructed by dividing the walls into a finite number of straight line segments, denoted here by  $S_1$  and  $S'_1$ ,  $S_2$  and  $S'_2$ , and  $S_3$  and  $S'_3$ . The initial parallel flow field in region 1 is represented by the point  $P_1$  in the hodograph diagram. The line  $OP_1$  represents the direction and magnitude of the velocity  $\vec{V}_1$ . The flow



(a) Physical plane.

(b) Hodograph plane.

FIGURE 9-9.—Flow between two walls.

in regions 2 and 2' (points  $P_2$  and  $P'_2$  in the hodograph diagram) can be determined, as before, for the flow through a weak expansion wave. The lines  $OP_2$  and  $OP'_2$  are parallel to  $\vec{V}_2$  and  $\vec{V}'_2$ , respectively.

The problem now is to determine what happens to the flow after the two initial Mach waves intersect. Flow fields 2 and 2' must be separated by another flow field, since  $\vec{V}_2$  and  $\vec{V}'_2$  are not in the same direction. Consider that the flow field 3 is separated from 2 and 2' by a continuation, in modified form, of the initial Mach waves  $\overline{M}_1$  and  $\overline{M}'_1$ . A jump from region 2 through any wave can satisfy the equations of motion only if the end point lies on a characteristic through  $P_2$ ; that is,  $C_1$  or  $C'_2$  (since these curves represent eq. (9-21) graphically). Similarly, a jump from region 2' must lie on characteristic  $C'_1$  or  $C_2$ . To satisfy both sets of conditions, the end point of the jump representing the flow field 3 must be either point  $P_3$  or  $P_1$  in the hodograph plane. The end point being  $P_1$  can be ruled out because this would mean that the extensions of the expansion waves are compression waves, which makes little physical sense. The end point being  $P_3$  in the hodograph plane makes sense because it represents further flow expansion. The direction of the extensions  $\overline{M}_2$  and  $\overline{M}'_2$  of the initial Mach waves are given by the normals to the segments  $P'_2P_3$  and  $P_2P_3$ , respectively, in the hodograph plane. Because of the assumed symmetry of the flow, the velocity  $\vec{V}_3$  is parallel to  $\vec{V}_1$ . These procedures can be used to construct the flow field piecemeal until one of the waves advancing across the channel strikes the wall. A new type of solution is now required.

Consider the flow in field 4, which is parallel to the wall segment  $S_3$ . The flow in field 5 is not parallel to the wall. Therefore, field 5 cannot extend the wall, and a new field 6 must separate it from the wall. The flow in field 6 is parallel to the wall and, therefore, point  $P_6$  in the hodograph plane must lie on the extension of line  $OP_4$ , because the flows in fields 4 and 6 are in the same direction. Also,  $P_6$  must lie on one of the characteristics through  $P_5$ , that is,  $C_2$  or  $C'_3$ . According to arguments similar to those used before, these conditions require that  $P_6$  be located as shown in the hodograph diagram, where the wave between  $P_5$  and  $P_6$  is an expansion wave. In general, an expansion wave striking a solid boundary reflects as an expansion wave. The construction of the flow in the interior of the channel proceeds as before.

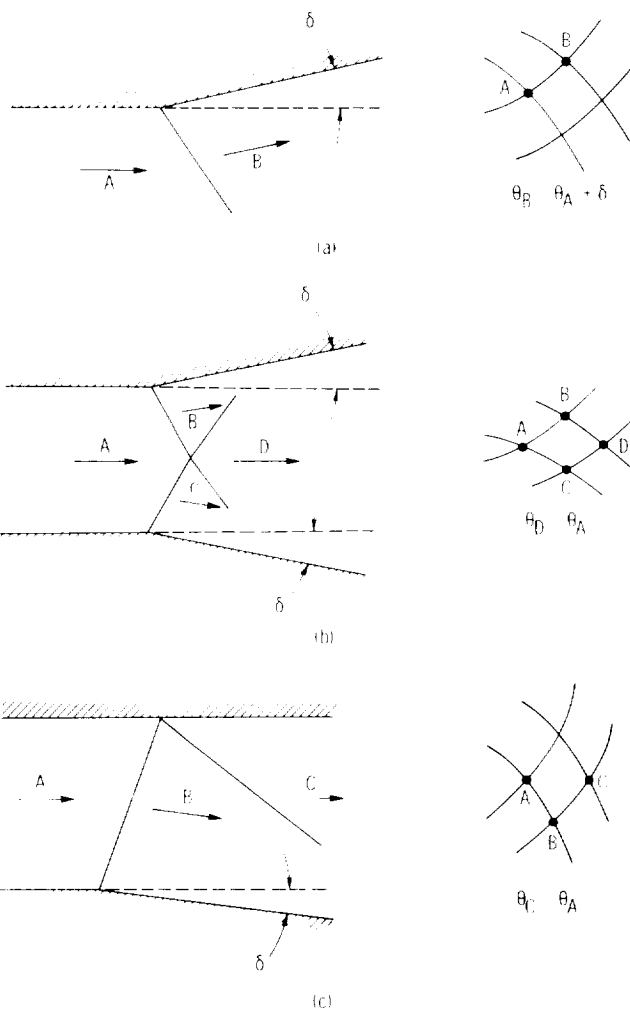
As seen from the foregoing discussion, the flow in the channel may be approximated by a number of small quadrilateral regions in each of which the velocity is constant. The sides of the quadrilaterals are the Mach waves. The equations of motion are satisfied in finite form across each wave and, therefore, are approximately satisfied throughout the entire flow field. This type of procedure is called the "field method," since the stream properties are found in small regions, or fields. Another calculation procedure, known as the "lattice-point method," is often used in supersonic flow problems. In this procedure, the stream properties are found at the intersections, or lattice points, of the Mach net. Both methods are, for most practical situations, identical. The "lattice-point method" will not be discussed further. Both methods are described in reference 1.

### Summary of Elementary Flow Solutions

The flow solutions previously discussed, as well as others that are used for the design of supersonic stator and rotor blade sections, are summarized in figure 9-10. For each case, the physical situation is shown along with the hodograph solution. Figures 9-10(a), (b), and (c) show the previously discussed cases of a weak expansion wave, the intersection of expansion waves, and the reflection of an expansion wave from a solid boundary, respectively. In figure 9-10(c), the reflected wave is at a slightly smaller Mach angle than is the incident wave because of the higher Mach number associated with the flow across the reflected wave.

Figure 9-10(d) shows the cancellation of an expansion wave at a solid boundary. A bend at the proper location in the top wall is made in the same direction and of the same magnitude as the flow deflection produced by the wave. The boundary conditions are, therefore, satisfied without any additional (reflected) waves.

Figure 9-10(e) shows the solution for the flow field beyond the intersection of an expansion wave and a compression wave. The hodograph point representing region *D* must lie on the intersection of characteristic curves passing through *B* and *C*, as shown. Therefore, each wave continues unchanged in type beyond the intersection.

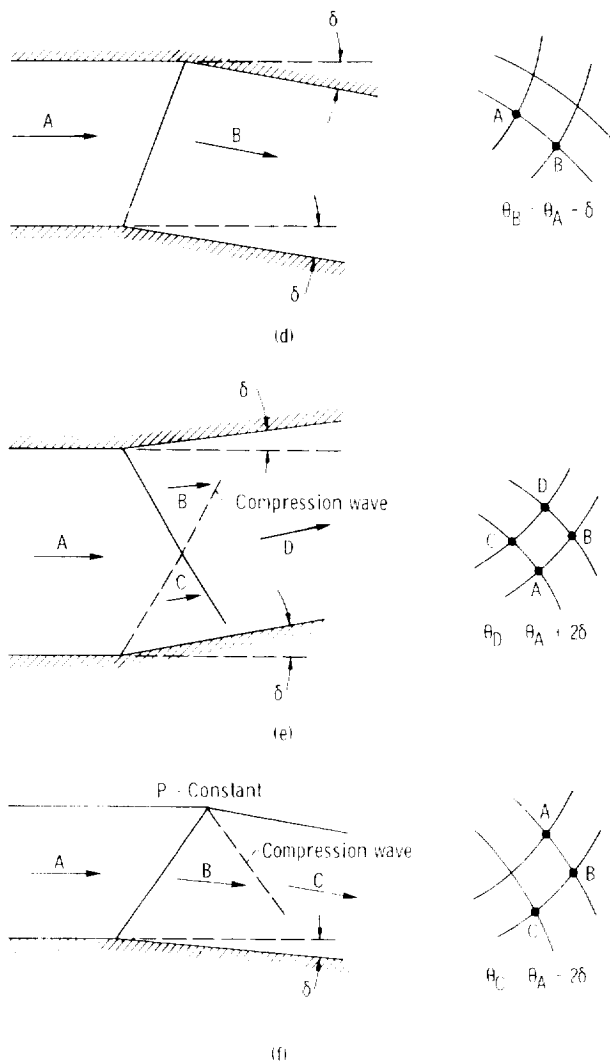


(a) Weak expansion wave.

(b) Intersection of expansion waves.

(c) Reflection of an expansion wave from a solid boundary.

**FIGURE 9-10.**—Elementary flow solutions.



(d) Cancellation of expansion wave at solid boundary.

(e) Intersection of expansion and compression waves.

(f) Reflection of expansion wave from a free boundary (constant pressure).

FIGURE 9-10.—Concluded.

A case that is not encountered in the design of supersonic blade sections, but may be of general interest, is shown in figure 9-10(f). This is the reflection of an expansion wave from a constant-pressure free boundary. The boundary condition requires that the pressure be

constant along the outside streamline. Since the flow is isentropic, the velocity magnitude of all the flow fields lying along the boundary must be equal. Therefore, field *C* must be as shown in the hodograph plane. In general, an expansion wave reflects from a free boundary (constant pressure) as a compression wave.

### DESIGN OF SUPersonic STATOR BLADES

One of the most important uses of the method of characteristics is its application to the design of a channel to produce uniform, parallel flow at supersonic speeds. This is the basis of the design of two-dimensional nozzles for supersonic wind tunnels. This type of nozzle also has application to supersonic-turbine stator blades, since it is desired to have uniform parallel flow entering the rotor. Only the design of a stator based on this type of nozzle will be discussed here.

#### Nozzles Producing Uniform Parallel Flow

A supersonic nozzle that produces uniform, parallel flow is shown in figure 9-11. Since it is required that the flow be parallel and supersonic, the wall must first curve outward (*AD*) and then curve in again (*DE*), so that at the exit, the wall is again parallel to the initial flow. Point *D* is the point where the wall has its maximum slope. It is usually assumed that the flow at the throat is uniform, parallel, and sonic ( $M=1$ ). Because of the nozzle symmetry, the nozzle axis is a streamline and may, for design purposes, be replaced by a solid boundary. Therefore, only one half of the nozzle need be designed.

The flow region *ABCDA* is called the expansion zone. The curved wall *AD* generates expansion waves which reflect off the centerline. The calculation procedure is the same as was discussed in the section

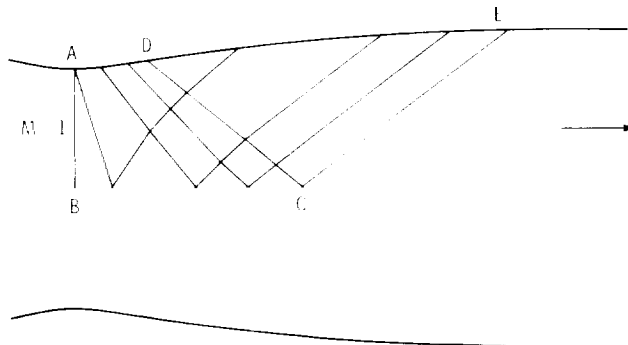
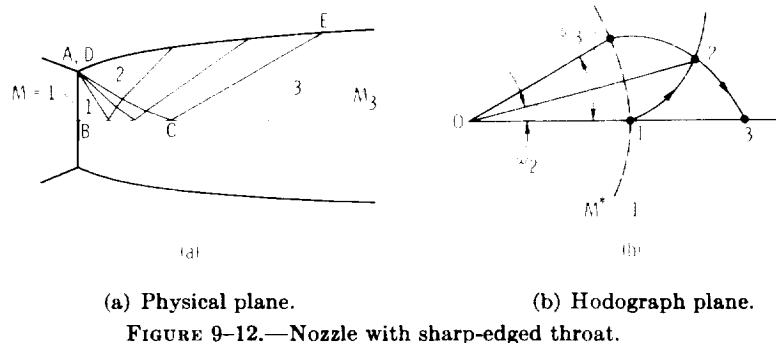


FIGURE 9-11.—Supersonic nozzle producing uniform, parallel flow.

**"Flow Between Two Walls."** The region  $DCED$  is called the straightening section, and the wall in this section is curved so that the incoming expansion waves are cancelled. The method of cancelling waves was seen in the section "Summary of Elementary Flow Solutions." The flow past  $CE$  is uniform, parallel, and supersonic. The final Mach number depends on how much expansion occurs between  $A$  and  $D$ . For large exit Mach numbers, a nozzle of this type may be too long for supersonic turbine applications. In these cases, a limiting form of this type of nozzle is used.

A nozzle with a sharp-edged throat, shown in figure 9-12(a), produces uniform, parallel flow in the shortest possible length. It is a limiting form of the nozzle described previously (fig. 9-11), where points  $A$  and  $D$  coincide. The flow expands around the sharp edge (corner flow), producing waves that are reflected by the centerline. Cancellation of the reflected waves is again used to obtain uniform parallel flow at the exit. The hodograph diagram (fig. 9-12(b)) shows that one half of the expansion occurs as a result of the corner flow, and the other half as a result of the reflected waves. Therefore, the wall bounding region 2 is set at an angle equal to the Prandtl-Meyer angle  $\omega_2$ , which is half of the design exit Prandtl-Meyer angle  $\omega_3$ .

A computer program has been written (ref. 3) to design supersonic nozzles with sharp-edged throats by the method of characteristics. Only the supersonic portion of the nozzle is designed by the program. The input to the computer program includes the desired exit Mach number and the specific-heat ratio  $\gamma$  of the working fluid. The program output gives the coordinates of the nozzle. The program of reference 3 does not account for any flow losses.



(a) Physical plane.

(b) Hodograph plane.

FIGURE 9-12.—Nozzle with sharp-edged throat.

### Stator Nozzles

The sharp-edged-throat nozzle just discussed serves as the basis for the design of minimum-length (chord) supersonic stators. Additional considerations for a stator as compared to the nozzle previously

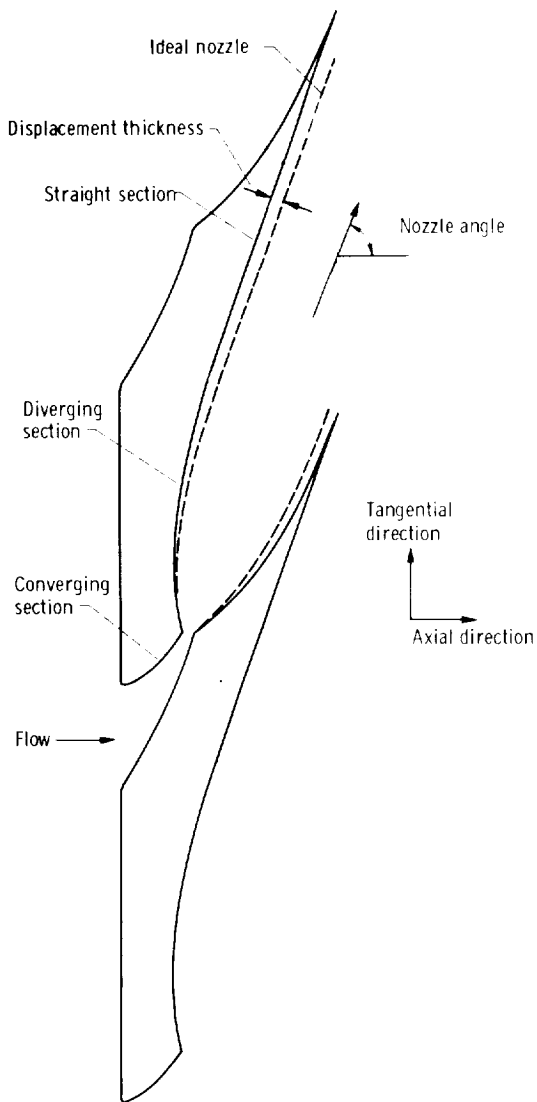


FIGURE 9-13.—Design of supersonic stator nozzle with sharp-edged throat.

discussed are the flow turning and the desire to include flow and energy losses.

A supersonic-turbine stator blade and channel section of the type being discussed herein is shown in figure 9-13 and will be referred to as a stator nozzle. The stator nozzle consists of three sections: (1) a converging (subsonic) section, (2) a diverging (supersonic) section, and (3) a straight section on the suction surface. The converging section accelerates the flow to sonic speed and can be designed by the methods of chapter 5 (vol. 2). In order to minimize losses, the converging section is designed to produce all of the turning of the flow. The diverging section accelerates the flow to the desired free-stream Mach number at the exit. This section is designed by the method of characteristics as previously discussed. The straight section on the suction surface completes the nozzle profile, and its length is determined by the required nozzle angle.

A computer program for the design of sharp-edged-throat supersonic stator nozzles, including a correction for losses, is presented in reference 4. An ideal (no loss) nozzle profile, indicated by the dashed lines in figure 9-13, is first designed by the method of characteristics. Boundary-layer parameters (displacement thickness, momentum thickness, etc.) are then computed for the ideal profile by methods discussed in chapter 6 (vol. 2). The final profile is then obtained by adding the local displacement thicknesses to the ideal nozzle coordinates as indicated in figure 9-13. The nozzle efficiency is obtained from the boundary-layer parameters as described in chapter 7 (vol. 2).

## DESIGN OF SUPERSONIC ROTOR BLADES

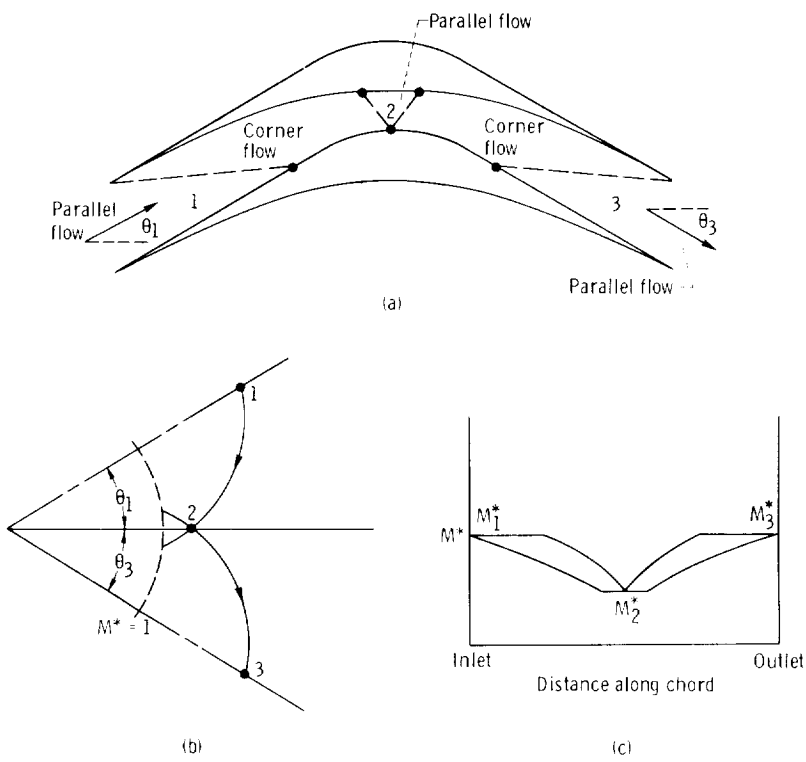
Two methods that have been proposed for the design of supersonic rotors are discussed herein. Both design methods use the method of characteristics. The channel is designed to prevent any shock formation caused by the convergence of compression waves. The flow entering the rotor passage is assumed to be uniform and parallel.

### Corner-Flow Method

One method of designing supersonic rotor blades is given by Shapiro (ref. 1). A typical blade of this type is shown in figure 9-14(a). The entering uniform, parallel flow (region 1) undergoes a corner-type compression, resulting from flow along the concave lower (pressure) surface of the blade. The upper (suction) surface is curved so as to cancel the incoming compression waves. In region 2, parallel horizontal flow ( $\theta=0$ ) is obtained. This parallel flow then undergoes a corner-type expansion, with waves being cancelled by the concave

surface, until uniform parallel flow of the desired Mach number occurs at the blade exit. Straight-line segments on the upper surface, parallel to the inlet and outlet flow directions, complete the blade profile.

For an impulse blade (as shown in fig. 9-14(a)), only one half of the blade needs to be designed, since it is symmetrical. The specification of corner flow makes this type of blade particularly easy to design, since only waves of one kind are present in any region. The hodograph diagram for this blade is shown in figure 9-14(b). Shown in figure 9-14(c) is the theoretical blade-surface velocity distribution, which is quite unusual. This type of velocity distribution is not very desirable, because the loading becomes zero in the middle of the blade. Another drawback of this design method is that for a given inlet Mach number,



(a) Blade and passage.  
 (b) Hodograph diagram.      (c) Blade loading diagram  
**FIGURE 9-14.—Supersonic rotor design by the corner-flow method.**

the amount of flow turning is limited. The velocity in region 2 must be sonic (Mach 1) or higher. The maximum amount of flow turning is, therefore, equal to the sum of the inlet and exit Prandtl-Meyer angles. For reasonable Mach number levels (1.5 to 3.0), large amounts of flow turning ( $120^\circ$  to  $150^\circ$ ) would be impossible.

#### Vortex-Flow Method

Another method of designing supersonic rotor blades is described in reference 5. This method is based on establishing vortex flow within the passage. In a vortex-flow field, the product of velocity (also, therefore, critical velocity ratio  $M^*$ ) and streamline radius is a constant throughout the field. A typical blade and passage designed by this method is shown in figure 9-15(a).

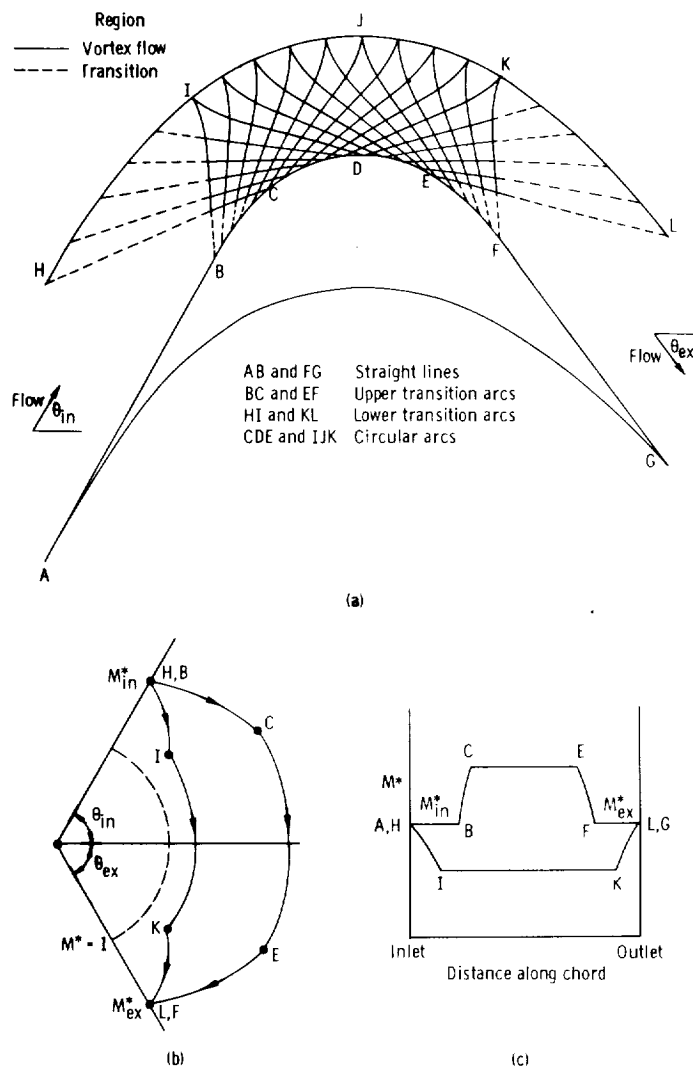
The blades consist essentially of three parts: (1) inlet transition arcs, (2) circular arcs, and (3) outlet transition arcs. The inlet transition arcs (lower and upper) convert the uniform parallel flow at the passage inlet into vortex flow by means of the compression waves generated by the lower transition arc and the expansion waves generated by the upper transition arc (see fig. 9-15(a)). The vortex-flow field begins where the compression and expansion waves first intersect. The concentric circular arcs turn and maintain the vortex flow. The outlet transition arcs reconvert the vortex flow into uniform parallel flow by cancelling the remaining waves generated by the circular arcs. Straight-line segments on the upper surface and parallel to the inlet and outlet flow directions complete the blade profile.

A hodograph diagram for this type of design is shown in figure 9-15(b). The flows along the blade surfaces are shown, with the letters corresponding to the locations indicated in figure 9-15(a). The constant-velocity flows along the circular arcs of the blade surfaces are represented by the circular arcs *IK* and *BF* on the hodograph diagram. In this type of design, there is no limit to the amount of flow turning obtainable in the rotor, because the circular arcs can provide any necessary degree of turning. The surface velocity distribution is shown on the blade-loading diagram, figure 9-15(c). This blade is seen to be quite highly loaded, especially as compared to the corner-flow design shown in figure 9-14.

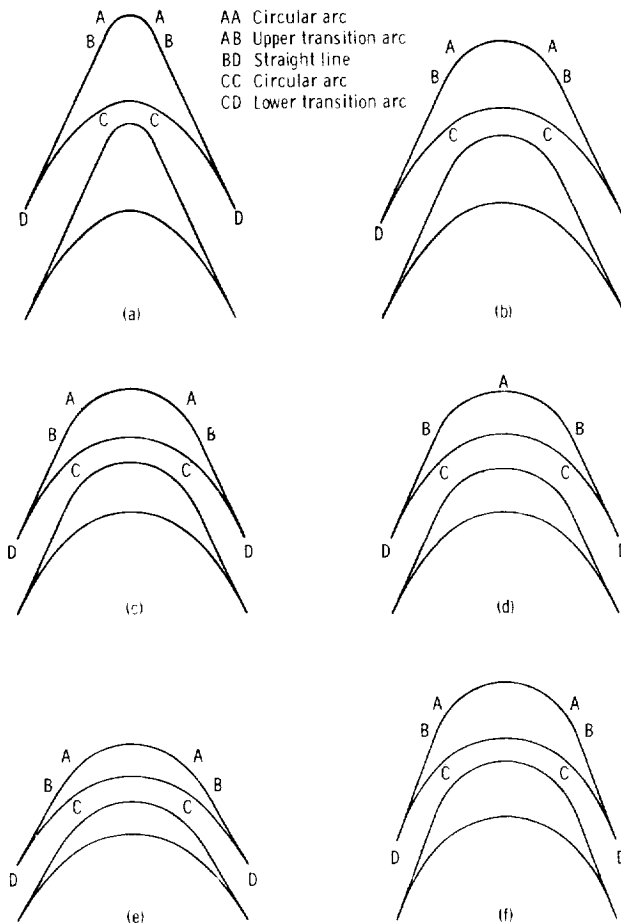
A computer program for designing rotor blades of this type by the method of characteristics is presented in reference 6. The computer program input includes the inlet and outlet flow angles, the inlet, outlet, and surface Mach numbers, and the specific-heat ratio of the gas. The output includes the rotor blade coordinates and a plot of the blade shape. An approximate method for obtaining the transition arcs without using the method of characteristics is described in

references 7 and 8. In this procedure, the vortex flow is established by making the curvature of the transition arcs one-half the curvature of the circular arcs. For very small curvatures, this method is correct.

In this blade design, the lower- and upper-surface Mach numbers are specified. This permits blades of various shapes to be designed for



(a) Blade and passage.  
 (b) Hodograph diagram. (c) Blade loading diagram.  
 FIGURE 9-15.—Supersonic rotor design by the vortex-flow method.



- (a) Lower-surface Prandtl-Meyer angle,  $0^\circ$  ( $M=1$ ); upper-surface Prandtl-Meyer angle,  $59^\circ$  ( $M=3.5$ ); total flow turning angle,  $130^\circ$ .
- (b) Lower-surface Prandtl-Meyer angle,  $12^\circ$  ( $M=1.5$ ); upper-surface Prandtl-Meyer angle,  $59^\circ$  ( $M=3.5$ ); total flow turning angle,  $130^\circ$ .
- (c) Lower-surface Prandtl-Meyer angle,  $18^\circ$  ( $M=1.7$ ); upper-surface Prandtl-Meyer angle,  $59^\circ$  ( $M=3.5$ ); total flow turning angle,  $130^\circ$ .
- (d) Lower-surface Prandtl-Meyer angle,  $18^\circ$  ( $M=1.7$ ); upper-surface Prandtl-Meyer angle,  $104^\circ$  ( $M=10.7$ ); total flow turning angle,  $130^\circ$ .
- (e) Lower-surface Prandtl-Meyer angle,  $21^\circ$  ( $M=1.8$ ); upper-surface Prandtl-Meyer angle,  $59^\circ$  ( $M=3.5$ ); total flow turning angle,  $120^\circ$ .
- (f) Lower-surface Prandtl-Meyer angle,  $21^\circ$  ( $M=1.8$ ); upper-surface Prandtl-Meyer angle,  $59^\circ$  ( $M=3.5$ ); total flow turning angle,  $140^\circ$ .

FIGURE 9-16.—Turbine blade shapes at inlet Mach number of 2.5 (inlet Prandtl-Meyer angle of  $39^\circ$ ) and specific-heat ratio of 1.4.

a given inlet Mach number. A number of blades designed by the program of reference 6 for an inlet Mach number of 2.5 are shown in figure 9-16. From the figure, it is seen that the upper-surface Mach number (cf. figs. 9-16(c) and (d)) has little effect on the blade shape, whereas the lower-surface Mach number (cf. figs. 9-16(a), (b), and (c)) and the flow turning (cf. figs. 9-16(e) and (f)) have significant effects. Guidance in the selection of a blade design is obtained by consideration of flow separation and supersonic starting problems, both of which will be discussed later in this chapter.

The previously discussed "method of characteristics" design procedure is only for the case of ideal (isentropic) flow. A computer program for the design of supersonic-turbine vortex-flow rotor sections, including a correction for losses, is presented in reference 9. The ideal (no loss) passage profile, indicated by the dashed lines in figure 9-17, is first designed by the method of characteristics. Boundary-layer parameters are then computed, and the final profile is then obtained by adding the local displacement thicknesses to the ideal profile as indicated in figure 9-17. Rotor profile loss coefficients are determined from the boundary-layer parameters as described in chapter 7 (vol. 2).

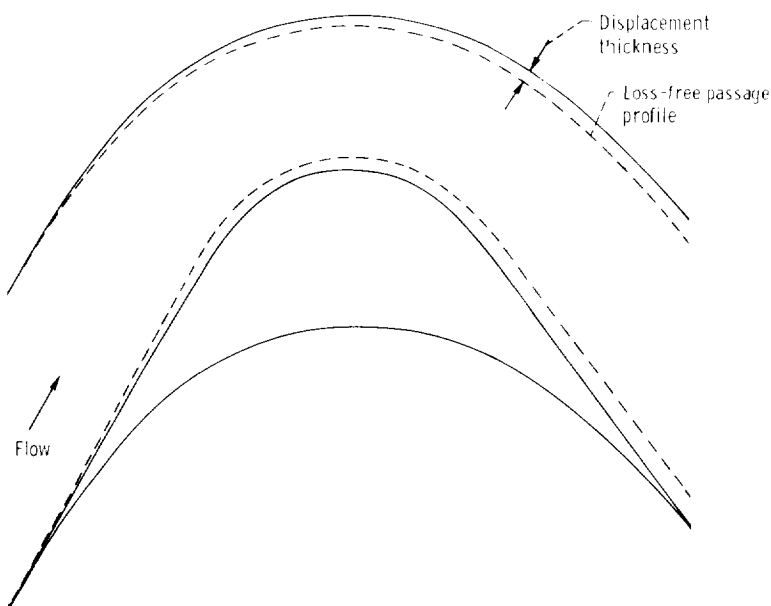


FIGURE 9-17.—Design of supersonic rotor blade section.

As seen from figure 9-15, adverse pressure gradients exist along transition arcs *HI* and *EF* within the rotor blade passages. The boundary-layer calculations give an indication of whether the pressure gradients are severe enough to cause flow separation. Flow separation results in large losses. If it is possible, it would be desirable to prevent separation. The separation criterion places limitations on the choice of the upper- and lower-surface Mach numbers.

## OPERATING CHARACTERISTICS OF SUPERSONIC TURBINES

### Supersonic Starting

Problems occur in the starting of supersonic diffusers because the diffuser must be able to swallow the shock that forms at the inlet

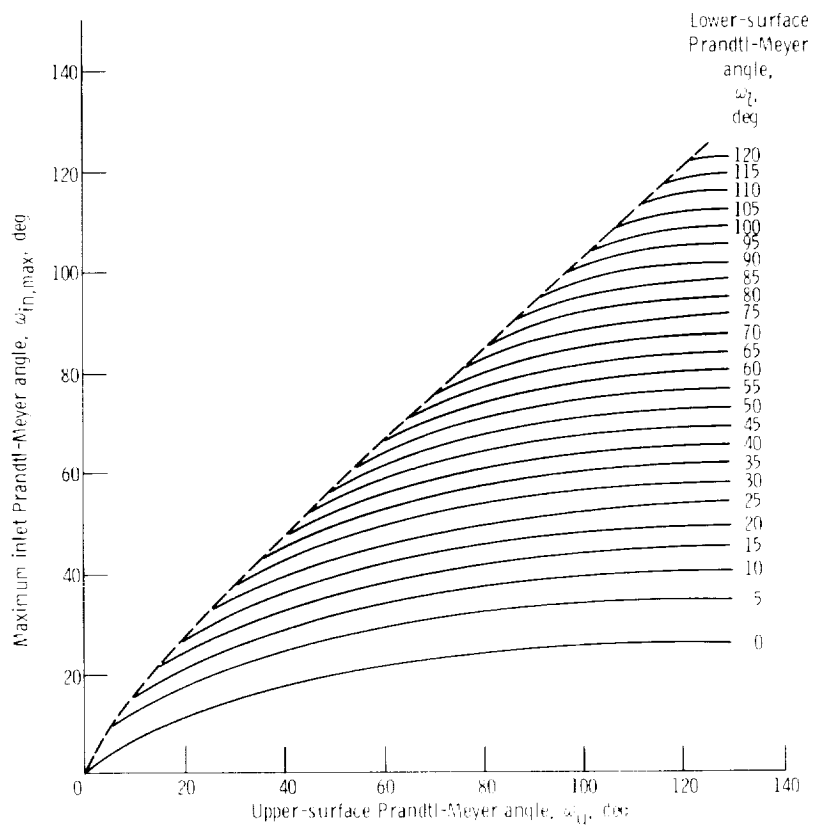


FIGURE 9-18.—Maximum Prandtl-Meyer angle for supersonic starting. Specific-heat ratio, 1.4.

during startup. Since the rotor blade passage is convergent-divergent in shape, similar problems would be expected to occur in the starting of supersonic turbines. As a first approximation, it is assumed that a normal shock spans the rotor blade passage at the instant of starting. The permissible contraction of the blade passage is set by this condition, since the passage must be large enough to permit the shock wave to pass through.

For specified flow Mach numbers along the circular-arc segments of the blade surfaces (often expressed in terms of the corresponding Prandtl-Meyer angles  $\omega_u$  and  $\omega_l$ ), there exists a maximum value of the inlet Mach number (or inlet Prandtl-Meyer angle) for which supersonic flow can be established. The calculation procedure for determining this maximum value is given in reference 6. In figure 9-18, the maximum inlet Prandtl-Meyer angle for supersonic starting of vortex-flow rotor blades is plotted as a function of the blade-surface Prandtl-Meyer angles. In the usual design problem, the inlet Prandtl-Meyer angle is known from the velocity diagram, and the surface Prandtl-Meyer angles must then be determined in order to obtain the rotor blade

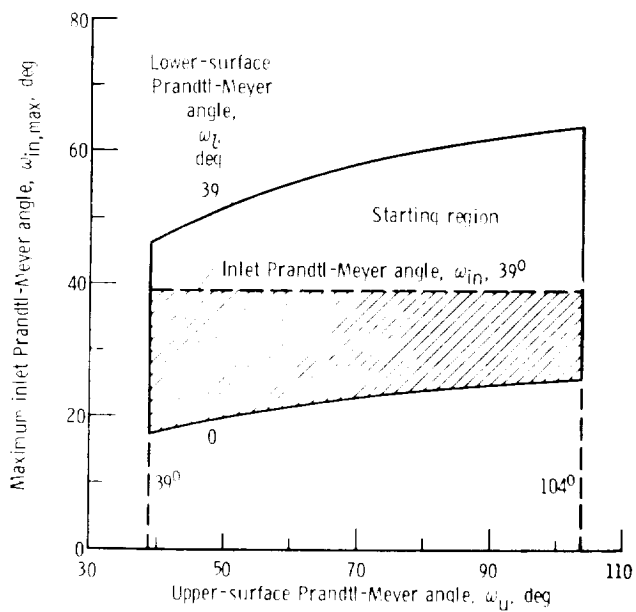


FIGURE 9-19.—Supersonic starting criterion applied to example turbine. Inlet Mach number 2.5; inlet Prandtl-Meyer angle,  $39^\circ$ ; inlet flow angle,  $65^\circ$ .

and passage profiles. To assure satisfactory starting for the given inlet conditions, the point representing the surface Prandtl-Meyer angles in figure 9-18 must lie on or above the ordinate corresponding to the inlet Prandtl-Meyer angle. In general, the supersonic starting condition places a severe restriction on the permissible design values of surface Mach numbers. This restriction is best seen from an example.

Suppose a blade is to be designed for the following conditions: (1)  $\gamma=1.4$ ; (2)  $M_{in}=M_{ex}=2.5$  ( $\omega_{in}=\omega_{ex}=39^\circ$ ); and (3)  $\theta_{in}=\theta_{ex}=65^\circ$ . It is first noted that  $\omega_i$  can vary from  $0^\circ$  to  $39^\circ$ , and that  $\omega_u$  can vary from  $39^\circ$  to  $104^\circ$ . The  $0^\circ$  limit on  $\omega_i$  is due to the fact that the flow must remain at least sonic; the  $104^\circ$  limit on  $\omega_u$  is due to the fact that the inlet transition turning cannot exceed the inlet flow angle of  $65^\circ$  ( $39^\circ+65^\circ=104^\circ$ ). In figure 9-19, the maximum inlet Prandtl-Meyer angle  $\omega_{in, max}$  is plotted as a function of  $\omega_u$  for this example. For clarity, only the bounds of  $\omega_i$  and  $\omega_u$  discussed previously are shown. The dashed line represents  $\omega_{in}=39^\circ$ , and the region shown crosshatched would not be permissible for design purposes because of supersonic starting considerations. Flow separation consideration will, in general, limit the maximum value of  $\omega_u$  to much lower values than the limit indicated in the figure.

### Supersonic Turbine Performance

Experimental performance data for supersonic turbines are reported in references 10 to 14. The variation in supersonic-turbine efficiency with blade-jet speed ratio (blade speed divided by ideal velocity corresponding to turbine inlet-total- to exit-static-pressure ratio) is illustrated in figure 9-20, which presents the data for the partial-admission turbine of reference 14. For any given speed, efficiency is maximum at about design pressure ratio and falls off rapidly as pressure ratio is decreased. The variation in maximum efficiency (circles in fig. 9-20) with blade-jet speed ratio is similar to that for a subsonic turbine. If this were a subsonic turbine, the efficiencies at the lower pressure ratios would have fallen on the envelope curve. The decrease in supersonic-turbine efficiency at the

## SUPersonic TURBINES

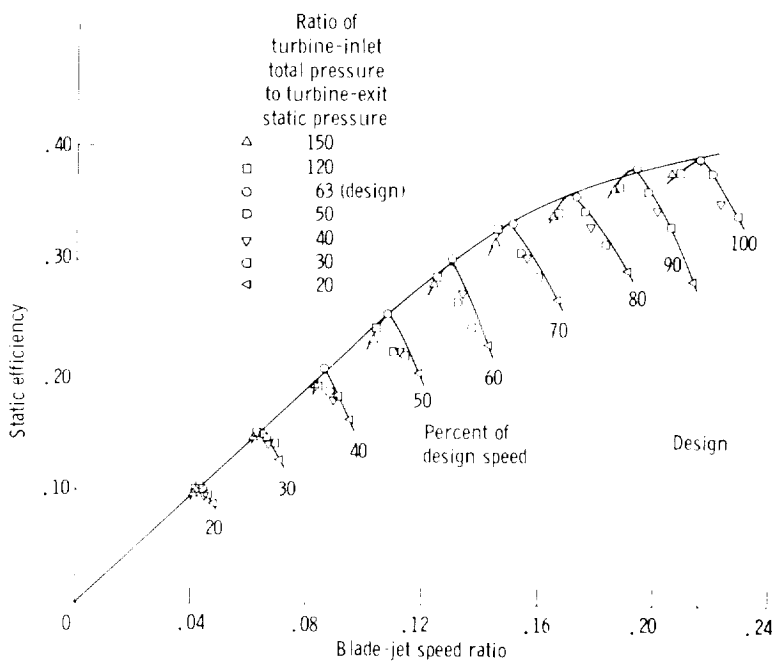


**FIGURE 9-20.—**Static efficiency of turbine as function of blade-jet speed ratio for constant speeds.

lower pressure ratios is due to the shocks occurring in the underexpanded stator nozzles.

The variation in static pressure throughout the stator nozzle of the turbine of reference 14 is shown in figure 9-21. The formation of the shock waves in the underexpanded nozzle is readily apparent. It can also be seen from this figure that at pressure ratios near design, the divergent section of the nozzle performed as expected, but the pressure did not remain constant in the straight section. There was some overexpansion followed by some compression. This same behavior was found in the data of reference 10.

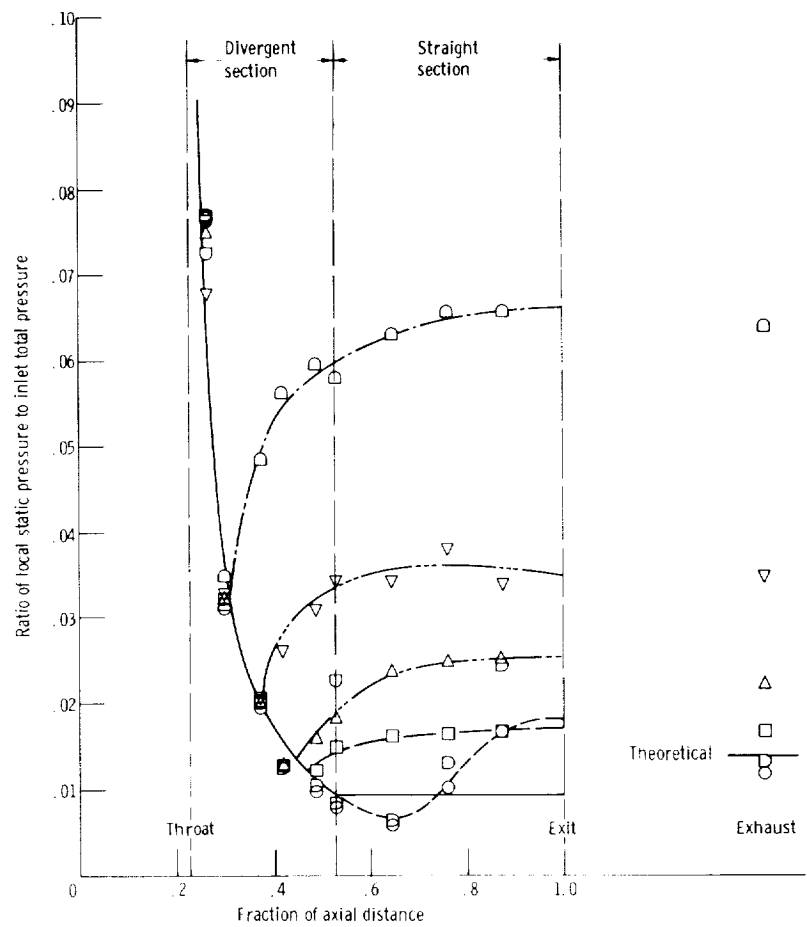


FIGURE 9-21.—Variation of nozzle pressure ratio with axial distance in nozzle for constant ratios of nozzle exit static pressure to inlet total pressure.

## REFERENCES

1. SHAPIRO, ASCHER H.: The Dynamics and Thermodynamics of Compressible Fluid Flow. vol. 1. Ronald Press Co., 1953.
2. LIEPMANN, HANS WOLFGANG; AND PUCKETT, ALLEN E.: Introduction to Aerodynamics of a Compressible Fluid. John Wiley & Sons, 1947.
3. VANCO, MICHAEL R.; AND GOLDMAN, LOUIS J.: Computer Program for Design of Two-Dimensional Supersonic Nozzle with Sharp-Edged Throat. NASA TM X-1502, 1968.
4. GOLDMAN, LOUIS J.; AND VANCO, MICHAEL R.; Computer Program for Design of Two-Dimensional Sharp-Edged-Throat Supersonic Nozzle with Boundary-Layer Correction. NASA TM X-2343, 1971.
5. BOXER, EMANUEL; STERRETT, JAMES R.; AND WŁODARSKI, JOHN: Application of Supersonic Vortex-Flow Theory to the Design of Supersonic Impulse Compressor- or Turbine-Blade Sections. NACA RM L52B06, 1952.
6. GOLDMAN, LOUIS J.; AND SCULLIN, VINCENT J.: Analytical Investigation of Supersonic Turbomachinery Blading. I—Computer Program for Blading Design. NASA TN D-4421, 1968.
7. STRATFORD, B. S.; AND SANSCHE, G. E.: Theory and Tunnel Tests of Rotor Blades for Supersonic Turbines. R&M 3275, Aero. Res. Council, 1962.
8. HORLOCK, J. H.: Axial Flow Turbines: Fluid Mechanics and Thermodynamics. Butterworths, 1966.
9. GOLDMAN, LOUIS J.; AND SCULLIN, VINCENT J.: Computer Program for Design of Two-Dimensional Supersonic Turbine Rotor Blades with Boundary-Layer Correction. NASA TM X-2434, 1971.
10. MOFFITT, THOMAS P.: Design and Experimental Investigation of a Single-Stage Turbine with a Rotor Entering Relative Mach Number of 2. NACA RM E58F20a, 1958.
11. STABE, ROY G.; KLINE, JOHN F.; AND GIBBS, EDWARD H.: Cold-Air Performance Evaluation of a Scale-Model Fuel Pump Turbine for the M-1 Hydrogen-Oxygen Rocket Engine. NASA TN D-3819, 1967.
12. MOFFITT, THOMAS P.; AND KLAG, FREDERICK W., JR.: Experimental Investigation of Partial- and Full-Admission Characteristics of a Two-Stage Velocity-Compounded Turbine. NASA TM X-410, 1960.
13. JOHNSON, I. H.; AND DRANSFIELD, D. C.: The Test Performance of Highly Loaded Turbine Stages Designed for High Pressure Ratio. R&M 3242, Aero. Res. Council, 1962.
14. GOLDMAN, LOUIS J.: Experimental Investigation of a Low Reynolds Number Partial-Admission Single-Stage Supersonic Turbine. NASA TM X-2382, 1971.

## SYMBOLS

<i>A</i>	flow area along Mach wave, m <sup>2</sup> ; ft <sup>2</sup>
<i>a</i>	speed of sound, m/sec; ft/sec
<i>g</i>	conversion constant, 1; 32.17 (lbm)(ft)/(lbf)(sec <sup>2</sup> )
<i>M</i>	Mach number
<i>M*</i>	critical velocity ratio ( <i>V/V<sub>cr</sub></i> )
<i>p</i>	absolute pressure, N/m <sup>2</sup> ; lb/ft <sup>2</sup>
<i>u</i>	component of velocity parallel to initial flow direction, m/sec; ft/sec
<i>V</i>	velocity, m/sec; ft/sec
<i>V<sub>cr</sub></i>	critical velocity ( <i>M</i> =1), m/sec; ft/sec
<i>v</i>	component of velocity normal to initial flow direction, m/sec; ft/sec
<i>w</i>	mass flow rate, kg/sec; lb/sec
<i>β</i>	Mach angle, deg
<i>γ</i>	ratio of specific heat at constant pressure to specific heat at constant volume
<i>δ</i>	small change in flow direction, deg
<i>θ</i>	flow angle, deg
<i>ν</i>	Prandtl-Meyer angle, deg
<i>ρ</i>	density, kg/m <sup>3</sup> ; lb/ft <sup>3</sup>
<i>ω</i>	Prandtl-Meyer angle, deg

## Subscripts:

<i>ex</i>	rotor exit
<i>in</i>	rotor inlet
<i>l</i>	lower surface of blade
<i>max</i>	maximum
<i>n</i>	normal direction with respect to Mach wave
<i>r</i>	relative
<i>s</i>	isentropic
<i>t</i>	tangential direction with respect to Mach wave
<i>u</i>	upper surface of blade

## CHAPTER 10

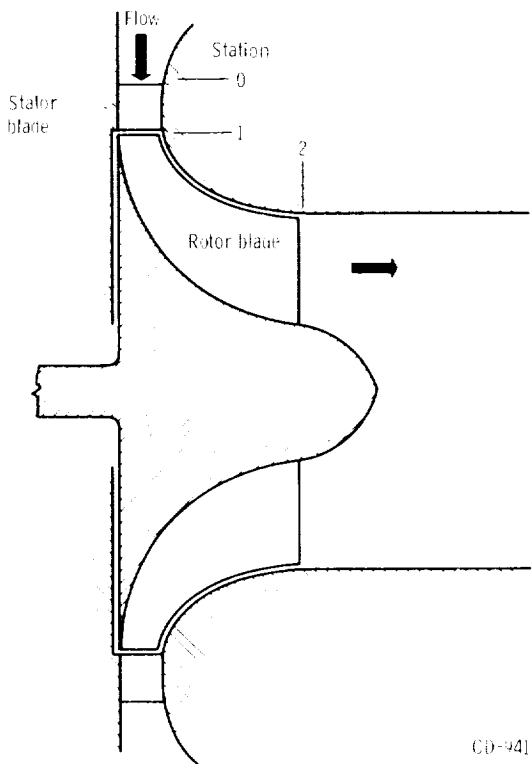
# Radial-Inflow Turbines

By Harold E. Rohlik

Radial-inflow turbines are suitable for many applications in aircraft, space power systems, and other systems where compact power sources are required. Turbines of this type have a number of desirable characteristics such as high efficiency, ease of manufacture, sturdy construction, and reliability. There is a substantial amount of information on radial-inflow turbines in the literature. References 1 to 6 are general in nature and cover most areas of the design and performance of these machines. In this chapter, the radial-inflow turbine is described, and its features are compared with those of an axial-flow turbine. In addition, design geometry and performance, blade design, and off-design performance are discussed.

Figure 10-1 shows a section through a typical radial-inflow turbine. The flow enters the stator radially and leaves the rotor axially. This turning of the flow takes place in the rotor passage, which is relatively long and narrow. In axial turbines, the blade aspect ratio, which is the ratio of blade height to chord, varies from about 1 to as much as 8. Radial turbine rotor and stator blades, on the other hand, generally have aspect ratios from 0.1 to 0.5.

A torus, which is a doughnut-shaped plenum, or a volute (shown in fig. 10-2), which is a spiral flow passage, usually surrounds the stator inlet. The torus is fed by a radial inlet pipe, while the volute is fed by a tangential inlet pipe. In the case of a volute, a prewhirl (tangential component of velocity) is imparted to the gas before it enters the stator blade row. This results in stator blades with little or no camber. It can be seen from figure 10-2 that the overall diameter of a radial-inflow turbine is considerably larger than the rotor diameter.



CD-9413

FIGURE 10-1.—Schematic cross section of radial-inflow turbine.

At the rotor inlet, where the flow velocity relative to the rotor has little or no tangential component ( $W_u \approx 0$ ), the rotor blades are usually straight and radial. This straight section of the rotor blade generally is rather highly loaded, since angular momentum  $rV_u$  (where  $r$  is the radius, and  $V_u$  is the tangential component of absolute velocity) here varies with the square of radius. (Since  $W_u \approx 0$ ,  $V_u = U \propto r$ , where  $U$  is the blade speed. Therefore,  $rV_u \propto r^2$ .) At the rotor exit, the blades are curved to turn the flow, so that the exit absolute velocity has little or no whirl.

Figure 10-3 shows the blading more clearly. The stator blade shape shows that prewhirl is developed in the inlet volute. Also, the low solidity (ratio of chord to spacing) and low aspect ratio that are generally used in the stators of radial turbines can be seen. The turbine shown here has splitter, or partial, blades between the full blades in the rotor. They are used in the radial part of the flow passage

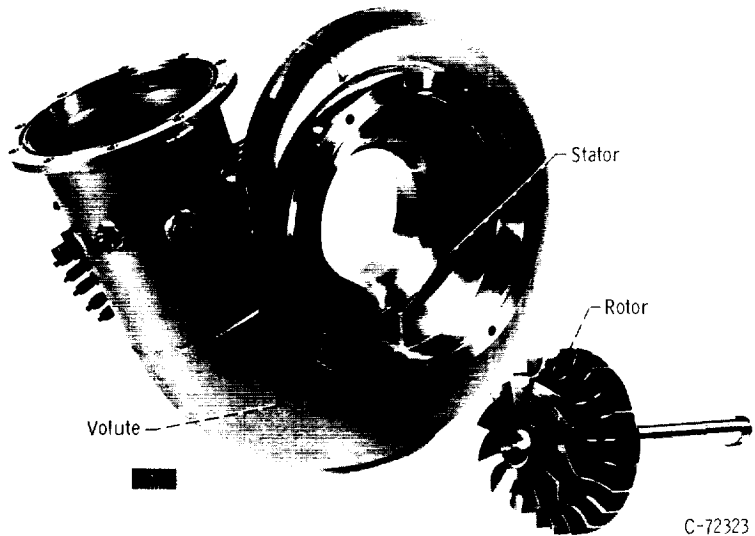
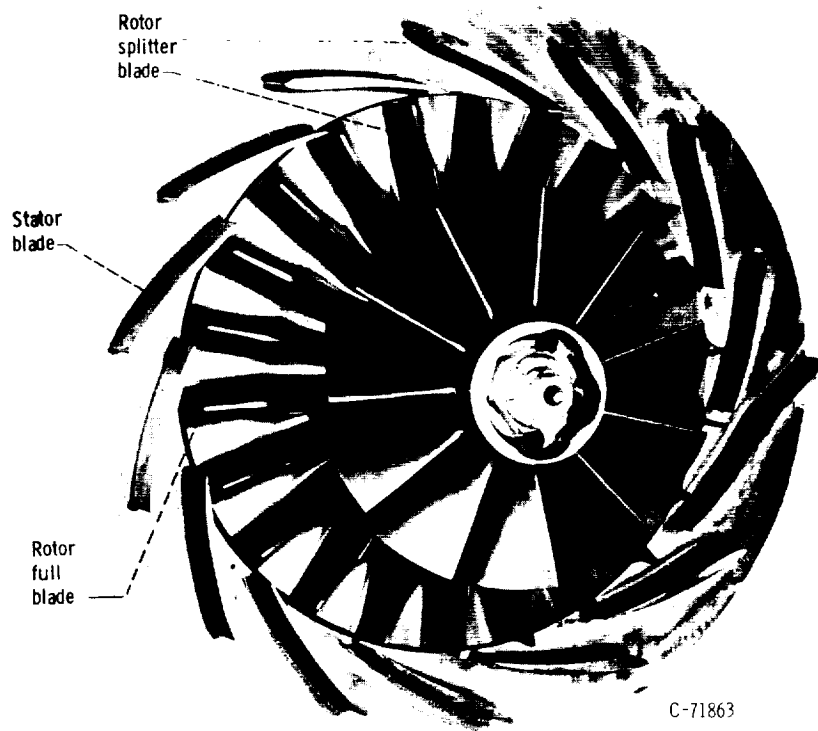


FIGURE 10-2.—Radial-inflow turbine.

to reduce the blade loading. Splitter blades are discussed further in the "BLADE DESIGN" section.

The expansion process in a radial turbine differs appreciably from that in an axial turbine because of the radius change in the rotor. The relative total temperature and pressure decrease with decreasing radius, as was discussed in chapter 2 of volume 1 (see eq. (2-31) and associated discussion). This is a distinct advantage for the radial turbine because it permits the use of a lower velocity level for a given overall expansion. This can be seen from the temperature-entropy diagram in figure 10-4, which shows the expansion through the rotor of a radial-inflow turbine. The change in relative total temperature  $T''$  and the corresponding change in relative total pressure  $p''$  are shown for the expansion. If this were an axial turbine ( $T'_1 = T'_2$ ), the  $p'_2$  line would be only slightly below the  $p'_1$  line (as shown in fig. 2-8 of ch. 2), because the difference between  $p'_1$  and  $p'_2$  is due only to rotor losses. For the radial turbine, as shown in figure 10-4, the  $p''_2$  line is farther removed from the  $p''_1$  line because the difference is due to both the rotor losses and the change in radius. Therefore,



C-71863

FIGURE 10-3.—Turbine stator and rotor assembly.

expansion from the same rotor inlet total pressure  $p_1''$  to the same exit static pressure  $p_2$  would require a higher relative velocity  $W_2$  at the rotor exit in an axial turbine than in a radial turbine (larger vertical distance between  $p_2''$  and  $p_2$  for an axial turbine.) Since fluid friction losses in a rotor increase approximately with the square of the relative gas velocity, the advantage of a lower level of velocity is clear.

A radial-turbine velocity diagram is shown in figure 10-5 for a turbine with prewhirl in the inlet volute and a mean diameter ratio (exit-mean to inlet) of about 0.5. The difference between the blade speeds  $U_1$  and  $U_2$  is very evident. For a typical zero-exit-whirl velocity diagram, the relative kinetic energy  $W_2^2$  leaving the rotor would be approximately three times as high if  $U_2$  equaled  $U_1$ , as in an axial turbine.

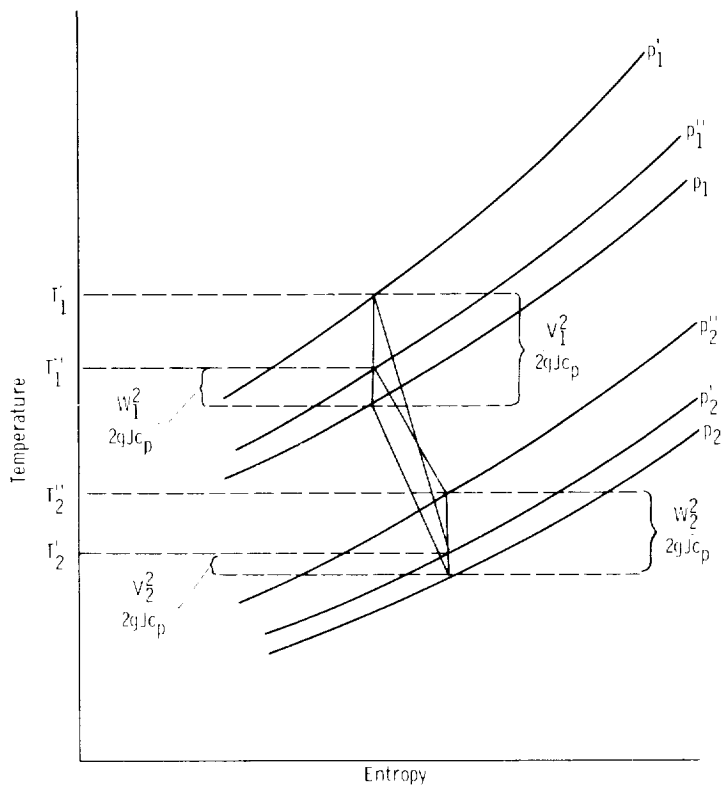


FIGURE 10-4.—Temperature-entropy diagram for a radial-inflow turbine rotor.

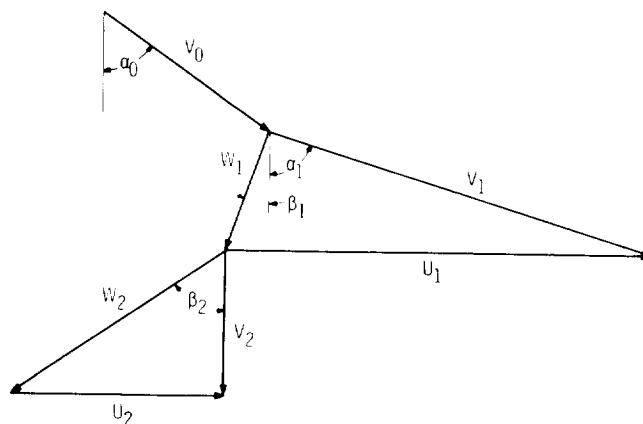


FIGURE 10-5.—Velocity diagram.

## OVERALL DESIGN CHARACTERISTICS

## Optimum Incidence

Since the blades are radial at the rotor inlet, the inlet flow angle  $\beta_1$  shown in figure 10-5 is an incidence angle. There is some incidence angle that provides optimum flow conditions at the rotor-blade leading edge. This angle has a value sometimes as high as  $40^\circ$  with a radial blade. This optimum incidence condition is analogous to the "slip" factor in a centrifugal compressor, and is associated with the unloading of the blade near the tip and the distribution of mass flow in the rotor passage. Before the flow is influenced by the rotor blades, it is circumferentially uniform. Blade loading then produces a large static-pressure gradient across the passage, so that there is a streamline shift toward the suction surface. Stream-function flow analyses of this flow condition show that the streamline pattern properly locates the inlet stagnation point when there is an "optimum" angle  $\beta_1$ . This pattern is shown schematically in figure 10-6. Note that the flow at the stagnation point is approximately radial. If this were not so, the flow would tend to separate from the suction surface near the leading edge, causing excessive loss. The relation between  $V_{u,1}$  and  $U_1$  has been studied analytically and experimentally in both compressors and turbines. It has

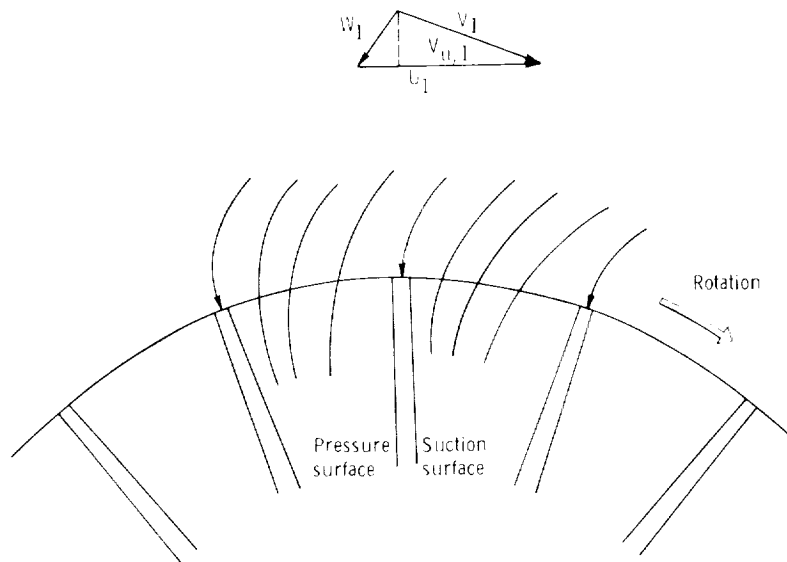


FIGURE 10-6.—Streamline flow at rotor inlet.

been determined that there is an optimum ratio of  $V_{u,1}$  to  $U_1$ . This optimum ratio depends on blade loading and, consequently, blade number and is often expressed as

$$\frac{V_{u,1}}{U_1} = 1 - \frac{2}{n} \quad (10-1)$$

where  $n$  is the number of blades (total of full blades plus splitter blades).

### Effect of Specific Speed on Design Geometry and Performance

The specific speed parameter  $N_s$  (derived and discussed in ch. 2 of vol. 1) is given by the equation

$$N_s = \frac{NQ_2^{1/2}}{H^{3/4}} \quad (10-2)$$

where

$N$  rotative speed, rad/sec; rev/min

$Q_2$  volume flow rate at turbine exit, m<sup>3</sup>/sec; ft<sup>3</sup>/sec

$H$  ideal work, or head, based on inlet and exit total pressures, J/kg; (ft)(lbf)/lbm

In its most commonly used form (with the stated U.S. customary units), it is not truly dimensionless. Specific speed is independent of size and may be considered as a shape parameter that expresses geometric and velocity-diagram similarity.

*Analytical study.*—The effect of specific speed on efficiency may be examined by substituting for  $N$ ,  $Q_2$ , and  $H$  as follows:

$$N = \frac{KU_1}{\pi D_1} \quad (10-3)$$

$$Q_2 = \pi D_2 h_2 V_2 \quad (10-4)$$

$$H = \frac{V_i^2}{2g} \left( \frac{\Delta h'}{\Delta h} \right)_{id} \quad (10-5)$$

where

$K$  dimensional constant,  $2\pi$  rad/rev; 60 sec/min

$D_1$  rotor inlet (tip) diameter, m; ft

$D_2$  rotor-exit mean-section diameter, m; ft

$h_2$  rotor-exit passage height, m; ft

$V_2$  rotor-exit fluid velocity (assumed to be in axial direction), m/sec; ft/sec

$V_i$  ideal jet speed, based on inlet-total to exit-static pressure ratio, m/sec; ft/sec

$g$  conversion constant, 1; 32.17 (lbm)(ft)/(lbf)(sec<sup>2</sup>)

$\Delta h'_{id}$  ideal work based on inlet-total and exit-total pressures, J/kg;  
Btu/lb

$\Delta h_{id}$  ideal work based on inlet-total and exit-static pressures, J/kg;  
Btu/lb

These substitutions and some manipulation result in the following expression for specific speed:

$$N_s = (\text{Constant}) \left( \frac{\Delta h}{\Delta h'} \right)_{id}^{3/4} \left( \frac{U_1}{V_j} \right)^{3/2} \left( \frac{V}{U} \right)_2^{1/2} \left( \frac{D_2}{D_1} \right)^{3/2} \left( \frac{h}{D} \right)_2^{1/2} \quad (10-6)$$

The terms of equation (10-6) are related to velocity-diagram characteristics and overall geometry. Any specific speed value can be achieved by an infinite number of combinations of these ratio terms. A large number of these combinations were examined analytically in reference 7 to determine optimum combinations over a wide range of specific speed.

The analysis of reference 7 related losses to mean-diameter flow properties, neglecting hub-to-shroud variations. The losses considered were those caused by the stator and rotor boundary layers, blade-to-shroud clearance, windage on the back of the rotor, and the exit kinetic energy. The number of rotor blades was varied with stator-exit flow angle  $\alpha_1$  (in degrees) according to the equation

$$n = 0.03 (\alpha_1 - 57)^2 + 12 \quad (10-7)$$

in order to provide the minimum number that would avoid separation. This was the total number of blades (full plus splitter) used in equation (10-1) to establish the rotor incidence angle. Other assumptions included a favorable reaction ( $W_2 = 2W_1$ ), zero exit whirl ( $V_{u,2} = 0$ ), a maximum limit of 0.7 for  $D_{t,2}/D_1$ , and a minimum limit of 0.4 for  $(D_h/D_t)_2$ .

The effects of geometry and velocity-diagram characteristics were examined by calculating the previously mentioned losses for a large number of combinations of stator-exit flow angle  $\alpha_1$ , stator-blade-height to rotor-inlet-diameter ratio  $h_1/D_1$ , and rotor-exit to rotor-inlet diameter ratio  $D_{t,2}/D_1$  at three rotor-tip critical velocity ratios ( $U/V_c$ )<sub>1</sub>. The static efficiency was then plotted against specific speed. For the range of values used in the study, all of the calculated points fell in the shaded areas shown in figure 10-7. Stator-exit flow angle is seen to be a prime determinant of efficiency, which falls into a small region for each stator-exit flow angle. The boundaries of each region are set by the extreme values of input variables and by the assumed geometric limits. For any given value of specific speed, there can be a large variation in static efficiency, as much as 45 to 50 points for some values. The dashed curve is the envelope of all the computed static

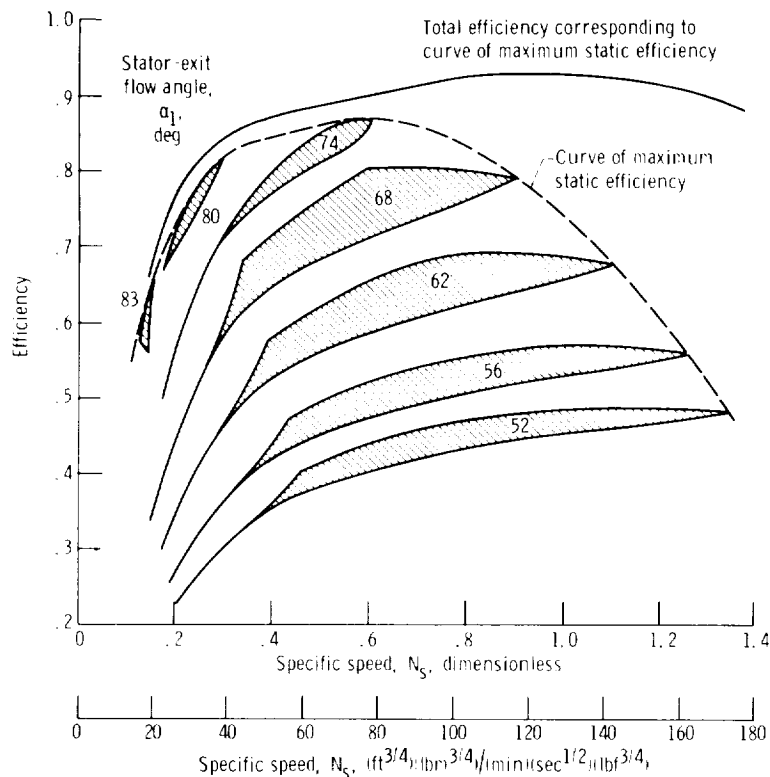


FIGURE 10-7.—Effect of specific speed on computed design-point efficiency.  
(Data from ref. 7.)

efficiencies, and the solid curve above it represents the corresponding total efficiencies. The computed values of efficiency do not necessarily represent achievable values, because there are many assumptions associated with the loss model used in the study of reference 7. The primary concern of that study, however, was to determine the optimum geometry and velocity ratios.

Most of the geometric and velocity ratios vary continuously along the envelope curves. The optimum values of some of these ratios as functions of specific speed are presented in figures 10-8 to 10-11. Figure 10-8 shows that the optimum stator-exit flow angle is large at low specific speed and decreases (opens to a larger flow area) with increasing specific speed. Figure 10-9 shows that the optimum ratio of stator-blade height to rotor-inlet diameter is small at low specific speed and increases with increasing specific speed until a maximum is reached at

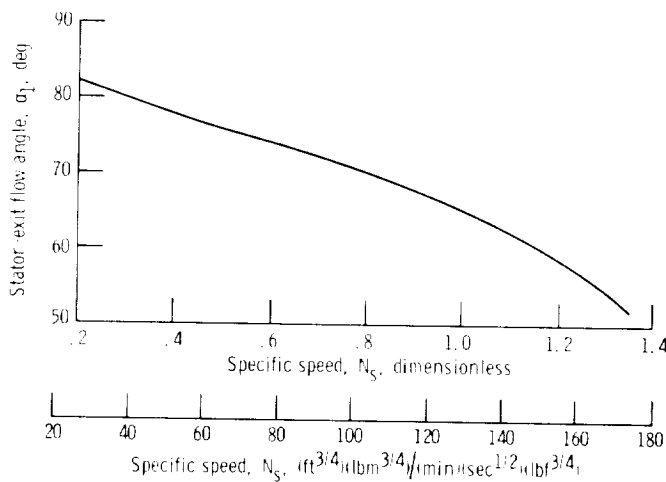


FIGURE 10-8.—Effect of specific speed on optimum stator-exit angle.  
(Data from ref. 7.)

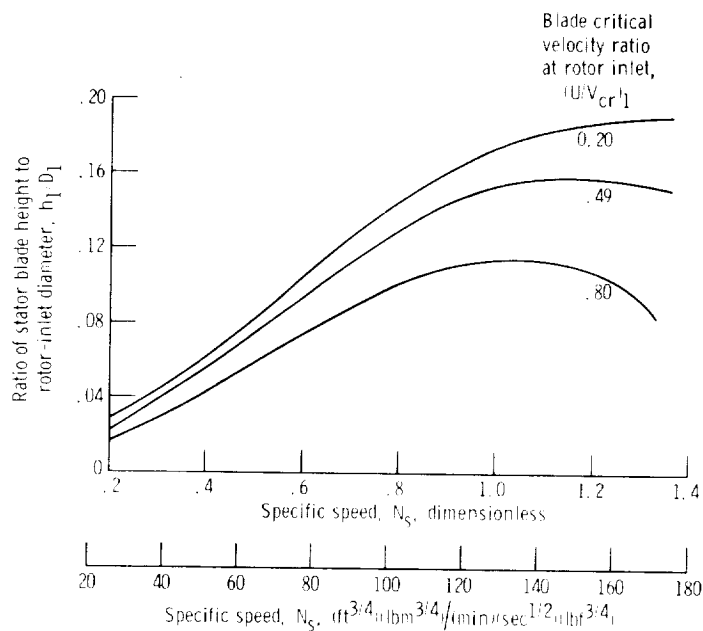


FIGURE 10-9.—Effect of specific speed and blade speed on optimum ratio of stator-blade height to rotor-inlet diameter. (Data from ref. 7.)

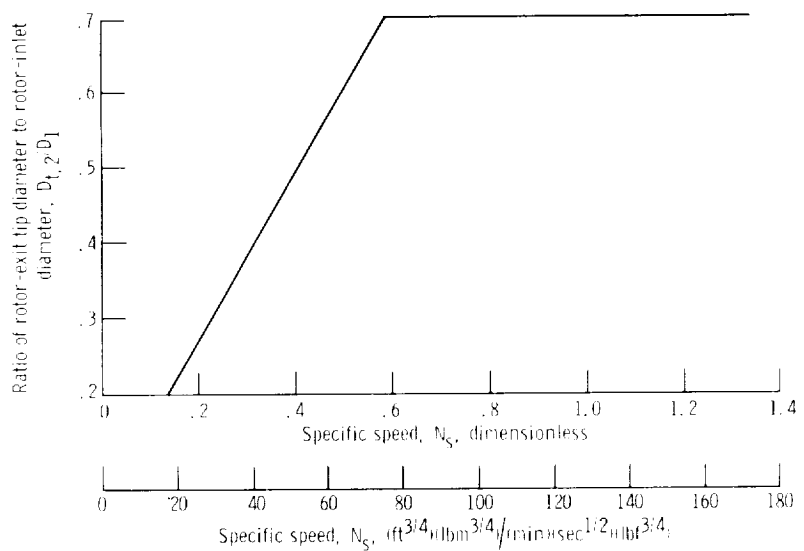


FIGURE 10-10.—Effect of specific speed on optimum ratio of rotor-exit tip diameter to rotor-inlet diameter. (Data from ref. 7.)

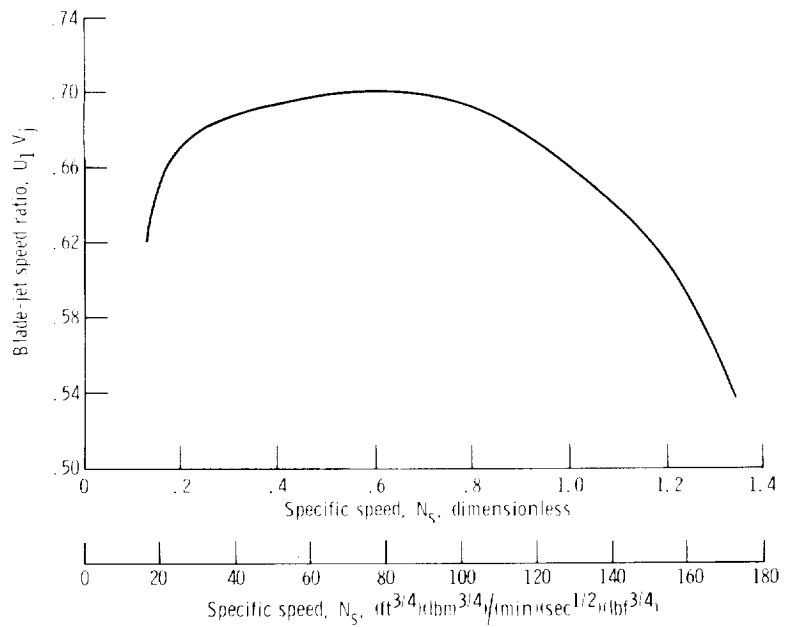
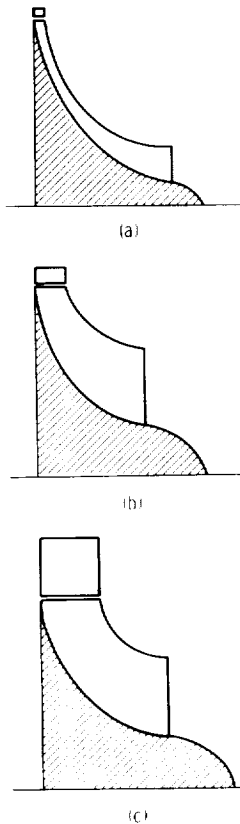


FIGURE 10-11.—Effect of specific speed on optimum blade-jet speed ratio. (Data from ref. 7.)

some value of specific speed depending on the overall level of velocity in the turbine. The only effect that compressibility has on the optimum geometric and velocity ratios is also shown in figure 10-9, where it is seen that higher velocity levels result in smaller ratios of stator-blade height to rotor-inlet diameter at any given specific speed. Figure 10-10 shows that the optimum ratio of rotor-exit tip diam-



- (a) Specific speed, 0.23;  $30 \text{ (ft}^{3/4}\text{)(lbm}^{3/4}\text{)/(min)(sec}^{1/2}\text{)(lbf}^{3/4}\text{)}$ . Stator-exit flow angle,  $81^\circ$ .
- (b) Specific speed, 0.54;  $70 \text{ (ft}^{3/4}\text{)(lbm}^{3/4}\text{)/(min)(sec}^{1/2}\text{)(lbf}^{3/4}\text{)}$ . Stator-exit flow angle,  $75^\circ$ .
- (c) Specific speed, 1.16;  $150 \text{ (ft}^{3/4}\text{)(lbm}^{3/4}\text{)/(min)(sec}^{1/2}\text{)(lbf}^{3/4}\text{)}$ . Stator-exit flow angle,  $60^\circ$ .

FIGURE 10-12.—Sections of radial turbines of maximum static efficiency.  
(Data from ref. 7.)

eter to rotor-inlet diameter is small at low specific speed and increases rapidly with increasing specific speed until the imposed limit of  $D_{t,2}/D_1=0.7$  is reached. It is seen from figure 10-11 that the optimum blade-jet speed ratio  $U_1/V_j$  varies with specific speed in a manner similar to the variation of static efficiency.

The optimum values shown in figures 10-8 to 10-11 can be used for the design of radial-inflow turbines. Sections of turbines with optimum geometries are shown in figure 10-12 for three values of specific speed. These sections show that specific speed is largely an index of flow capacity.

The design study of reference 7 also indicated the variation in the different losses along the curve of maximum static efficiency. This is shown in figure 10-13 for the range of specific speed covered. For low values of specific speed, the stator and rotor viscous losses are very

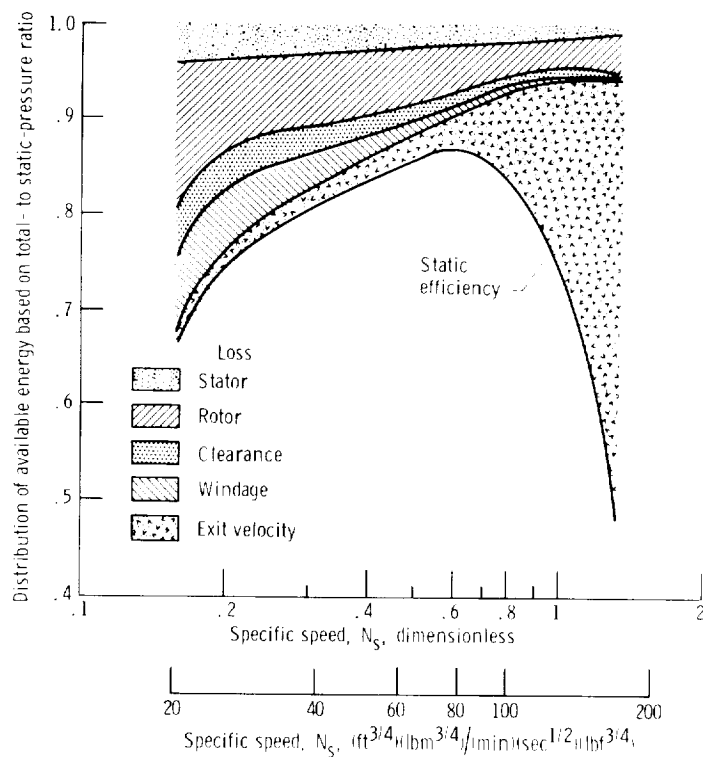
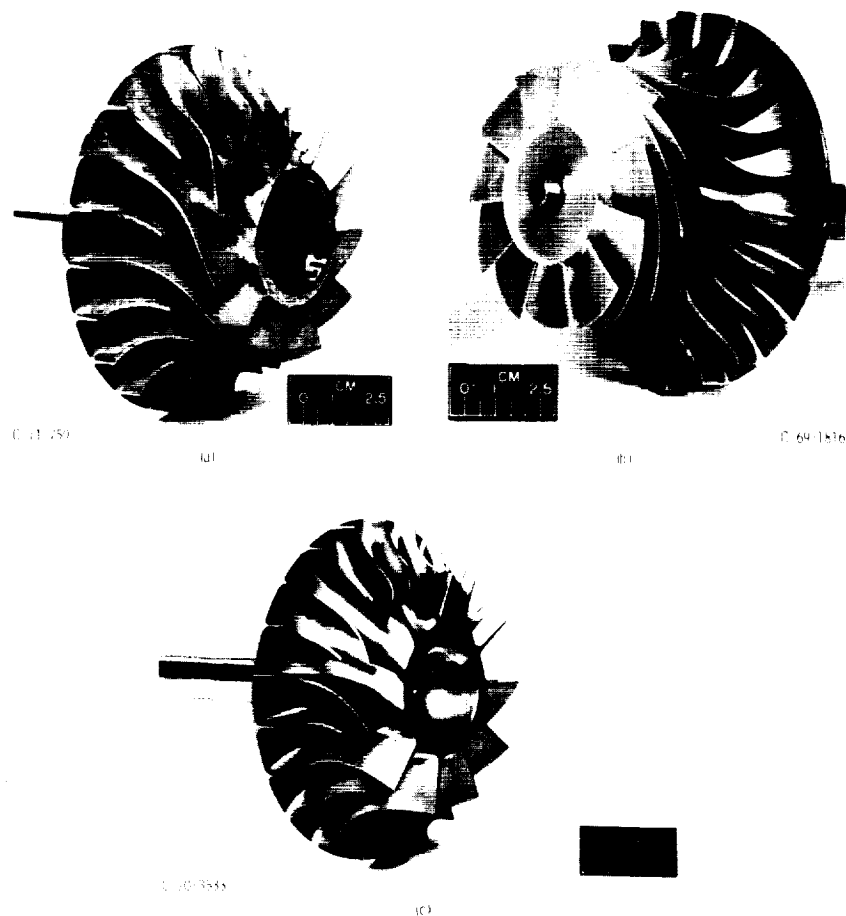


FIGURE 10-13.—Loss distribution along curve of maximum static efficiency.  
(Data from ref. 7.)

large because of the high ratio of wall area to flow area. Also, the clearance loss is large because the blade-to-shroud clearance is a relatively large fraction of the passage height. The windage loss, which depends on primarily the diameter and rotative speed, is also large at low specific speed because of the low flow rate. As specific speed increases, the stator and rotor losses, clearance loss, and windage loss all decrease because of the increased flow and area. The exit kinetic-energy loss becomes predominant at high values of specific speed.



(a) Design rotor.

(b) Rotor with exducer extension.

(c) Cut-back rotor.

FIGURE 10-14.—Rotor configurations used in specific-speed study of reference 8.

*Experimental study.*—In order to determine experimentally the effect of specific speed on turbine efficiency, a turbine was modified (ref. 8) to accept a series of stator blade rows with different numbers of blades and different blade angles. The rotor was fitted with an extension for reduced area operation and was also cut back for increased area operation. These modifications were used to vary the stator throat area from 20 to 144 percent of the design throat area and to vary the rotor throat area from 53 to 137 percent. This allowed the turbine to be operated over a large range of specific speed. Figure 10-14 shows the rotor as designed, with the reduced-area extension, and cut back. Details of the geometry, test results, and internal velocity calculations are given in reference 8.

Performance was determined experimentally for 13 combinations of stator area and rotor area. Figure 10-15 shows the envelopes of the

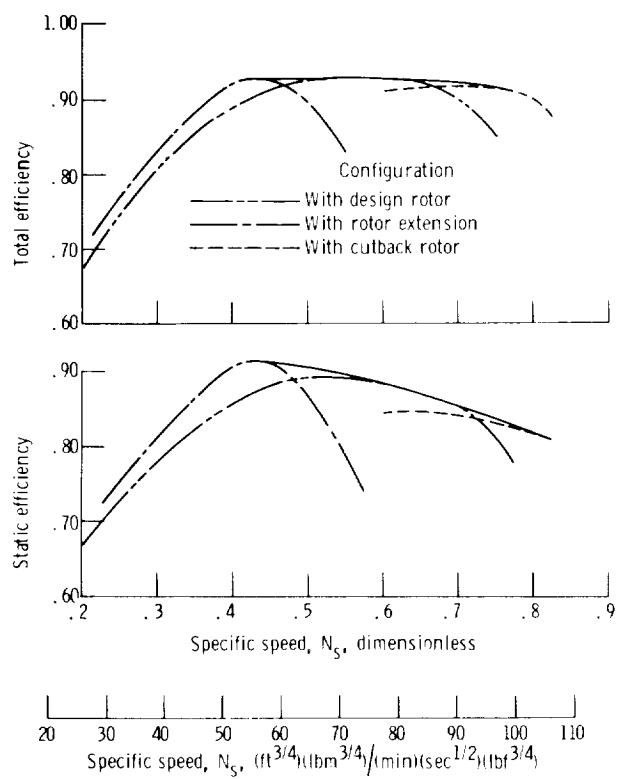


FIGURE 10-15.—Experimental variation of efficiency with specific speed. (Data from ref. 8.)

design-speed efficiency curves obtained with each rotor configuration, as well as the overall envelope curve. Specific speed for each stator-and-rotor combination was varied simply by varying overall pressure ratio at design speed. Note that total efficiencies over 0.90 were measured for specific speeds from 0.37 to 0.80 ( $48 \text{ to } 103 \text{ (ft}^{3/4}\text{)}$  ( $\text{lbf}^{3/4}\text{/min(sec}^{1/2}\text{)(lbf}^{3/4}\text{)}$ ). Maximum efficiencies were obtained when the ratio of stator throat area to rotor throat area was near the design ratio. Maximum static efficiencies of about 0.90 were measured in the specific speed range of about 0.4 to 0.5 ( $51 \text{ to } 65 \text{ (ft}^{3/4}\text{)(lbf}^{3/4}\text{/min(sec}^{1/2}\text{)(lbf}^{3/4}\text{)}$ ).

The investigation of reference 8 showed that a particular basic design could be used for a variety of applications (different specific speeds) and, even though the distribution of internal velocities is considerably off design, still yield high efficiency. Further, a radial turbine might be used to advantage in applications requiring variable stators. In this investigation, the volume flow rate varied by a factor of nearly three, with total efficiency remaining over 0.90. In addition, the parallel endwalls of the stator blade row minimize the potential for leakage.

#### **Effect of Blade-to-Shroud Clearance**

Clearance between the blade and the shroud must be adequate to avoid contact during speed and thermal transients, but it must be minimized to avoid loss of work due to flow bypassing the blades, generation of turbulence, and blade unloading. The efficiency loss due to blade-to-shroud clearance was one of the losses included in the previously discussed specific-speed analysis. For the losses shown in figure 10-13, the clearance loss was based on an average clearance as determined from constant values of rotor-inlet and rotor-exit clearance-to-diameter ratios.

The effects of blade-to-shroud clearance at the rotor inlet and at the rotor exit on radial-inflow turbine efficiency were determined experimentally in the study of reference 9. The results of these studies are presented in figure 10-16, which shows the effects of both inlet clearance and exit clearance. Increasing exit clearance causes a significantly greater loss in turbine efficiency than does a comparable increase in inlet clearance. It is the exit clearance that determines the fraction of the flow that is fully turned to the exit blade angle. Since it is the turbine stator that produces the rotor inlet whirl, design flow turning can be achieved even with a relatively large inlet clearance. With equal inlet and exit clearances (in terms of percent of passage height), there was about a 1-percent loss in efficiency for each percent increase in clearance.

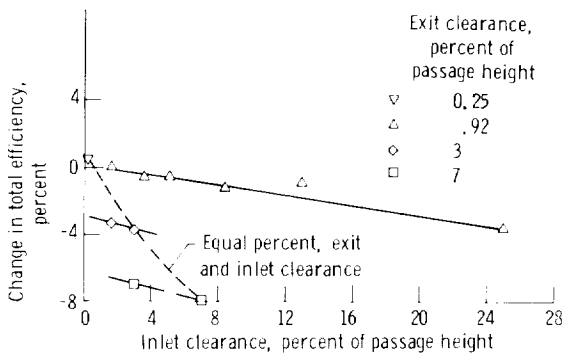


FIGURE 10-16.—Effects of inlet and exit clearances on total efficiency. (Data from ref. 9.)

An axial-flow turbine with the same flow conditions as a radial-inflow turbine would have a larger relative clearance (percent of rotor-exit passage height) than would the radial-inflow turbine. The larger rotor-exit diameter of the axial-flow turbine would result in a larger absolute clearance (since required clearance is largely a function of diameter) and a smaller passage height (in order to have same annulus area). This may be one of the reasons, along with the lower kinetic-energy level previously discussed, for the efficiency advantage of a radial-inflow turbine over a small axial-flow turbine for the same application.

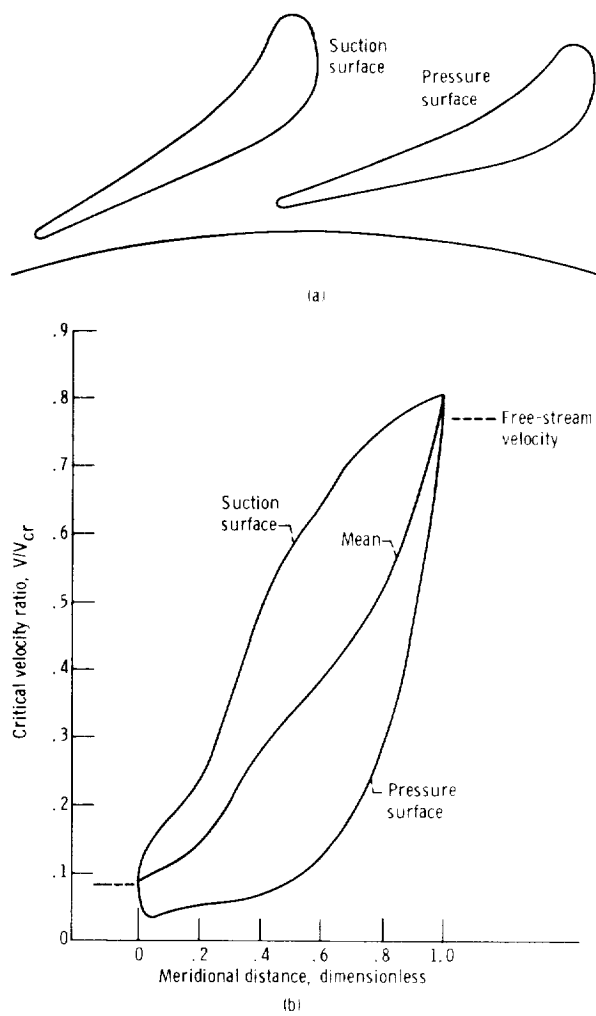
## BLADE DESIGN

The curves (figs. 10-8 to 10-11) relating turbine geometry and velocity ratios to specific speed are useful in preliminary design studies for a particular turbine problem. They can be used to determine turbine size and shape, as well as the design velocity diagram. The next part of any design problem involves the examination of internal flow in order to determine the best stator and rotor blade profiles. The methods and computer programs discussed in chapter 5 (vol. 2) are used for this purpose.

### Internal Flow Analysis

*Stator.*—Stator blade aerodynamic design is relatively straightforward. Typically, the blades have relatively little camber, long chords, and parallel endwalls. A long chord is usually specified because large blade profiles are easier to machine and because the small number

of blades (long chord means large spacing for a given solidity) means lower cost. Also, long chords are desirable because the stator blades serve as structural supports for the shroud. The aerodynamic penalty associated with the added endwall area (over that of short-chord



(a) Blades and passage.

(b) Surface velocities.

FIGURE 10-17.—Stator blades with surface-velocity distributions.

blades) is small because of the high reaction and the resultant favorable boundary-layer conditions.

A two-dimensional flow analysis may be used for the stator because of the parallel or near-parallel endwalls. The stream-function method described in reference 10 provides satisfactory subsonic and transonic solutions. Input information for the computer program includes flow rate, fluid properties and conditions, inlet and outlet flow angles, and a complete specification of blade geometry. The calculated blade-surface velocities are examined for smooth acceleration and magnitude and rate of local decelerations. Successive trials are made with varying solidity, blade number, and distribution of blade curvature until satisfactory velocity distributions are obtained for the pressure and suction surfaces.

Figure 10-17(a) shows the stator blade and passage profiles for a radial-inflow turbine in which the flow entering the stator has no prewhirl. The calculated suction- and pressure-surface velocities are shown in figure 10-17(b). Except for a small deceleration at the pressure-surface leading edge, the flow accelerates continuously on both surfaces. The calculated velocities near the trailing edge may be used to determine whether the blade row can accomplish the design turning. If the suction and pressure surface velocity curves remain open at the trailing edge, the input value for the free-stream exit flow angle specifies more turning than the blades can provide. Conversely, if the curves cross before the trailing edge, the blades will provide more turning than is specified by the input flow angle.

*Rotor.*—The design of rotor blading is appreciably more difficult than that of stator blading because of adverse pressure gradients (decelerations) encountered and because of the three-dimensionality of the design. The computer program of reference 11 is particularly suitable for screening various combinations of shroud contour, hub contour, number of blades, blade thickness distribution, and blade curvature. This approach, which was developed specifically for radial-inflow turbines, uses the velocity-gradient method, with integration of directional derivatives along fixed arbitrarily located straight lines (called quasi-orthogonals) that intersect all streamlines in the meridional plane. A meridional-plane section with several of these quasi-orthogonals is shown in figure 10-18. A complete meridional solution of velocities and streamlines is obtained. Blade-surface velocities are then calculated approximately in the program of reference 11 with an equation based on irrotational absolute flow and a linear velocity distribution between blades. These blade-surface velocities are used to evaluate the various geometries primarily on the basis of obtaining smooth accelerations and avoiding severe decelerations.

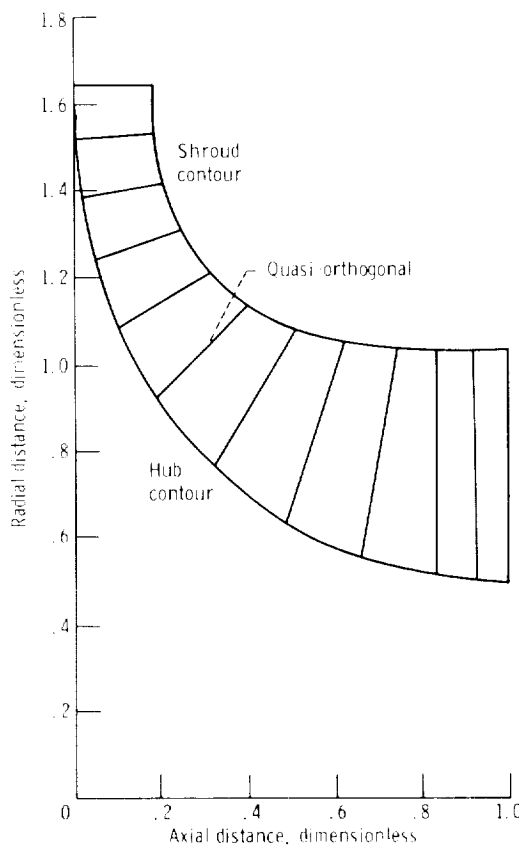
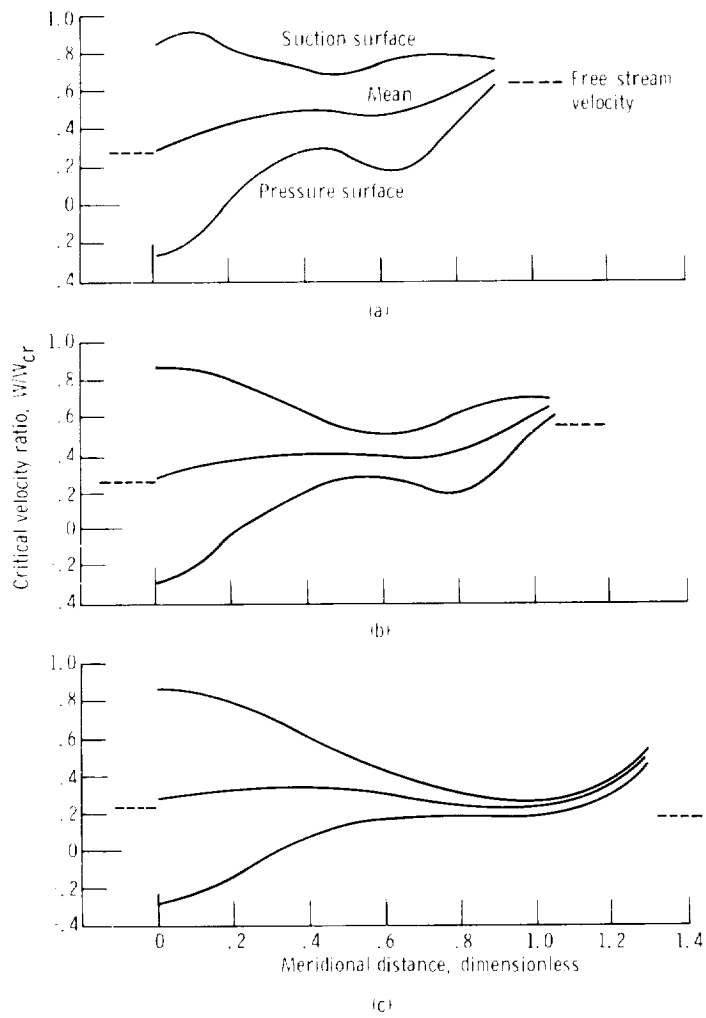


FIGURE 10-18.—Meridional section through radial-inflow turbine.

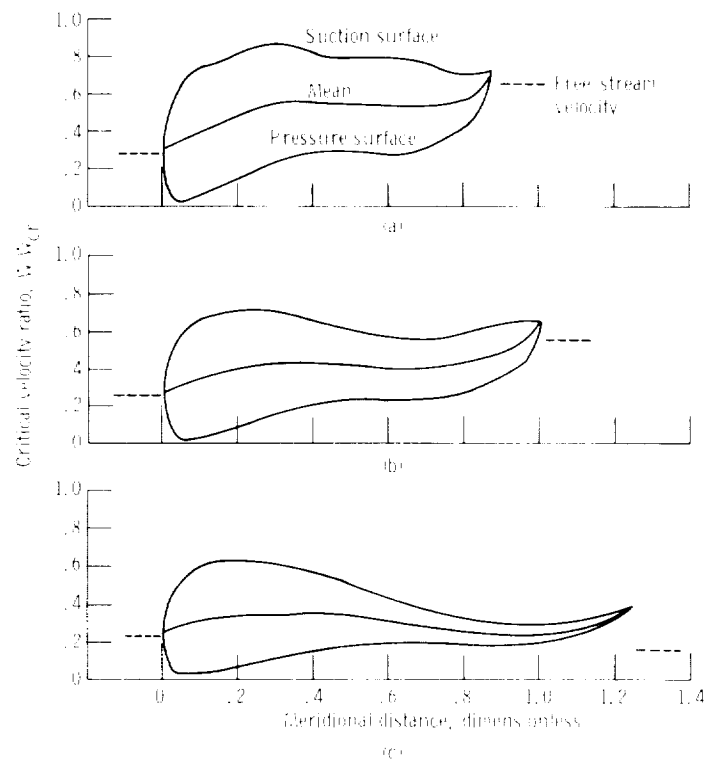
Blade-surface velocity distributions, as calculated from the meridional-plane solution of reference 11, at the hub, mean, and shroud sections of a radial-inflow turbine rotor are shown in figure 10-19. In figure 10-20 are shown the velocity distributions for the same blading, but as calculated by the stream-function method of reference 10. The surface velocities calculated from the meridional-plane solution agree fairly well with those of the stream-function solution over most of the blade. It can be seen, however, that an appreciable difference between solutions occurs at the leading and trailing edges. The linear velocity variation used in the meridional-plane solution method does not reflect the blade unloading that actually occurs in these regions. The stream-function method determines the blade surface velocities in a more rigorous manner. However, the meridional-



- (a) Shroud section.
- (b) Mean (50-percent streamline) section.
- (c) Hub section.

FIGURE 10-19.—Rotor-blade surface-velocity distributions from meridional-plane solution.

plane program (ref. 11) is easier and quicker to use than the stream-function program (ref. 10) and, thus, provides a better means for rapid screening of the many design variables. A lesser difference occurs in the intermediate portion of the blade passage. In the meridional-



(a) Shroud section.  
 (b) Mean (50-percent streamline) section.  
 (c) Hub section.

FIGURE 10-20.—Rotor-blade surface-velocity distributions from stream-function solution.

plane analysis, the flow is assumed to be circumferentially uniform, and the mean stream surface between the blades follows the prescribed mean blade surface. The stream-function solution considers blade-to-blade variations in the flow and defines a mean stream surface between blades that deviates from the mean blade surface. The distribution of blade loading, then, is also somewhat different.

Figures 10-19 and 10-20 illustrate the hub-to-shroud variations in the surface velocities and the blade loading, as well as the variations along the flow path. The blade is more heavily loaded along the shroud than elsewhere because of the lower solidity and the shorter flow path. Also, the shroud is a region of high flow. Therefore, the shroud is generally considered the most critical region and is examined most

carefully for favorable blade-surface velocity distributions. The loading near the rotor inlet, where the flow is nearly radial, is considerably higher than the loading near the rotor exit, where the flow is nearly axial. The high loading at the inlet is due primarily to the previously discussed rapid change in angular momentum ( $rV_u \propto r^2$ ) in that section. This high loading near the inlet could be reduced by 50 percent through the use of splitters, which are discussed in the next section. The rear part of the hub surface shows a very low blade loading. This results principally from the long flow path and the great decrease in blade spacing from inlet to exit at the hub section. In this particular turbine, the blade spacing decreased by about 75 percent.

### Splitter Blades

As indicated previously, the blade loading is highest at the rotor inlet, where the flow is radially inward. If this loading is excessive, as indicated by negative velocities calculated for the pressure surface and/or large decelerations on the suction surface, it can be reduced by using partial blades between the full blades in the radial part of the rotor. Such partial blades are shown in figure 10-3 and are commonly called splitter blades. When splitter blades are used, the reduced loading results in decreased boundary-layer losses per unit of surface area. However, there is now the additional surface area of the splitter blades to offset the reduced loss per unit area. A judgment must be made, therefore, as to whether the use of splitter blades will, on balance, be beneficial.

The effect of splitter blades on turbine performance was examined experimentally in the study of reference 12. A turbine designed with splitter blades was built and tested. The splitter blades then were removed, thereby doubling the blade loading in the upstream half of the rotor. Channel velocities were calculated for both cases. When the splitters were removed, calculated negative velocities on the pressure side of the blade indicated a reverse-flow eddy extending from the hub almost to the meridional 50-percent streamline, and a large increase in loading upstream of what had been the splitter trailing-edge location.

Turbine performance data (ref. 12) taken over a range of speed and pressure ratio showed very little difference in efficiency between the splitter and the no-splitter cases. The loss increase due to the loading increase when the splitters were removed was apparently offset by the reduced surface area. This result and the previously discussed effect of blade-shroud clearance indicate an insensitivity of efficiency to poor flow conditions near the rotor leading edge. The low inlet velocity and favorable rotor reaction in a radial-inflow turbine provide an appreciable margin of tolerance toward such conditions.

## OFF-DESIGN PERFORMANCE

The performance characteristics of radial-inflow turbines are slightly different from those of axial-flow turbines. In an axial-flow turbine at all rotor speeds, the flow rate becomes zero only when the turbine pressure ratio (inlet-total- to exit-static-pressure) is one. In a radial-inflow turbine, however, this is only true at zero speed, as illustrated in figure 10-21. With rotation, the centrifugal force on the fluid within the rotor must be balanced by a pressure gradient directed radially inward. Therefore, there is some small pressure ratio across the turbine even with no flow (see fig. 10-21). This zero-flow pressure ratio increases with speed because of the increasing centrifugal force.

The variation of efficiency with blade-jet speed ratio, illustrated later in this section, for a radial-inflow turbine is very similar to that for an axial-flow turbine. The efficiency decrease as blade-jet speed ratio varies from the peak-efficiency point is slightly more rapid in the case of the radial-inflow turbine.

Prediction techniques for off-design performance are valuable in many situations. Estimated performance data can be useful in system studies to examine start transients and various operating conditions before any hardware is built. They can also be used to help select design modifications where system components may not be matched or to study the use of variable geometry. The approach in these off-design calculation methods is somewhat different from that used in design studies. In the off-design calculations, the geometry is

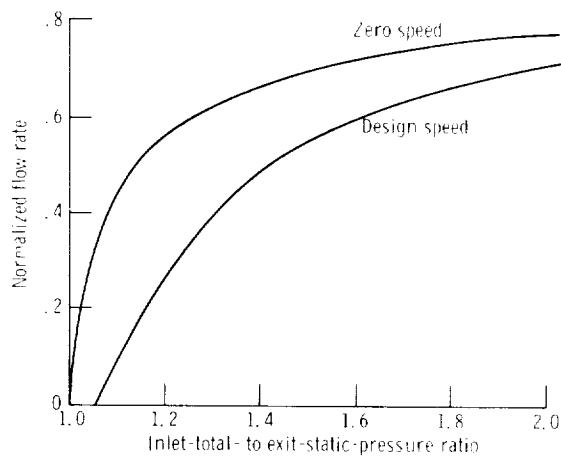


FIGURE 10-21.—Radial-inflow turbine flow characteristics.

fixed, the working-fluid inlet conditions are fixed, and the variables are blade speed and pressure ratio. Losses calculated for the stator and rotor depend on loss coefficients selected to force agreement between calculated and experimental or design values at the design operating point. Additional losses considered for subsonic flows are the rotor incidence loss and the exit kinetic-energy loss.

A radial-inflow turbine off-design performance calculation method developed at the NASA Lewis Research Center is described in reference 13, and the associated computer program is presented in reference 14. Figures 10-22 and 10-23 illustrate results obtained from a modified version of this computer program by presenting calculated performance over a range of speed and pressure ratio and comparing this with experimental performance. The mass flow estimation in figure 10-22 shows an accurate representation of the experimental variation of mass flow rate with pressure ratio. Total and static efficiencies plotted against blade-jet speed ratio are shown in figure 10-23. The calculated efficiencies are generally within 1 per-

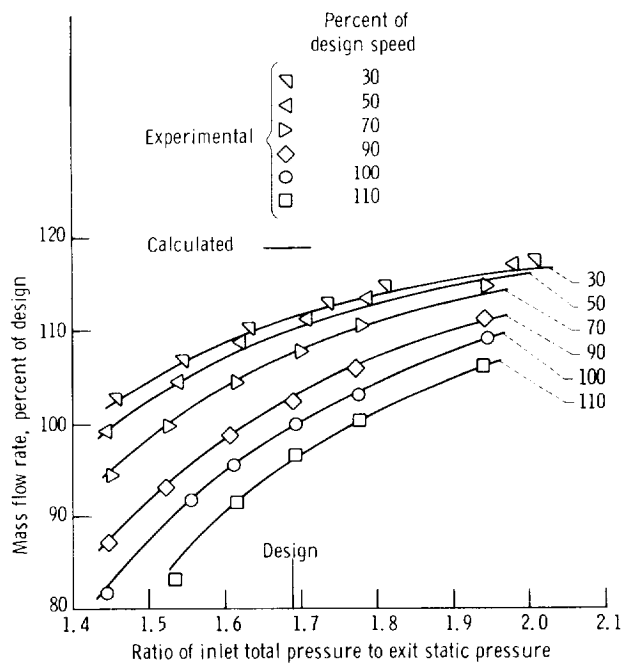


FIGURE 10-22.—Comparison of calculated and experimental flow rates for off-design operation.

cent and at most 2 percent of the experimental values. The calculations are sufficiently accurate to provide a valuable tool in the examination of overall system performance prior to fabrication and testing of the various components.

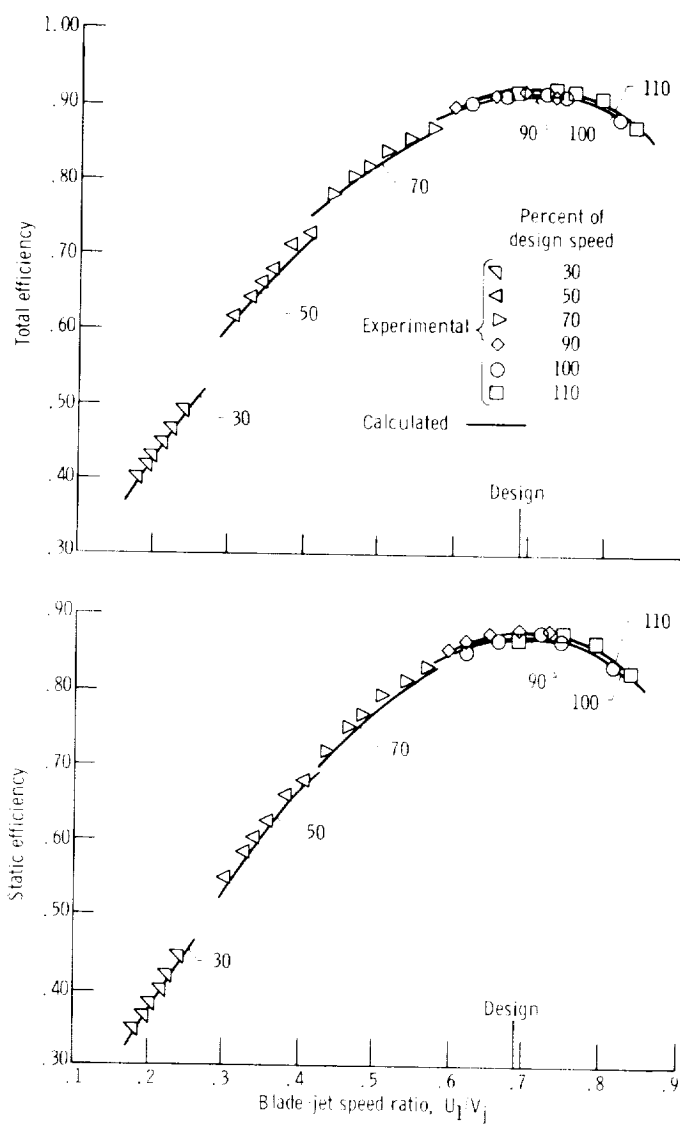


FIGURE 10-23.—Comparison of calculated and experimental efficiencies for off-design operation.

## REFERENCES

1. SAWYER, JOHN W., ed.: Gas Turbine Engineering Handbook. Gas Turbine Publications, Inc., 1966.
2. SHEPHERD, D. G.: Principles of Turbomachinery. Macmillan Co., 1956.
3. RODGERS, C.: Efficiency and Performance Characteristics of Radial Turbines. Paper 660754, SAE, 1966.
4. LAGNEAU, J. P.: Contribution to the Study of Advanced Small Radial Turbines. Int. Note 38, von Karman Institute of Fluid Dynamics, Mar. 1970.
5. WOOD, HOMER J.: Current Technology of Radial-Inflow Turbines for Compressible Fluids. J. Eng. Power, vol. 85, no. 1, Jan. 1963, pp. 72-83.
6. HIETT, G. F.; AND JOHNSON, I. H.: Experiments Concerning the Aerodynamic Performance of Inward Flow Radial Turbines. Paper 13 presented at the Thermodynamics and Fluid Mechanics Convention, Inst. Mech. Eng., London, Apr. 1964.
7. ROHLIK, HAROLD E.: Analytical Determination of Radial Inflow Turbine Design Geometry for Maximum Efficiency. NASA TN D-4384, 1968.
8. KOFSKEY, MILTON G.; AND NUSBAUM, WILLIAM J.: Effects of Specific Speed on Experimental Performance of a Radial-Inflow Turbine. NASA TN D-6605, 1972.
9. FUTRAL, SAMUEL M., JR.; AND HOLESKI, DONALD E.: Experimental Results of Varying the Blade-Shroud Clearance in a 6.02-Inch Radial-Inflow Turbine. NASA TN D-5513, 1970.
10. KATSANIS, THEODORE: Fortran Program for Calculating Transonic Velocities on a Blade-to-Blade Stream Surface of a Turbomachine. NASA TN D-5427, 1969.
11. KATSANIS, THEODORE: Use of Arbitrary Quasi-Orthogonals for Calculating Flow Distribution in the Meridional Plane of a Turbomachine. NASA TN D-2546, 1964.
12. FUTRAL, SAMUEL M., JR.; AND WASSERBAUER, CHARLES A.: Experimental Performance Evaluation of a 4.59-Inch Radial-Inflow Turbine With and Without Splitter Blades. NASA TN D-7015, 1970.
13. FUTRAL, SAMUEL M., JR.; AND WASSERBAUER, CHARLES A.: Off-Design Performance Prediction with Experimental Verification for a Radial-Inflow Turbine. NASA TN D-2621, 1965.
14. TODD, CARROLL A.; AND FUTRAL, SAMUEL M., JR.: A Fortran IV Program to Estimate the Off-Design Performance of Radial-Inflow Turbines. NASA TN D-5059, 1969.

## SYMBOLS

$c_p$	specific heat at constant pressure, J/(kg)(K) ; Btu/(lb)(°R)
$D$	diameter, m; ft
$g$	conversion constant, 1; 32.17 (lbm)(ft)/(lbf)(sec <sup>2</sup> )
$H$	ideal work, or head, based on inlet and exit total pressures, J/kg; (ft)(lbf)/lbm
$h$	passage height, m; ft
$\Delta h_{id}$	ideal work based on inlet-total and exit-static pressures, J/kg; Btu/lb
$\Delta h'_{id}$	ideal work based on inlet-total and exit-total pressures, J/kg; Btu/lb
$J$	conversion constant, 1; 778 (ft)(lb)/Btu
$K$	conversion constant, $2\pi$ rad/rev; 60 sec/min
$N$	rotative speed, rad/sec; rev/min
$N_s$	specific speed, dimensionless; $(ft^{3/4})(lbm^{3/4})/(min)(sec^{1/2})$ (lbf <sup>3/4</sup> )
$n$	total number of blades (full plus partial)
$p$	absolute pressure, N/m <sup>2</sup> ; lb/ft <sup>2</sup>
$Q$	volume flow rate, m <sup>3</sup> /sec; ft <sup>3</sup> /sec
$r$	radius, m; ft
$T$	absolute temperature, K; °R
$U$	blade speed, m/sec; ft/sec
$V$	absolute velocity, m/sec; ft/sec
$V_j$	ideal jet speed, based on inlet-total- to exit-static-pressure ratio, m/sec; ft/sec
$W$	relative velocity, m/sec; ft/sec
$\alpha$	fluid absolute flow angle measured from meridional plane, deg
$\beta$	fluid relative flow angle measured from meridional plane, deg

## Subscripts:

$cr$	critical flow condition (sonic velocity)
$h$	hub
$t$	tip
$u$	tangential component
$0$	at stator inlet
$1$	at stator exit or rotor inlet
$2$	at rotor exit

## Superscripts:

'	absolute total state
''	relative total state

## CHAPTER 11

# Turbine Cooling

By Raymond S. Colladay

The trend towards higher compressor pressure ratios and turbine-inlet temperatures to increase thrust and cycle efficiency has led to the necessity of cooling turbine blades, vanes, and end walls to meet life requirements. In this chapter, the term "vane" refers to a stator airfoil, while the term "blade" refers to the rotor airfoil. The hot combustor discharge gases enter the first vane row at peak temperatures frequently in excess of 1644 K (2500° F). In order to preserve the integrity of the turbine components in this hostile environment, air bled from the compressor is routed through the internal passages of the airfoils for cooling and then is dumped into the main gas stream at discrete locations around the blade or vane. This inevitably results in losses, both across the turbine and in the overall cycle thermodynamic efficiency. Consequently, very effective cooling schemes which utilize a minimum of air are required.

### GENERAL DESCRIPTION

In any turbine cooling design, one must make a complete energy balance on the blade (or vane, or end wall) to arrive at a cooling configuration which meets a given metal temperature limit. The analysis can be broken up conceptually into three parts: (1) The prediction of the heat flux to the blade from the hot gas stream. This requires an understanding of the boundary-layer development over the airfoil, the location of the transition from laminar to turbulent flow, the potential-flow velocity distribution, and the temperature profile (pattern factor) of the gas leaving the combustor (or other heat

source). (2) A steady-state or transient heat-conduction analysis to provide a detailed map of metal temperatures for blade-stress predictions. And, (3) the prediction of complex internal coolant flow paths for convection-cooling calculations. To maintain closure on the energy balance, the entire heat transfer process—convection from hot gas to blade, conduction through the blade wall, and convection from blade to coolant—must be treated simultaneously.

Let us for a moment oversimplify the problem by considering a one-dimensional model of a turbine-blade wall on the suction or pressure surface (see fig. 11-1). The heat flux to the blade can be expressed as a product of a hot-gas-side heat-transfer coefficient and the temperature difference between the gas and the wall. The gas temperature is expressed as an effective gas temperature, which for convection cooling is the adiabatic or recovery temperature (the temperature the surface would reach if there were no cooling). For purposes of this illustration, let the adiabatic wall temperature be the total gas temperature. Therefore,

$$q = h_g(T_g' - T_{w,o}) \quad (11-1)$$

where

$q$  heat flux,  $\text{W/m}^2$ ;  $\text{Btu}/(\text{hr})(\text{ft}^2)$

$h_g$  heat-transfer coefficient of hot gas,  $\text{W}/(\text{m}^2)(\text{K})$ ;  $\text{Btu}/(\text{hr})(\text{ft}^2)$   
 $(^\circ\text{R})$

$T_g'$  total temperature of hot gas,  $\text{K}$ ;  $^\circ\text{R}$

$T_{w,o}$  temperature of wall outer surface,  $\text{K}$ ;  $^\circ\text{R}$

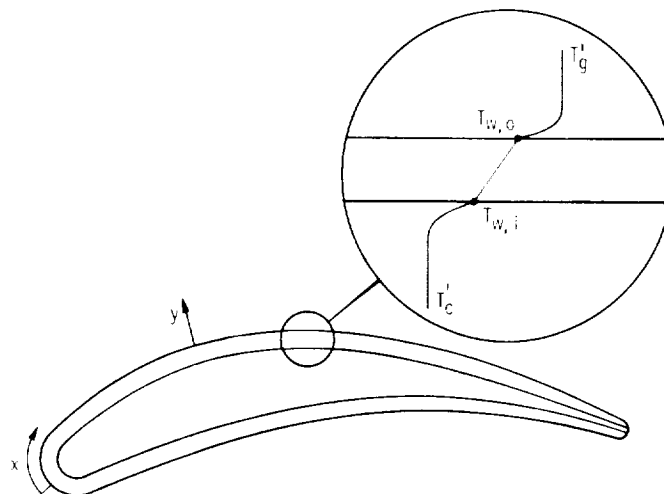


FIGURE 11-1.—Simplified one-dimensional model.

The heat removed from the wall, expressed in the same manner, is

$$q = h_c(T_{w,i} - T_c) \quad (11-2)$$

where

$h_c$  heat-transfer coefficient of coolant, W/(m<sup>2</sup>)(K); Btu/(hr)(ft<sup>2</sup>)  
(°R)

$T_{w,i}$  temperature of wall inner surface, K; °R

$T_c'$  total temperature of coolant, K; °R

The temperature drop through the wall is given by

$$q = -k_w \frac{dT}{dy} = \frac{k_w}{l} (T_{w,o} - T_{w,i}) \quad (11-3)$$

where

$k_w$  thermal conductivity of wall, W/(m)(K); Btu/(hr)(ft)(°R)

$y$  coordinate normal to wall surface, m; ft

$l$  wall thickness, m; ft

The second equality holds only for constant thermal conductivity.

As is frequently done in a first-order design, let the heat-transfer coefficient  $h_g$  be approximated by a correlation for flow over a flat plate. For a turbulent boundary layer, the flat-plate local Nusselt number  $Nu$  is given by

$$Nu_x = \frac{h_g x}{k_g} = 0.0296 Re_x^{0.8} Pr^{1/3} \quad (11-4)$$

where

$x$  distance along surface from leading edge of flat plate, m; ft

$Re_x$  Reynolds number based on distance  $x$

$Pr$  Prandtl number

The Reynolds number is defined as

$$Re_x = \frac{\rho u_g x}{\mu} \quad (11-5)$$

where

$\rho$  density, kg/m<sup>3</sup>; lb/ft<sup>3</sup>

$u_g$  component of hot-gas velocity in  $x$  direction, m/sec; ft/sec

$\mu$  viscosity, (N)(sec)/m<sup>2</sup>; lb/(ft)(sec)

and the Prandtl number is defined as

$$Pr = K \frac{\mu c_p}{k_g} \quad (11-6)$$

where

- $K$  dimensional constant, 1; 3600 sec/hr  
 $c_p$  specific heat at constant pressure, J/(kg)(K); Btu/(lb)(°R)

For an ideal gas, equation (11-5) can be substituted into equation (11-4) to yield

$$h_g = \frac{k}{x} (0.0296) Pr^{1/3} \left[ p_g' \sqrt{\frac{\gamma g}{RT_g}} \mu \left( 1 + \frac{\gamma-1}{2} M^2 \right)^{(\gamma+1)/2(\gamma-1)} \right]^{0.8} \quad (11-7)$$

where

- $p_g'$  total pressure of hot gas, N/m<sup>2</sup>; lb/ft<sup>2</sup>  
 $\gamma$  ratio of specific heat at constant pressure to specific heat at constant volume  
 $g$  conversion constant 1; 32.17 (lbm)(ft)/(lbf)(sec<sup>2</sup>)  
 $R$  gas constant, J/(kg)(K); (ft)(lbf)/(lbm)(°R)  
 $M$  Mach number

On the coolant side, a number of cooling schemes can be used, but in general,

$$h_c = C Re_c^{-m} Pr^n = C \left( \frac{w_c \mathcal{L}'}{\mathcal{A}_c \mu} \right)^m Pr^n \quad (11-8)$$

where

- $C$  constant dependent on coolant-passage geometry  
 $Re_c$  Reynolds number based on characteristic length  $\mathcal{L}'$   
 $w_c$  coolant mass flow rate, kg/sec; lb/sec  
 $\mathcal{L}'$  characteristic length for coolant passage, m; ft  
 $\mathcal{A}_c$  coolant-passage flow area, m<sup>2</sup>; ft<sup>2</sup>

For turbulent convection cooling,  $m=0.8$  and  $n=1/3$ . Since efficient cooling is desired, internal laminar flow ( $m=0.5$ ) should be avoided.

Now, consider the temperature profile through the blade wall, as depicted in figure 11-2, when the pressure  $p_g'$  and temperature  $T_g'$  of the hot gas are increased and the wall outer temperature  $T_{w,o}$  is kept constant (going from state 1 to state 2 in fig. 11-2). From equations (11-7) and (11-1), the heat flux to the blade increases with pressure to the 0.8 power and it increases with increasing gas temperature. The increased heat flux raises the temperature drop through the wall (i.e., decreases  $T_{w,i}$  for a fixed wall outer temperature  $T_{w,o}$ ). At the same time, the compressor bleed air temperature increases (higher compressor pressure ratio), so the temperature difference ( $T_{w,i}-T_c'$ ) available for convection cooling is sharply reduced. The heat flux  $q$  must be removed, otherwise the outer wall temperature will increase. Therefore,

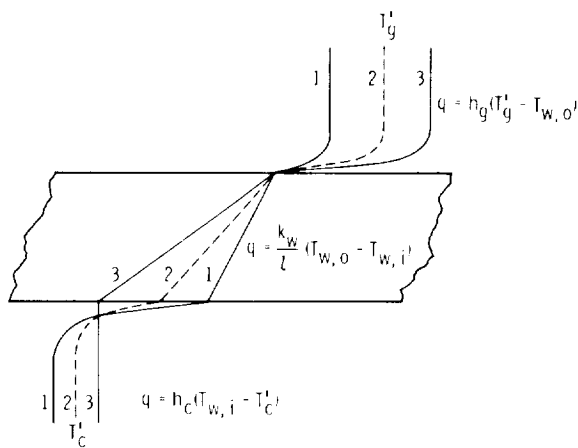


FIGURE 11-2.—Gas temperature and pressure effect on temperature drop through the wall.

$h_c$  must be increased by increasing the coolant flow  $w_c$ . The limiting case, as seen from figure 11-2, is state 3, where the inside wall temperature and coolant temperature are equal; therefore,  $h_c$  must be infinite, and an infinite coolant flow is required. Of course, this condition is impossible to achieve.

Because of limited internal passage size and the restriction on the quantity of cooling air available and on its supply pressure, a limit to the capabilities of plain convection cooling is apparent. Figure 11-3 from reference 1 shows the highly nonlinear increase in cooling air required for convection cooling as pressure and temperature increase.

The limit in the application of advanced convection cooling is about 1644 K (2500° F) hot-spot turbine-inlet temperature and about 20 atmospheres pressure. To exceed these gas conditions while maintaining reasonable operating blade-metal temperatures, cooling designs must incorporate film or transpiration cooling. Figure 11-3 shows the potential savings in cooling air with the use of transpiration cooling or combined film and convection cooling as compared to convection cooling only. Figure 11-4 illustrates the basic methods for air-cooling turbine components (figs. 11-4(a) to (e)), and it also shows examples of blades cooled by one or more of these cooling methods (figs. 11-4(f) to (i)).

Film cooling is an effective way to protect the surface from the hot gas stream by directing cooling air into the boundary layer to provide a protective, cool film along the surface. The effective gas temperature

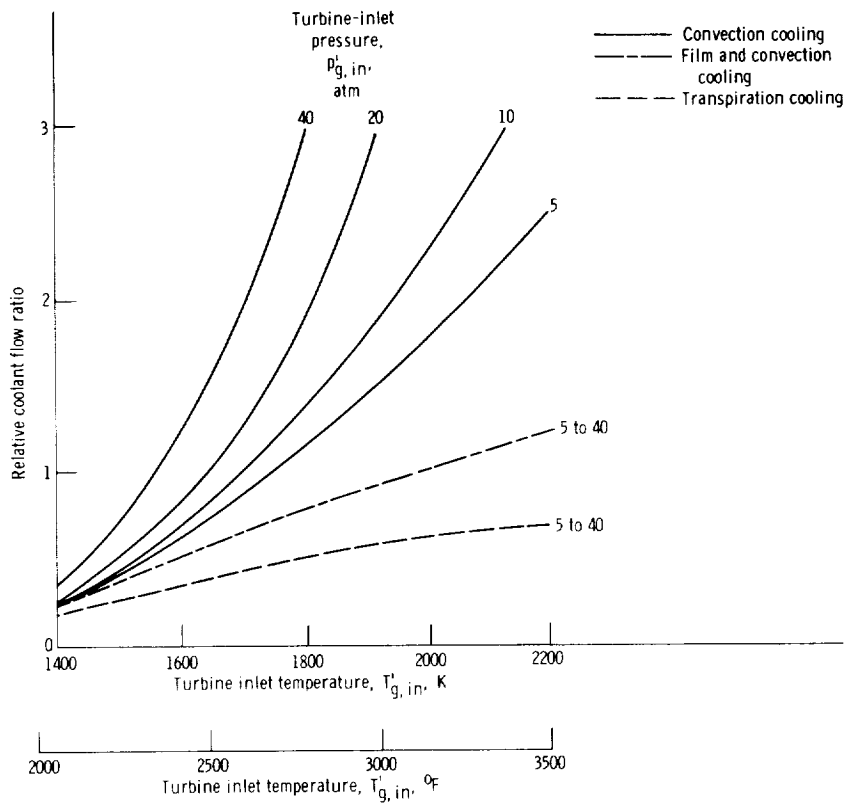


FIGURE 11-3.—Effect of turbine-inlet pressure and temperature on coolant flow requirements.

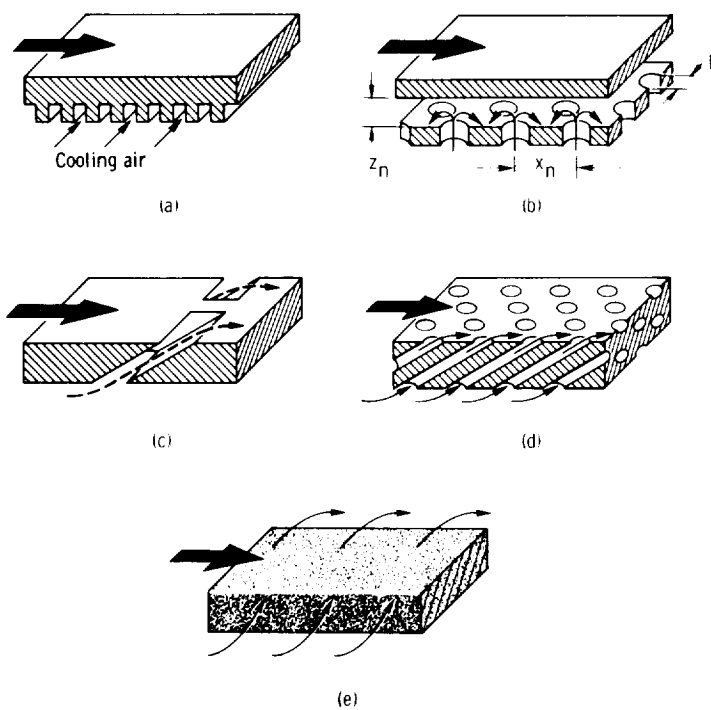
in equation (11-1) becomes the local film temperature, and the heat flux to the blade is then

$$q = h_f(T'_{film} - T_{w,o}) \quad (11-9)$$

where  $T'_{film}$  is the total temperature of the gas film, in K or °R. It is frequently assumed that the heat-transfer coefficient in this equation is the same as in the non-film-cooled case.

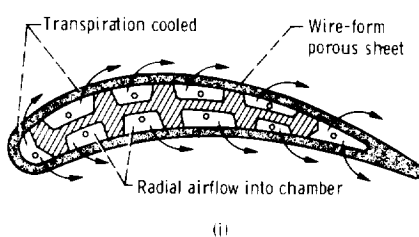
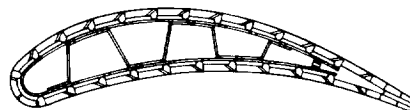
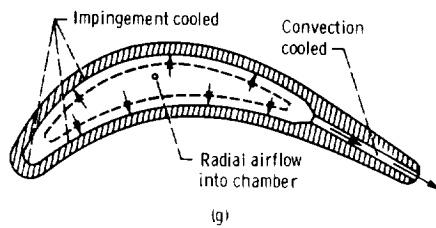
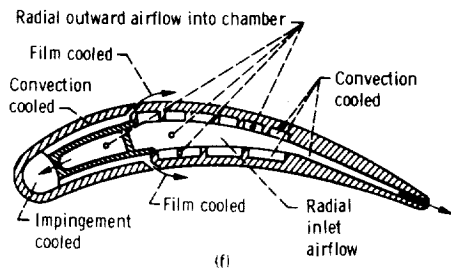
The injection of film air into the boundary layer causes turbine aerodynamic losses which tend to reduce some of the advantages of using higher pressures and temperatures. The aerodynamic and heat-transfer designs must be integrated to achieve an optimum configuration which ensures blade metal temperatures consistent with long-life objectives yet minimizes the loss in turbine efficiency.

Transpiration cooling of a porous blade wall is the most efficient air-cooling scheme available, but it has significant drawbacks which currently limit its use to advanced designs operating under extreme heat-flux conditions. For efficient transpiration cooling, the pores should be small, which leads to problems of blockage due to oxidation and foreign contaminates. Also, the aerodynamic losses can be severe because of normal injection of cooling air into the boundary layer. To offset this latter point, however, it must be recognized that transpiration cooling requires less cooling air than other cooling schemes. A typical transpiration-cooled blade is shown in figure 11-4(i). Full-coverage film cooling from an array of discrete holes, as illustrated in figure 11-4(h), is an attempt to draw on some of the advantages of transpiration cooling without paying the penalties mentioned.



(a) Convection cooling. (b) Impingement cooling.  
 (c) Film cooling. (d) Full-coverage film cooling.  
 (e) Transpiration cooling.

FIGURE 11-4.—Methods for turbine blade cooling.



(f) Convection-, impingement-, and film-cooled blade configuration.

(g) Convection- and impingement-cooled blade configuration.

(h) Full-coverage film-cooled blade configuration.

(i) Transpiration-cooled blade configuration.

FIGURE 11-4.—Concluded.

## HEAT TRANSFER FROM HOT GAS TO BLADE

### Boundary-Layer Equations

*General equations.*—The transfer of heat to the blade is confined to the boundary-layer region very near the surface, where large velocity

and temperature gradients are present. Consequently, to describe the heat-transfer process, the following boundary-layer equations, introduced in chapter 6 (vol. 2), must be solved:

Conservation of mass

$$\frac{\partial}{\partial x} (\rho u) + \frac{\partial}{\partial y} (\rho v + \overline{\rho' v'}) = 0 \quad (11-10)$$

where

$v$	time-average value of velocity component in $y$ direction, m/sec; ft/sec
$(\ )'$	fluctuating component
$\overline{(\ )}$	time-averaged quantity

Conservation of momentum

$$\rho u \frac{\partial u}{\partial x} + (\rho v + \overline{\rho' v'}) \frac{\partial u}{\partial y} = -g \frac{dp}{dx} + g \frac{\partial}{\partial y} \tau + g \rho B_x \quad (11-11)$$

where

$\tau$	local shear stress, N/m <sup>2</sup> ; lb/ft <sup>2</sup>
$B_x$	component of body force in the $x$ direction, N/kg; lbf/lbm

Conservation of energy

$$\rho u \frac{\partial H}{\partial x} + (\rho v + \overline{\rho' v'}) \frac{\partial H}{\partial y} = \frac{\partial}{\partial y} \left( \frac{1}{K} q + \frac{u \tau}{J} \right) + Q \quad (11-12)$$

where

$H$	total enthalpy, J/kg; Btu/lb
$J$	conversion constant, 1; 778 (ft)(lb)/Btu
$Q$	heat-generation term, W/m <sup>3</sup> ; Btu/(sec)(ft <sup>3</sup> )

The dependent variables  $\rho$ ,  $u$ ,  $v$ , and  $H$  are time-average values (i.e.,  $\bar{\rho}$ ,  $\bar{u}$ ,  $\bar{v}$ , and  $\bar{H}$ , as denoted in ch. 6), with the overbar being understood.

The solution of these equations requires appropriate expressions for the shear stress and heat flux through the hydrodynamic and thermal boundary layers. The laminar contribution to molecular diffusivity of heat and momentum is straightforward, but our limited understanding of turbulent flow requires the use of various assumptions in describing the turbulent counterpart. One such assumption, which bears little physical resemblance to the structure of turbulence but has persisted because of its simplicity and success in predicting turbulent transport processes, is Prandtl's mixing-length hypothesis for eddy diffusivity of heat and momentum. The shear stress and heat flux are expressed as the sum of the laminar and turbulent contributions:

$$\tau = \frac{\rho}{g} \left( \nu_L \frac{\partial u}{\partial y} - \overline{u'v'} \right) \quad (11-13)$$

and

$$q = K\rho \left( \alpha_L \frac{\partial \mathcal{H}}{\partial y} - \overline{v'\mathcal{H}'} \right) \quad (11-14)$$

where

$\nu_L$  laminar component of momentum diffusivity (kinematic viscosity),  $\text{m}^2/\text{sec}$ ;  $\text{ft}^2/\text{sec}$

$\alpha_L$  laminar component of heat diffusivity,  $\text{m}^2/\text{sec}$ ;  $\text{ft}^2/\text{sec}$

$\mathcal{H}$  static enthalpy,  $\text{J/kg}$ ;  $\text{Btu/lb}$

The turbulent shear stress  $\overline{u'v'}$  and heat flux  $\overline{v'\mathcal{H}'}$  are assumed proportional to the respective gradients in the mean flow variable; that is,

$$\overline{u'v'} = -\nu_T \frac{\partial u}{\partial y} \quad (11-15)$$

and

$$\overline{v'\mathcal{H}'} = -\alpha_T \frac{\partial \mathcal{H}}{\partial y} \quad (11-16)$$

where the subscript  $T$  denotes the turbulent component of momentum and heat diffusivity.

Equations (11-13) and (11-14) can then be written as

$$\tau = \frac{\rho}{g} (\nu_L + \nu_T) \frac{\partial u}{\partial y} = \frac{\rho}{g} \nu \frac{\partial u}{\partial y} \quad (11-17)$$

and

$$q = K\rho (\alpha_L + \alpha_T) \frac{\partial \mathcal{H}}{\partial y} = K\rho \alpha \frac{\partial \mathcal{H}}{\partial y} \quad (11-18)$$

The preceding boundary-layer equations assume temperature-variable properties and compressible, turbulent flows (inclusive of laminar flow where both  $\nu_T$  and  $\alpha_T$  approach zero). If the variation in specific heat  $c_p$  is neglected and there is no internal heat generation, the energy equation reduces to equation (6-42).

If temperature-variable properties are assumed at the onset of the analysis, all boundary-layer equations must be solved simultaneously. However, constant properties are frequently assumed, and experimental data are usually taken under approximately isothermal conditions. The final results are then corrected to account for temperature-variable properties. These corrections will be considered in a later section.

*Integral equations.*—As we saw in chapter 6 (vol. 2) with the momentum equation, it is often convenient to solve the boundary-layer equations from an integral approach in terms of integral parameters

such as momentum and displacement thicknesses rather than in terms of discrete velocity profiles. Just as the displacement and momentum thicknesses derive their meaning from the integral momentum equation, so the enthalpy thickness is a significant boundary-layer parameter for the integral energy equation. The enthalpy thickness  $\Delta$  is defined as follows:

$$\Delta = \frac{\int_0^\infty \rho u (H - H_\infty) dy}{\rho_\infty u_\infty (H_{w,\infty} - H_\infty)} \quad (11-19)$$

Note that the subscript  $g$  refers to the free-stream value denoted by the subscript  $e$  in chapter 6. For low-velocity, constant-property flow,

$$\Delta = \frac{\int_0^\infty u (T' - T'_{\infty}) dy}{u_\infty (T_{w,\infty} - T'_{\infty})} \quad (11-20)$$

The enthalpy thickness is a measure of the convected energy decrement caused by the boundary layer.

The integral energy equation can be derived either by integrating equation (11-3) or directly by balancing the transport of energy across the boundary of a control volume containing the hydrodynamic and thermal boundary layers (for details see ref. 2). In either case, the resulting integral energy equation for compressible flow with temperature-variable properties and mass transfer at the wall is

$$\begin{aligned} & \frac{q}{K \rho_\infty u_\infty (H_{w,\infty} - H_\infty)} + \frac{\rho_c u_c}{\rho_\infty u_\infty} \\ &= \frac{d\Delta}{dx} + \Delta \left[ (1 - M_\infty^2) \frac{1}{u_\infty} \frac{du_\infty}{dx} + \frac{1}{(H_{w,\infty} - H_\infty)} \frac{d}{dx} (H_{w,\infty} - H_\infty) \right] \end{aligned} \quad (11-21)$$

Note that if we make restrictive assumptions of constant properties, zero pressure gradient, low-speed flow (incompressible), no mass flux at the wall, and constant temperature difference  $(T_{w,\infty} - T'_{\infty})$  with  $x$ , then equation (11-21) reduces to its simplest form,

$$\frac{q}{K \rho u_\infty c_p (T_{w,\infty} - T'_{\infty})} = \frac{d\Delta}{dx} \quad (11-22)$$

If a local heat-transfer coefficient  $h_{\infty,x}$  is defined as

$$h_{\infty,x} = \frac{q}{(T_{w,\infty} - T'_{\infty})} \quad (11-23)$$

then,

$$\frac{h_{\infty,x}}{K \rho u_\infty c_p} = \frac{d\Delta}{dx} = St_x \quad (11-24)$$

The group of variables on the left side is dimensionless and is called the local Stanton number  $St_x$ , which is also equal to

$$St_x = \frac{Nu_x}{Re_x Pr} \quad (11-25)$$

Notice from equations (6-72) and (6-75) that with similar assumptions, the integral momentum equation resulted in

$$\frac{C_{f,x}}{2} = \frac{d\theta}{dx} \quad (11-26)$$

For compressible flow, there is dissipation of kinetic energy into thermal energy by viscous shear within the boundary layer. This is characterized by an increase in the static temperature near the wall as shown in figure 11-5. The effective gas temperature  $T_{g,e}$ , or adiabatic wall temperature  $T_{w,a}$ , is the temperature the wall would reach if it were uncooled and is, therefore, a measure of the viscous heating in the boundary layer. This dissipation of kinetic energy is related to the recovery factor  $r$  defined by the following equation:

$$T_{g,e} = T_{w,a} + r \frac{u_g^2}{2gJc_p} \quad (11-27)$$

where  $t_g$  is the hot-gas static temperature, in K or °R. For laminar flow, the recovery factor can be approximated by  $Pr^{1/2}$ , while for a turbulent boundary layer,  $r$  is assumed to equal  $Pr^{1/3}$ . It is not surprising that the Prandtl number has an effect on the adiabatic wall temperature. The Prandtl number is the ratio of the viscosity (responsible for energy dissipation) to the thermal diffusivity (mechanism allowing heat to escape from the boundary layer). This would suggest that for a given free-stream kinetic energy, a high Prandtl number should lead to a high adiabatic wall temperature, and vice versa.

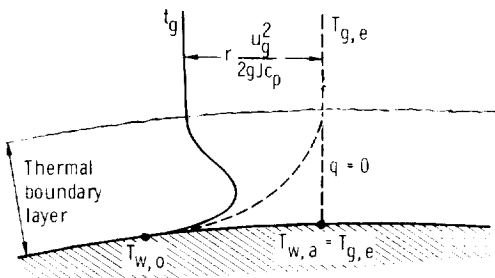


FIGURE 11-5.—Temperature distribution in a high-velocity boundary layer.

The heat flux to the blade is proportional to the temperature gradient (either effective or static gas temperature) at the wall:

$$q = -k_g \frac{\partial t}{\partial y} \Big|_{y=0} = -k_g \frac{\partial T_{g,e}}{\partial y} \Big|_{y=0} = h_{g,z}(T_{g,e} - T_{w,o}) \quad (11-28)$$

As we have already seen, it is convenient to express the heat flux in terms of the heat-transfer coefficient  $h_{g,z}$  and the gas-to-wall temperature difference. The gas temperature in this case must always be the effective gas temperature, or the adiabatic wall temperature.

The problem in determining the heat flux to the blade is to find a suitable expression for the heat-transfer coefficient  $h_{g,z}$ . The objective is to design a cooling configuration which will yield a constant outer-wall temperature. In reality, however, the surface temperature is never constant. The effect that the actual varying surface temperature has on the thermal boundary layer can be accounted for in more refined design stages.

### Solutions to Boundary-Layer Equations

*First-order approximation.*—The simplest approach to the solution is to assume that the heat-transfer coefficient on the suction or pressure side of the blade is approximated by a flat-plate correlation faired into a heat-transfer coefficient distribution around a cylinder in a crossflow for the blade leading-edge region. Though the flat-plate expression pertains, in a strict sense, only to zero-pressure-gradient flow, the results are accurate enough for a first-order approximation. In fact, often the flat-plate correlation yields results surprisingly close to those of more sophisticated analyses, primarily because the Stanton number  $St$  is relatively insensitive to pressure gradient.

For laminar flow over a flat plate with the thermal and the hydrodynamic boundary layers both beginning at the leading edge, the energy equation can be solved directly by means of the Blasius similarity solution discussed in chapter 6 for the velocity profile. With the wall temperature assumed to be constant, the result is

$$h_{g,z} = 0.332 \frac{k_g}{x} Re_x^{1/2} Pr^{1/3} \quad (11-29)$$

The turbulent counterpart is given by

$$h_{g,z} = 0.0296 \frac{k_g}{x} Re_x^{0.8} Pr^{1/3} \quad (11-30)$$

The local velocity  $u_{g,z}$  is used in the Reynolds number.

For the heat-transfer coefficient  $h_{g,e}$  in the leading-edge region, the following correlation is frequently assumed:

$$h_{g, le} = a \left[ 1.14 \frac{k_g}{D} \left( \frac{\rho_g u_{g,\infty} D}{\mu} \right)^{1/2} Pr^{0.4} \left( 1 - \left| \frac{\Phi}{90} \right|^3 \right) \right] \quad -80^\circ < \Phi < 80^\circ \quad (11-31)$$

where

- $a$  augmentation factor
- $D$  diameter of leading-edge circle, m; ft
- $u_{g,\infty}$  velocity of gas approaching leading edge, m/sec; ft/sec
- $\Phi$  angular distance from leading-edge stagnation point, deg

The bracketed term is the heat-transfer coefficient for a cylinder of diameter  $D$  (see fig. 11-6) in a cross-flowing, laminar free stream.

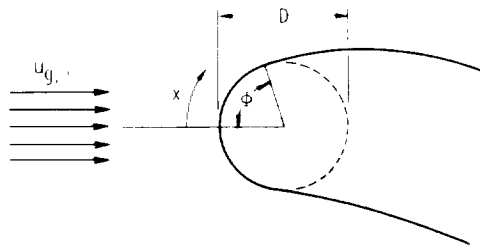


FIGURE 11-6.—Blade leading-edge geometry.

The term  $a$  is an augmentation factor used to adjust the coefficient to account for the highly turbulent mainstream flow approaching a vane or blade leading edge. Various magnitudes of the factor  $a$ , from 1.2 to 1.8, have been used. This amplification of heat flux is uniquely associated with large, favorable-pressure-gradient flows. The highly accelerated flow at the stagnation region stretches vortex filaments oriented with their axes in the direction of flow, thereby increasing the turbulent fluctuating velocities within the boundary layer. Kestin (ref. 3) has studied this phenomenon in detail, but as yet, no general correlation of stagnation heat transfer with turbulence scale and intensity is available.

Transition from laminar to turbulent flow will occur when the Reynolds number becomes sufficiently high to allow instabilities in the boundary layer to grow. For a flat plate with zero pressure gradient, it can generally be assumed that transition will take place in the Reynolds number range of 200 000 to 500 000, depending on free-stream turbulence and surface roughness. However, a Reynolds num-

ber based on the distance,  $x$ , from the leading edge (boundary-layer origin) is not a practical transition criterion, because it is not a local parameter. It is more convenient to use the momentum thickness,  $\theta$ , as the characteristic length in the Reynolds number for determining transition, because the critical Reynolds number at a given point is then independent of the history of the boundary layer; that is, it is immaterial how the boundary layer developed in getting to the given state. For a strongly accelerated flow, the boundary layer never becomes turbulent. This fact is consistent with the use of  $\theta$  but not with the use of  $x$ . A value of  $Re_{\theta,crit}=360$  is a "universal" critical Reynolds number corresponding to  $Re_x=300\ 000$  for a flat plate and  $Re_D=2000$  for pipe flow. For flow over a turbine blade with very high free-stream turbulence, a conservative value of  $Re_{\theta,crit}=200$  can be assumed.

An approximate expression for the momentum thickness variation on a turbine blade can be derived from the integral momentum equation from chapter 6 (eq. (6-76)) by making suitable assumptions as to the functional form of the local velocity profile through the boundary layer (see ref. 2). Upon integrating equation (6-76), the laminar momentum thickness as a function of a variable free-stream velocity is given by

$$\theta_L = \frac{0.67\nu^{0.5}}{u_g^3} \left( \int_0^x u_g^5 dx \right)^{0.5} + \theta_{stag} \quad (11-32)$$

where  $x$  is the surface distance measured from the stagnation point, in meters or feet. The momentum thickness  $\theta_{stag}$  at the stagnation point of a cylinder of diameter  $D$  in a crossflow with an approach velocity  $u_{g,\infty}$  is

$$\theta_{stag} = \frac{0.1D}{\sqrt{\frac{u_{g,\infty}^2}{2\nu} D}} \quad (11-33)$$

Turbulent or transitional flow, then, exists when the value of  $\theta$  is such that  $(\rho u_g \theta / \mu) > 200$ . The value of  $x$  where this occurs is denoted as  $x_{crit}$ .

The turbulent momentum thickness is obtained in a similar manner by the equation

$$\theta_T = \left[ \frac{0.016\nu^{0.25}}{u_g^{4.11}} \int_{x_{crit}}^x u_g^{3.86} dx + \theta_{L,crit}^{1.25} \left( \frac{u_{g,crit}}{u_g} \right)^{4.11} \right]^{0.8} \quad (11-34)$$

This assumes an abrupt transition from laminar to turbulent flow.

*Integral method.*—The solution of the integral equations of momentum and energy to obtain the heat flux to a blade is a more refined and accurate approach than the "flat-plate approximation" previously discussed. The penalty for more accuracy is, of course, the increased complexity of the computation. In many cases, the more sophisticated

methods are not warranted in the early stages of design. The integral method accounts for free-stream velocity variation more realistically, and the effect of a nonconstant surface temperature on  $h_{g,x}$  can also be included. However, some assumptions must still be made in order to solve the integral equations.

Consider the integral energy equation (eq. (11-21)) with constant specific heat and no mass transfer across the wall boundary.

$$St_x - \frac{h_{g,x}}{K\rho_g u_g c_p} \frac{d\Delta}{dx} + \Delta \left[ \frac{1}{\rho_g} \frac{d\rho_g}{dx} + \frac{1}{u_g} \frac{du_g}{dx} + \frac{1}{(T_{w,o} - T_g')} \frac{d}{dx} (T_{w,o} - T_g') \right] \quad (11-35)$$

Ordinarily, the integral momentum equation would first have to be solved in order to evaluate the enthalpy thickness  $\Delta$  in equation (11-20). Ambrok (ref. 4), however, proposed an approach whereby equation (11-35) could be solved independently of the momentum equation by making use of the fact that experimental data show the Stanton number to be a very weak function of pressure gradient. He proposed that the Stanton number can be written as a function of a local Reynolds number based on enthalpy thickness as the characteristic length, and that this function is independent of pressure gradient.

$$St_x = f(Re_\Delta) \quad (11-36)$$

If  $f$  is independent of pressure gradient, then the flat-plate solution should give us the functional form.

For turbulent flow over a flat plate, combining equations (11-4) and (11-25) yields

$$St_x = 0.0296 Re_x^{-0.2} Pr^{-2/3} \quad (11-37)$$

Recalling from equation (11-24) that for a flat plate

$$St_x = \frac{d\Delta}{dx} \quad (11-38)$$

the local Stanton number can be expressed in terms of the enthalpy thickness by combining equations (11-37) and (11-38) so as to obtain

$$St_x = (0.0296 Pr^{-2/3})^{1.25} (0.8 Re_\Delta)^{-0.25} \quad (11-39)$$

Hence, the function  $f$  from equation (11-36) is given by equation (11-39) for turbulent flow and, by assumption, for any arbitrary free-stream velocity variation. (The same argument holds for laminar flows.) Substituting equation (11-39) into equation (11-35) and integrating yields

$$St_x - \frac{h_{g,x}}{K\rho_g u_g c_p} = 0.0296 Pr^{-2/3} (T_g' - T_{w,o})^{0.25} I^{-0.2} \quad (11-40)$$

where

$$I = \int_{x_{crit}}^{x'} \frac{\rho_k u_k (T_{k,z} - T_{w,o})^{1.25}}{\mu} dx + \left[ \frac{0.8 Re_2 (T_{k,z} - T_{w,o})}{0.0296 Pr^{2/3}} \right]^{1.25} \quad (11-41)$$

The integration is performed numerically for  $h_{k,z}$ , with the critical enthalpy-thickness Reynolds number being evaluated from the laminar-boundary-layer equation. For further details, see reference 2.

*Finite-difference solution.*—The most accurate method of calculating the heat flux to a turbine blade is to solve all the boundary-layer equations simultaneously by a finite-difference approach. There are several good numerical programs available to do this. One of these was developed by W. M. Kays and uses the numerical procedure of Spalding and Patankar (ref. 5). In addition to the equations for the conservation of mass (eq. (11-10)), momentum (eq. (11-11)), and energy (eq. (11-12)), a fourth conservation equation, that of turbulent kinetic energy  $\mathcal{K}$  is also solved simultaneously with the others. Conservation of turbulent kinetic energy is given by

$$\rho u \frac{\partial \mathcal{K}}{\partial x} + (\rho v + \overline{\rho' v'}) \frac{\partial \mathcal{K}}{\partial y} - \rho \nu_T \left( \frac{\partial u}{\partial y} \right)^2 + \frac{\partial}{\partial y} \left[ \rho (\nu_L + \nu_T) \frac{\partial \mathcal{K}}{\partial y} \right] = \mathcal{D}_T \quad (11-42)$$

where  $\mathcal{D}_T$  is a turbulent dissipation term, in  $\text{W/m}^3$  or  $\text{Btu}/(\text{ft}^3)(\text{sec})$ . The turbulent kinetic energy is defined as

$$\mathcal{K} = \frac{1}{2gJ} (\overline{u'^2} + \overline{v'^2} + \overline{w'^2}) \quad (11-43)$$

where  $w'$  is the fluctuating component of velocity, in  $\text{m/sec}$  or  $\text{ft/sec}$ , in the direction perpendicular to the  $x-y$  plane. By including the turbulent-kinetic-energy equation, the mixing length is calculated locally in the boundary layer. Also, the effects of free-stream turbulence can be accounted for.

All properties are evaluated locally through the boundary layer with no restrictive or approximating assumptions made on the variation of surface temperature or velocity profile. Mass transfer at the wall (transpiration cooling) and local film cooling are also handled in a straightforward manner.

Figure 11-7 presents example results from computer plots showing the flexibility of the numerical approach for the case of a high-temperature, high-pressure turbine vane. The free-stream velocity profile is given in figure 11-7(a). The initial profiles through the boundary layer must be supplied as a boundary condition to get the integration started (fig. 11-7(b)), but from then on, profiles can be

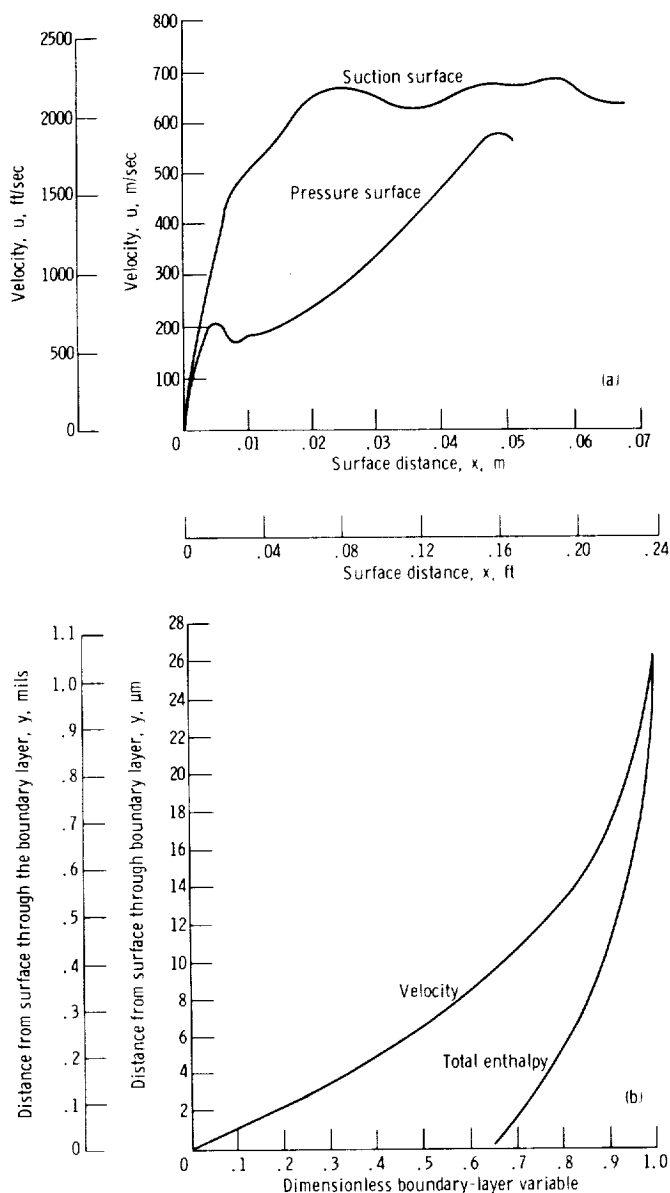
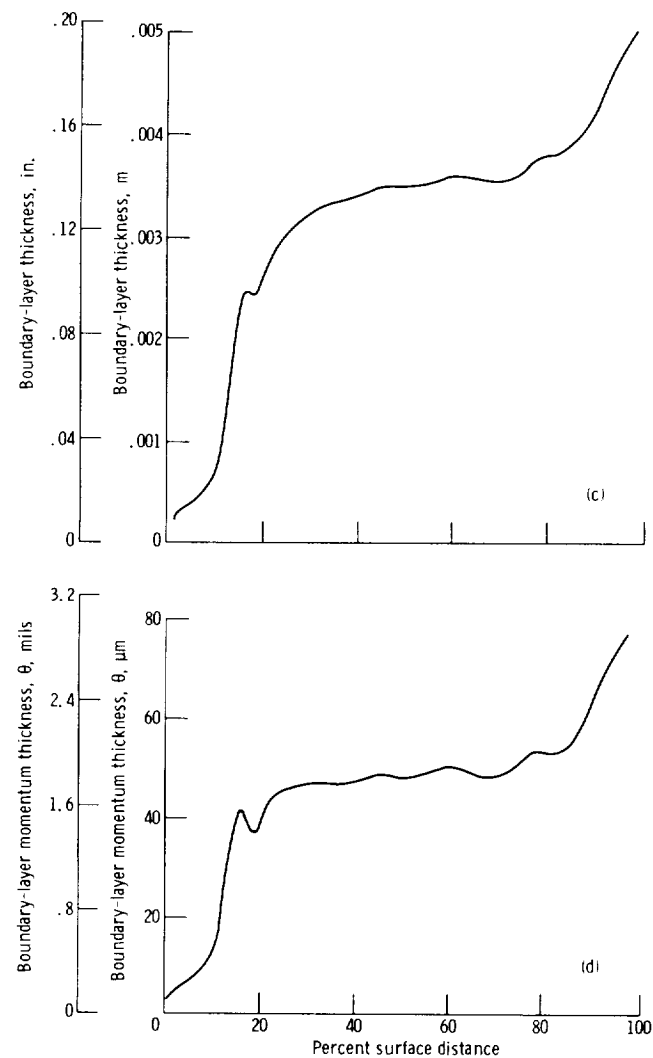


FIGURE 11-7.—Boundary-layer development over a high-temperature, high-pressure turbine vane.

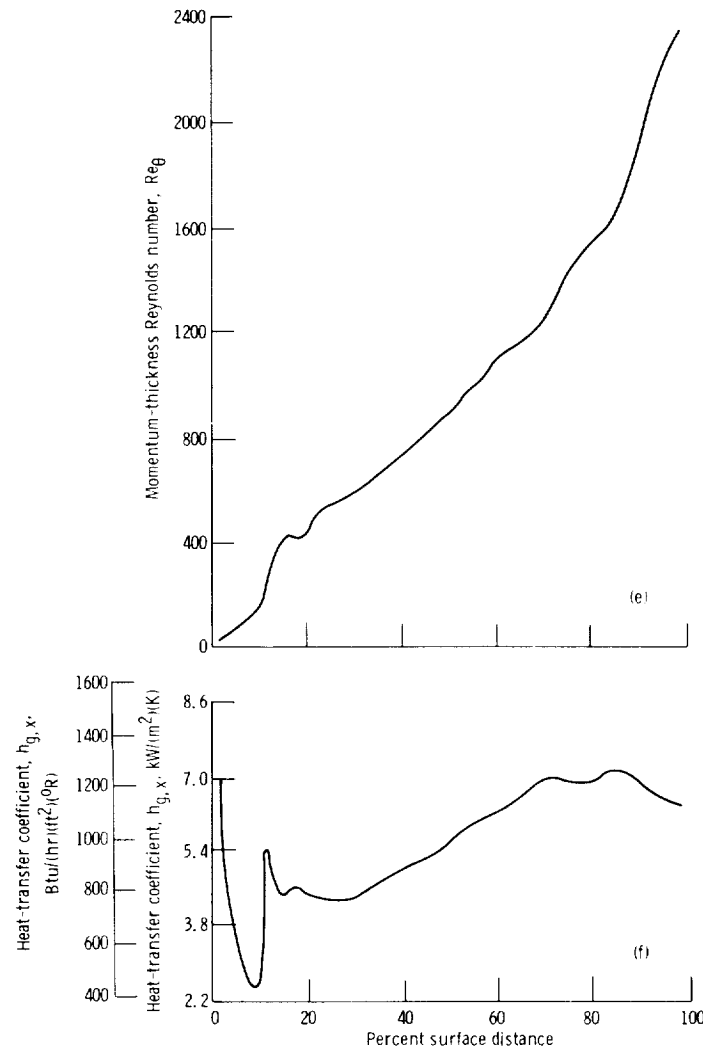
calculated through the boundary layer at discrete  $x$  locations. The boundary-layer thickness, momentum thickness, momentum-thickness Reynolds number, and heat-transfer coefficient are shown in figures 11-7(c) to 11-7(f), respectively. Notice that just upstream of the



(c) Pressure-side boundary-layer thickness.  
 (d) Pressure-side boundary-layer momentum thickness.

FIGURE 11-7.—Continued.

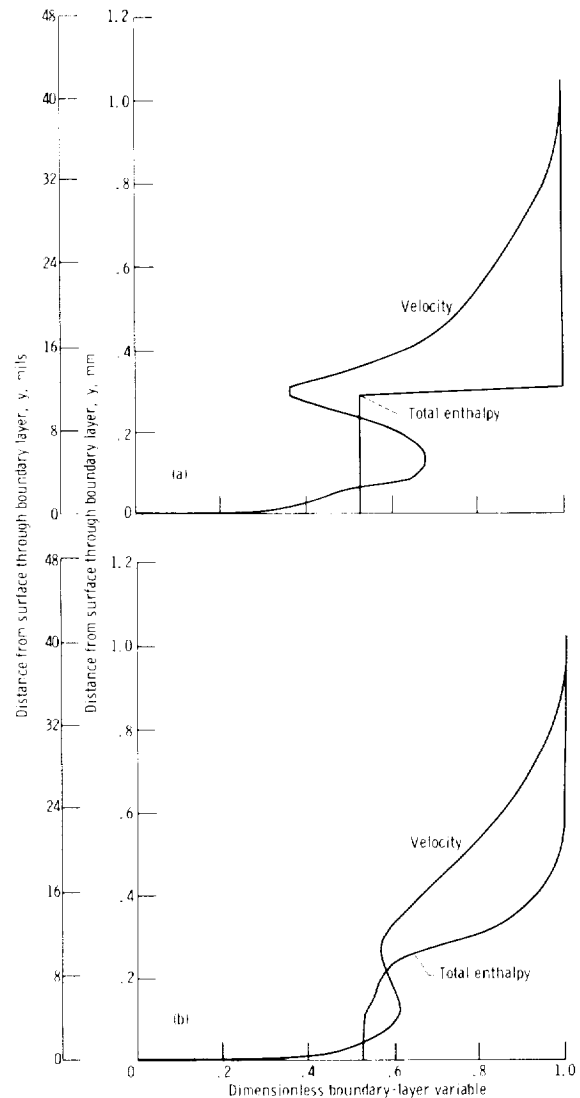
20-percent surface distance location on the vane, the boundary-layer thickness (fig. 11-7(c)) and the momentum thickness (fig. 11-7(d)) increase rapidly and then decrease slightly over a short distance before continuing to increase. This "blip" is caused by the rapid



(e) Pressure-side momentum-thickness Reynolds number.

(f) Pressure-side heat-transfer coefficient.

FIGURE 11-7.—Concluded.



- Initial profiles at slot. Free-stream reference velocity, 609.6 m/sec or 2000 ft/sec; free-stream reference enthalpy,  $4.8189 \times 10^6$  J/(kg)(K) or 1151.75 Btu/(lb)(°R).
- Three slot-widths downstream of slot. Free-stream reference velocity, 610.8 m/sec or 2004 ft/sec; free-stream reference enthalpy,  $4.8189 \times 10^6$  J/(kg)(K) or 1151.75 Btu/(lb)(°R).

FIGURE 11-8.—Boundary-layer profiles along adiabatic wall with film cooling.

deceleration and acceleration of the mainstream flow resulting from the adverse-pressure-gradient region aft of the leading edge on the pressure side. Transition from a laminar boundary layer occurs at about the 10-percent location. Very little of the boundary layer is in a transitional state, as can be seen from figure 11-7(f).

Initial velocity and enthalpy profiles illustrating an example of film cooling are given in figure 11-8(a). About 3 slot widths downstream, the profiles have changed to the shapes shown in figure 11-8(b).

### Temperature-Dependent Fluid Properties

The relations involving the dimensionless parameters  $Re$ ,  $Pr$ ,  $Nu$ , and  $St$ , discussed in earlier sections, contain gas properties  $\rho$ ,  $k$ ,  $\mu$ , and  $c_p$ , which all vary with temperature. The temperature dependence of these transport properties causes a change in the velocity and temperature profiles (and, therefore, in the heat-transfer coefficient) compared to results obtained if properties were constant. Since large temperature variations occur across the boundary layer, at what temperature are the properties to be evaluated? Usually, constant-property analytical solutions (except in the finite-difference method) or the experimental data obtained with small temperature differences are corrected to account for property variation. Two schemes are in common use for the correction of constant property results; namely, the temperature-ratio method (for gases) and the reference-temperature method.

In the latter method, all transport properties are evaluated at the reference temperature:

$$T_{ref} = 0.5 T_{w,o} + 0.28 t_g + 0.22 T_{g,e} \quad (11-44)$$

The temperature-ratio method assumes

$$\frac{Nu}{Nu_{CP}} = \frac{St}{St_{CP}} = \left( \frac{T_{g,e}}{T_{w,o}} \right)^n \left( \frac{t_g}{T_{g,e}} \right)^m \quad (11-45)$$

The subscript  $CP$  refers to constant properties evaluated at the free-stream static temperature. For laminar flow,  $n=0.08$  and  $m=0.12$ . For turbulent flow,  $n=0.4$  and  $m=0.6$ , a much greater influence than in laminar flow.

### CONDUCTION WITHIN THE BLADE WALL

Once the local heat-transfer coefficients on the hot-gas side and coolant side are known, the heat-flux boundary conditions for the heat-conduction problem are available. The blade or vane is broken up into a number of finite elements, as shown, for example, in figure

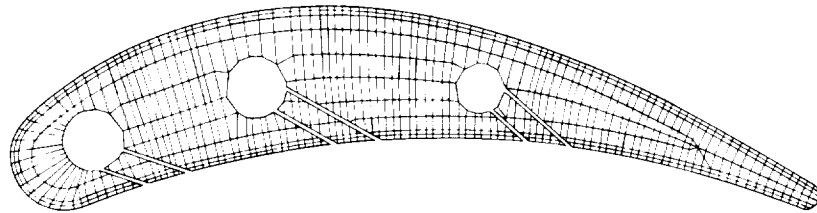


FIGURE 11-9.—Typical node breakdown for a turbine-blade conduction analysis.

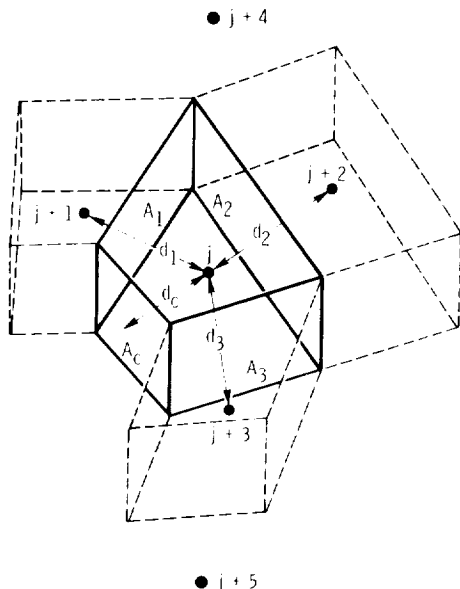


FIGURE 11-10.—Typical boundary element for heat-conduction analysis.

11-9, and an energy balance is written for each element. The result is a system of algebraic finite-difference equations, with the number of equations equal to the total number of elements. All equations must then be solved simultaneously by means of a high-speed, digital computer. Once such a conduction analysis is completed, a detailed temperature distribution throughout the blade is available for use in thermal-stress calculations.

Consider a typical boundary element from figure 11-10. Accounting

for all the energy transfer between the given element (the  $j^{th}$  element) and those adjacent to it (elements  $j+1$  to  $j+5$ ), including the fluid boundary, leads to the following algebraic equation (see fig. 11-10).

$$\frac{\frac{A_c}{d_c + \frac{1}{h_c}} (T_j - T_{c'})^m + \frac{k_w A_1}{d_1} (T_j - T_{j+1})^m + \frac{k_w A_2}{d_2} (T_j - T_{j+2})^m + \dots + \frac{k_w A_5}{d_5} (T_j - T_{j+5})^m}{\rho c_p V_j} = \frac{\rho c_p V_j}{\Delta(\text{time})} (T_j^{n+1} - T_j^n) \quad (11-46)$$

where

- $A_i$  surface area between  $j^{th}$  element and element or boundary denoted by subscript  $i$ ,  $\text{m}^2$ ;  $\text{ft}^2$
- $d_i$  distance between  $j^{th}$  element and element or boundary denoted by subscript  $i$ ,  $\text{m}$ ;  $\text{ft}$
- $V_j$  volume of  $j^{th}$  element,  $\text{m}^3$ ;  $\text{ft}^3$

The superscript  $m$  denotes time step  $n$  or  $n+1$ , depending on whether an explicit or implicit transient scheme is used.

A similar equation for every volume element must be written. The calculation may be either transient or steady-state, depending on how the equations are structured. If the element is allowed to reduce to an infinitesimal size, the energy balance at a point yields the familiar heat-conduction equation

$$\rho c_p \frac{\partial T}{\partial(\text{time})} = \frac{\partial}{\partial x} \left( k_w \frac{\partial T}{\partial x} \right) + \frac{\partial}{\partial y} \left( k_w \frac{\partial T}{\partial y} \right) + \frac{\partial}{\partial z} \left( k_w \frac{\partial T}{\partial z} \right) \quad (11-47)$$

where  $x$ ,  $y$ , and  $z$  are the coordinate directions.

## COOLANT-SIDE CONVECTION

There can be many internal flow geometries used to promote heat transfer by convection to the coolant, and for that reason, it would be impossible to discuss each convection-cooling scheme. Essentially, the problem is to determine the heat-transfer coefficient,  $h_c$ , and the local coolant temperature,  $T_{c'}$ , in the previously shown equation

$$q = h_c (T_{w,i} - T'_{c'}) \quad (11-2)$$

This is not, however, as simple as it sounds. The coolant flow path can be very complex, and the internal flow and pressure distribution must be known before the heat-transfer coefficient can be determined. An internal flow network is established, and conservation of momentum equations that describe the internal pressure distribution are solved

to determine the flow split between various parts of the blade. Since there is interaction between each of the three heat-transfer steps discussed (convection from hot gas to surface, conduction through the surface, and convection from surface to coolant), an iterative cycle between the three calculations must be made. After the percentage of air available for cooling a given region of the blade has been determined, empirical correlations for the particular convection scheme considered must be used to determine  $h_c$ .

Various methods are used to enhance coolant-side convection heat transfer. Fins can be added to the cooling passages to act as "turbulators" to keep the flow highly mixed and the boundary layers thin. They also help by increasing the convection surface area. One of the most effective convection methods is impingement cooling (fig. 11-4(b)), where small jets of cooling air are directed toward the inside wall of the blade, as seen in figures 11-4(b) and (g). One representative correlation from reference 6 for impingement cooling gives

$$Nu_{D, \text{imp}} = \varphi_1 \varphi_2 Re_D^m Pr^{1/3} \left( \frac{z_n}{D} \right)^{0.091} \quad (11-48)$$

where

$Nu_{D, \text{imp}}$	impingement-cooling Nusselt number based on hole diameter as characteristic dimension
$z_n$	distance between hole and wall, m; ft
$D$	hole diameter, m; ft

The power  $m$  on the Reynolds number and the coefficient  $\varphi_1$  are both functions of the impingement-hole array geometry and the Reynolds number. A least-squares-curve fit of the data in reference 6 gives

$$m = a_1 \left( \frac{x_n}{D} \right)^2 + b_1 \left( \frac{x_n}{D} \right) + c_1 \quad (11-49)$$

and

$$\varphi_1 = \exp \left[ a_2 \left( \frac{x_n}{D} \right)^2 + b_2 \left( \frac{x_n}{D} \right) + c_2 \right] \quad (11-50)$$

where  $x_n$  is the center-to-center distance, in meters or feet, between holes in the direction of flow, and the coefficients  $a$ ,  $b$ , and  $c$  are given in table 11-I as functions of  $Re_D$ . The coefficient  $\varphi_2$  is an attenuation factor to account for crossflow caused by the accumulation of fluid from multiple rows of impingement jets. It can be expressed as

$$\varphi_2 = \frac{1}{1 + a_3 \psi^{b_3}} \quad (11-51)$$

where  $a_3$  and  $b_3$  are given in table 11-I, and  $\psi$  for the  $i^{\text{th}}$  row of

TABLE 11-I.—IMPINGEMENT-COOLING CORRELATION COEFFICIENTS

Coefficient	Reynolds number range, 300 to 3 000	Reynolds number range, 3 000 to 30 000
$a_1$	-0.0015	-0.0025
$b_1$	.0428	.0685
$c_1$	.5165	.5070
$a_2$	0.0126	0.0260
$b_2$	-.5106	-.8259
$c_2$	-.2057	.3985
$a_3$	0.4215	0.4696
$b_3$	.580	.965

impingement holes is defined as

$$\psi = \left( \frac{G_{cf}}{G_h} \right)_i \left( \frac{z_n}{D} \right) \quad (11-52)$$

where

$G_{cf}$  crossflow mass flux,  $\text{kg}/(\text{sec})(\text{m}^2)$ ;  $\text{lb}/(\text{hr})(\text{ft}^2)$   
 $G_h$  impingement-hole mass flux,  $\text{kg}/(\text{sec})(\text{m}^2)$ ;  $\text{lb}/(\text{hr})(\text{ft}^2)$

## FILM AND TRANSPERSION COOLING

As turbine-inlet temperature and pressure increase, it becomes apparent that convection cooling must be augmented by film cooling to reduce blade metal temperatures and conserve cooling air (as shown in fig. 11-3). The importance of combining both film and convection cooling in a given design is shown in figure 11-11. Here, blade surface temperatures are given for convection cooling only, film cooling only, and combined film and convection cooling, all for the same hot-gas and cooling-air conditions and the same percent coolant flow rate. Except in the immediate region of the film injection hole, the combined cooling yields a significantly lower wall temperature than does either film or convection cooling alone. Notice also that the average wall temperature for film cooling only is about the same as for convection cooling, but the wall temperature gradients are much higher because of the rapid decay of the protective film.

First, localized film cooling from rows of holes or slots will be discussed, then transpiration cooling and full-coverage discrete-hole film

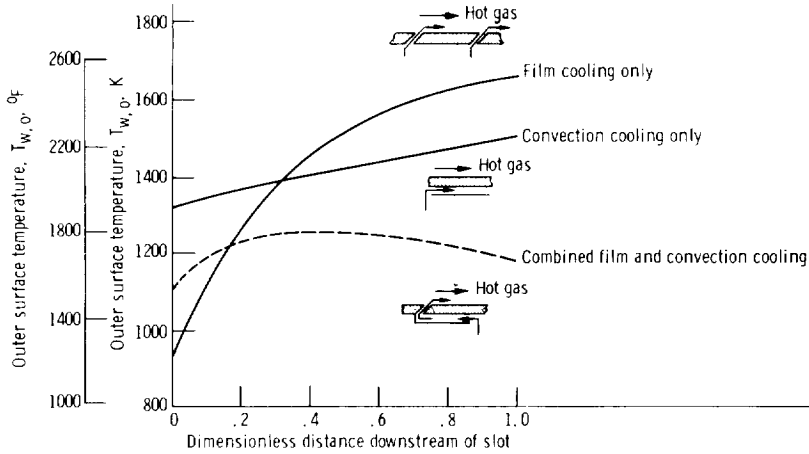


FIGURE 11-11.—Effect of combining film and convection cooling. Constant coolant flow rate.

cooling. To successfully analyze and model film cooling, the “non-film-cooled” heat-transfer coefficient must be known. Hence, the film-cooling analysis builds on the preceding discussion. In the following expression for the heat flux to the surface, the effective gas temperature becomes the film temperature  $T'_{film}$ :

$$q = \epsilon h_{g,z} (T'_{film} - T_{w,o}) \quad (11-53)$$

where  $h_{g,z}$  is the heat-transfer coefficient without film cooling, and

$$\epsilon = \frac{(h_{g,z})_{film}}{h_{g,z}} \quad (11-54)$$

Very near the point of injection, the heat-transfer coefficient is altered somewhat by the injection itself, and  $\epsilon$  is included to account for this. However, the effect is usually damped out rapidly, so  $\epsilon$  is frequently assumed to be unity. The film temperature is sometimes called the adiabatic wall temperature with film cooling, because it is obtained from experimental data under adiabatic wall conditions (i.e., it is the temperature of an uncooled wall having a buffer film layer of cool air between it and the hot gas (see fig. 11-12)). The film temperature is correlated in dimensionless form by the film effectiveness  $\eta_{film}$ :

$$\eta_{film} = \frac{T_{g,e} - T'_{film}}{T_{g,e} - T'_{c,o}} \quad (11-55)$$

where  $T'_{c,o}$  is the injected film temperature (coolant temperature at outer wall). The film effectiveness decays from a value of 1, at the

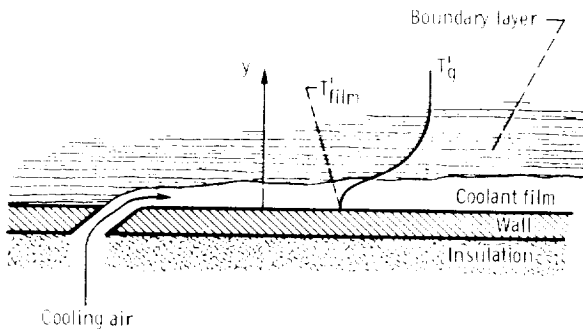


FIGURE 11-12.—Experimental determination of film temperature.

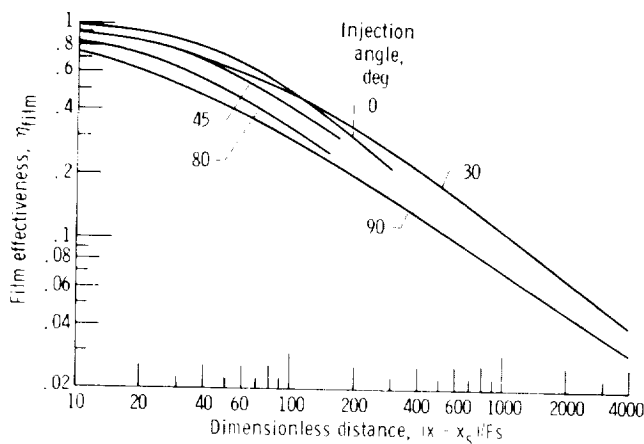


FIGURE 11-13.—Film-cooling effectiveness for slots.

slot, to zero, far downstream. Figure 11-13 gives experimental values of film effectiveness for film injection from slots as determined by a number of investigators. The distance downstream from the slot ( $x - x_s$ ) is normalized by the slot width  $s$  and the mass-flux ratio  $F$  between the film air and the hot-gas stream. The indicated injection angle is with respect to the surface ( $0^\circ$  is parallel to the surface, and  $90^\circ$  is perpendicular). As seen, the film effectiveness decreases with increasing injection angle.

The following expressions (from ref. 7) correlate turbine-blade slot film cooling reasonably well:

$$\eta_{film} = \exp \left\{ -2.9 \left( \frac{\rho_c u_c^2}{\rho_g u_g^2} \right)^{-n} \left( \frac{\rho_g u_g s}{\rho_c u_c s} \right) (Re_x)^{-0.2} \left[ 1 - \left( \frac{x_s}{x} \right)^{0.8} \right] \right\} \quad (11-56)$$

for small values of  $(x - x_s)$ , and

$$\eta_{film} = \frac{C \left( \frac{\rho_c u_c^2}{\rho_g u_g^2} \right)^n \left( \frac{\rho_g u_g s}{\rho_c u_c s} \right) (Re_x)^{0.2}}{1 - \frac{x_s}{x}} \quad (11-57)$$

for large values of  $(x - x_s)$ , where  $x_s$  is the location of the downstream edge of the slot, in meters or feet, measured from the stagnation point. Values for the coefficient  $C$  and the exponent  $n$  are  $C=2.7$  and  $n=0.21$  for a  $30^\circ$  injection angle, and  $C=1.95$  and  $n=0.155$  for a  $15^\circ$  injection angle.

Film effectiveness as a function of the downstream and lateral distances from the injection hole is presented in figure 11-14 (from ref. 8) for film cooling from a single hole and from a row of holes. For small lateral distances, up to about 1 hole diameter in this case, film effectiveness decreases with downstream distance, as previously shown

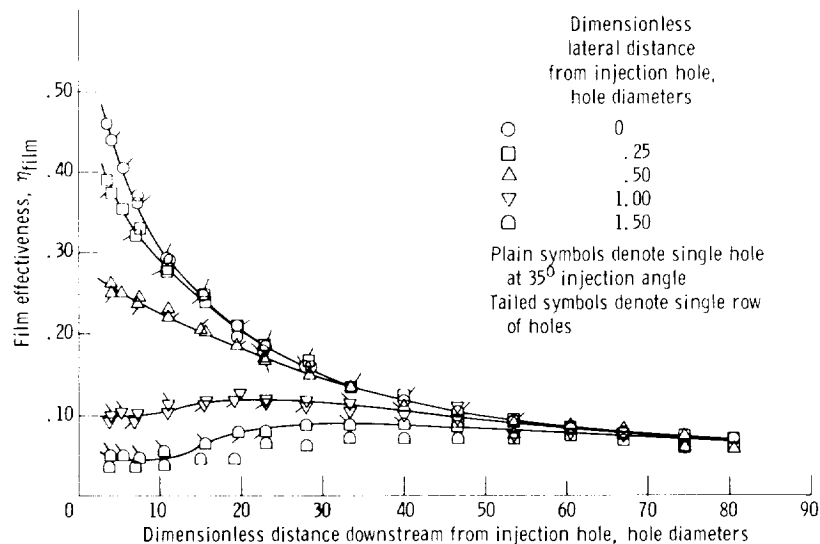


FIGURE 11-14.—Film-cooling effectiveness as function of dimensionless downstream and lateral distances from injection holes. Mass-flux ratio, 0.5; injection-hole diameter, 1.18 cm or 0.464 in.; gas velocity, 30.5 m/sec or 100 ft/sec; Reynolds number,  $0.22 \times 10^6$ .

for slots, and the same values are obtained for single holes as for a row of holes. For larger lateral distances, effectiveness initially increases with downstream distance as a result of the spreading of the injected flow, and the values for the row of holes are larger than for the single hole because of the interaction of flows from adjacent holes. Notice also that  $\eta_{film}$  is not unity at the injection hole. This is due to entrainment of hot gases underneath the film jet as the jet separates from the surface. Very limited data are available for a staggered row of film-cooling holes. Frequently, the slot data are used for this case, with an effective slot width  $s$  defined such that the total area of the holes equals the area of the slot.

Figure 11-15 (from ref. 8) shows the spreading of a film layer from a single hole at various angles of injection. For a 35° injection angle in the direction of the main gas stream, the film spreads less than 2 hole diameters, giving very local film coverage. A compound angle of injection gives more lateral coverage, but the film does not persist as far downstream.

Transpiration cooling of a porous wall is one of the most effective methods of cooling available. With mass transfer from the wall into the boundary layer, it combines film cooling with efficient convection cooling. The porous wall serves as a very effective heat exchanger, where the heat conducted into the wall from the hot gas stream is continuously transferred to the coolant in counter flow as it passes through the small pores. However, there are problems in applying this method of cooling to turbine blades. The pores tend to be extremely small and, therefore, are subject to blockage due to oxidation or contaminants in the air. Also, from an aerodynamic-loss standpoint, a penalty is paid, since the film air is injected into the gas stream essentially normal to the boundary.

In order to alleviate these problems yet still obtain some of the characteristic advantages of transpiration cooling, full-coverage film cooling is used. In full-coverage film cooling, the cooling air issues from a large number of small, closely-spaced, discrete holes in the surface. This type of cooling lies in the spectrum between pure transpiration cooling on the one end, with essentially a continuous mass flux over the surface, and localized film cooling on the other end. The amount of heat transferred by convection to the cooling air flowing through the wall depends on the tortuosity of the internal flow passages. The wall may be constructed of simple, straight-through holes, with a low resultant convection effectiveness, or it may consist of a maze of interconnected flow passages, with a relatively high convection effectiveness.

Convection effectiveness  $\eta_{conv}$  is a term borrowed from heat-exchanger theory and is a measure of the ability of the wall (or blade

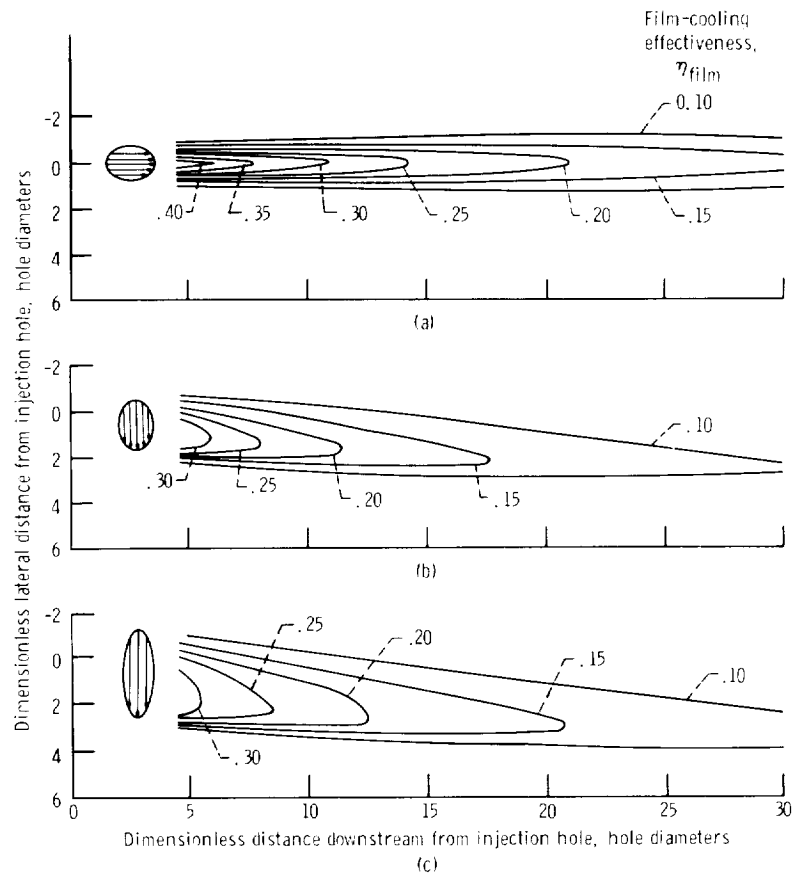
(a) Injection angle,  $35^\circ$ ; lateral injection,  $90^\circ$ .(b) Injection angle,  $90^\circ$ ; lateral injection,  $35^\circ$ .(c) Injection angle,  $90^\circ$ ; lateral injection,  $15^\circ$ .

FIGURE 11-15.—Lines of constant film-cooling effectiveness for single-hole injection. Mass-flux ratio, 0.5.

acting as a heat exchanger) to transfer heat to the cooling air by convection.

$$\eta_{conv} = \frac{T'_{c,o} - T'_{c,in}}{T_{w,o} - T'_{c,in}} \quad (11-58)$$

Since an optimum design utilizes as much of the heat sink available in the cooling air as possible for convection cooling,  $\eta_{conv}$  values approaching the limit of 1 are desirable. However, the convection

effectiveness is usually limited by the cooling-air supply pressure available. As  $\eta_{conv}$  increases, so does the pressure drop through the wall.

Consider a one-dimensional model of the porous or perforated turbine blade wall in figure 11-16. An energy balance can be written on the solid metal matrix and on the cooling-air flow through the wall (see ref. 9). The resulting differential equations for local metal temperature through the wall,  $T_w$ , and local coolant temperature in the wall,  $T'_c$ , are

$$\frac{d^3 T_w}{dy^3} + \frac{h_v}{G_c c_p} \frac{d^2 T_w}{dy^2} - \frac{h_v}{k_{w,e}} \frac{dT_w}{dy} = 0 \quad (11-59)$$

and

$$T'_c = T_w - \frac{k_{w,e}}{h_v} \frac{dT_w}{dy} \quad (11-60)$$

where

$k_{w,e}$  effective thermal conductivity of the porous wall, W/(m)(K); Btu/(hr)(ft)(°R)

$h_v$  internal volumetric heat-transfer coefficient, W/(m³)(K); Btu/(hr)(ft³)(°R)

The boundary conditions are

$$h_c(T_{c,i} - T'_{c,in}) = k_{w,e} \frac{dT_w}{dy} \Big|_{y=0} \quad (11-61)$$

and

$$G_c c_p (T'_{c,i} - T'_{c,in}) = k_{w,e} \frac{dT_w}{dy} \Big|_{y=0} \quad (11-62)$$

In this case, as seen from figure 11-16,  $G_c$  is the mass flux per unit of surface area.

An overall energy balance gives, as a third boundary condition for the heat flux to the wall,

$$q = G_c c_p (T'_{c,o} - T'_{c,in}) = G_c c_p \eta_{conv} (T_{w,o} - T'_{c,in}) \quad (11-63)$$

Typical wall and coolant temperature profiles are shown in figure 11-16. They are both nonlinear with opposite signs in the second derivative, which is a consequence of the interaction of the coolant and matrix heat transfer.

The heat flux to the wall can also be written in terms of a hot-gas-side heat-transfer coefficient:

$$q = h_{t,x} (T_{g,e} - T_{w,o}) \quad (11-64)$$

This is somewhat different from the heat flux expression with local

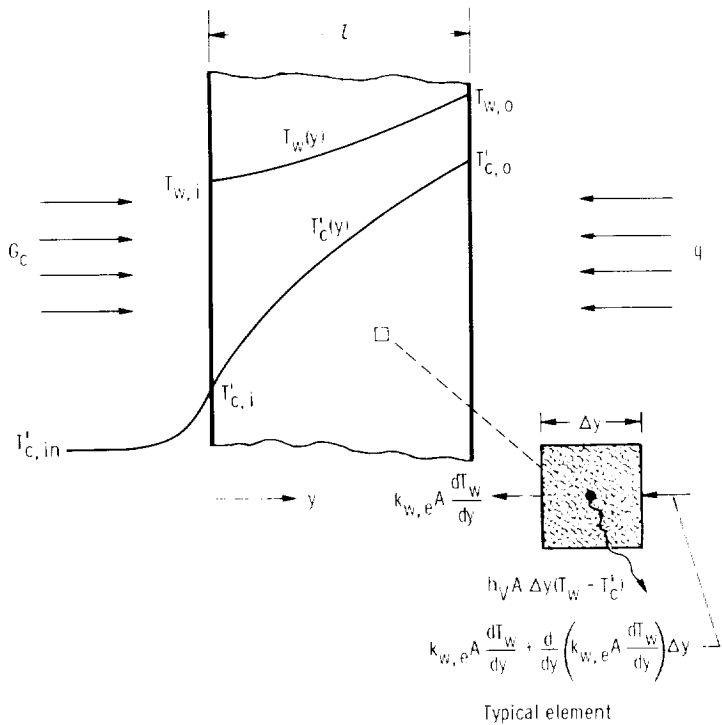


FIGURE 11-16.—Porous-wall temperature profile model.

film cooling in that the actual recovery gas temperature and a "reduced" heat-transfer coefficient  $h_{t,z}$  due to blowing are used rather than the film temperature and the solid-blade heat-transfer coefficient  $h_{g,z}$ .

Consistent with the local one-dimensional model of the blade wall, which incidentally gives good results if the pressure gradient is not too large, we can write

$$\frac{h_{t,z}}{h_{g,z}} = \frac{St_{t,z}}{St_{g,z}} = \frac{\overline{St}_{g,z}}{e^{F/\overline{St}_{g,z}} - 1} f \quad (11-65)$$

where the correction factor  $f$  is a function of convection effectiveness as shown in figure 11-17 (from ref. 10), and  $F$  is the ratio of the coolant mass flux (surface averaged) to the hot-gas mass flux:

$$F = \frac{(\rho u)_c}{(\rho u)_g} \quad (11-66)$$

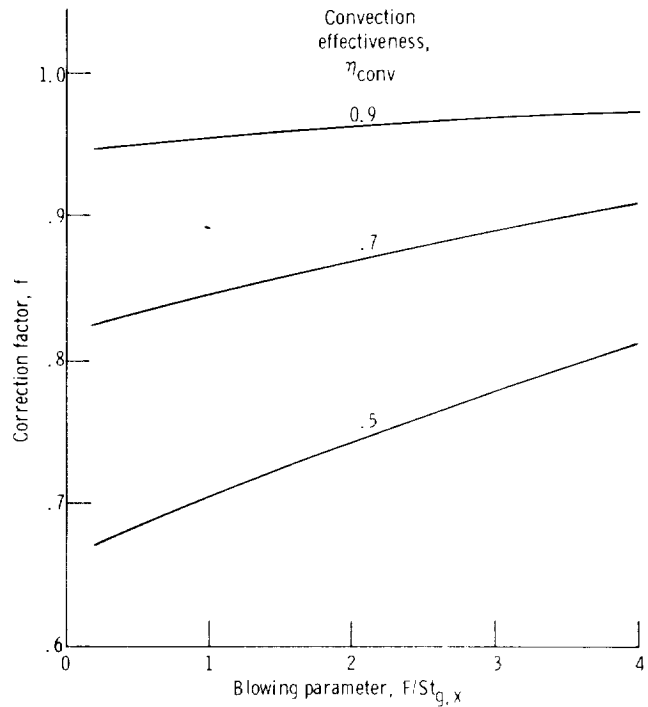


FIGURE 11-17.—Correction to equation (11-65) for wall convection effectiveness.

## SIMILARITY

It is often of economic necessity to evaluate the heat-transfer performance of turbine components at conditions other than the actual engine environment. Generally, initial tests are conducted to evaluate heat-transfer and aerodynamic performance with actual-size prototype hardware at lower gas temperatures and pressures than the actual application. This practice raises a valid question as to whether a cooled blade configuration meeting design specifications at the test conditions will behave similarly under actual engine conditions. To answer this question, the various similarity parameters which are important in relating test performance to engine performance of an actual-size film-convection-cooled turbine blade are discussed.

The Mach number distribution and momentum-thickness Reynolds number distribution around the vane must be the same between engine and test conditions. Similarity in these two parameters is

essential to ensure the same relative distributions of heat-transfer coefficient and adiabatic wall temperature and the same point of transition from laminar to turbulent boundary layer.

Let superscript  $(t)$  refer to test conditions and superscript  $(e)$  refer to engine conditions. To ensure that the local Mach number distribution does not change between the two conditions, the equivalent mass flow must be the same in both cases. Therefore,

$$\frac{w_g^{(t)}}{w_g^{(e)}} = \frac{p_g'^{(t)}}{p_g'^{(e)}} \sqrt{\frac{(RT')_g^{(e)}}{(RT')_g^{(t)}}} \frac{\Gamma_g^{(t)}}{\Gamma_g^{(e)}} \quad (11-67)$$

where  $\Gamma$  is an approximate correction (from eqs. (2-128) and (2-129)) for the variation of specific heat with temperature given by

$$\Gamma = \sqrt{\gamma} \left( \frac{2}{\gamma+1} \right)^{(\gamma+1)/2(\gamma-1)} \quad (11-68)$$

Since the local momentum-thickness Reynolds number must also remain unchanged between  $(t)$  and  $(e)$  conditions,

$$\frac{\left( \frac{\rho u \theta}{\mu} \right)_g^{(t)}}{\left( \frac{\rho u \theta}{\mu} \right)_g^{(e)}} = \frac{\theta_g^{(t)} \mu_g^{(e)} w_g^{(t)}}{\theta_g^{(e)} \mu_g^{(t)} w_g^{(e)}} = \frac{\theta_g^{(t)} \mu_g^{(e)} p_g'^{(t)}}{\theta_g^{(e)} \mu_g^{(t)} p_g'^{(e)}} \sqrt{\frac{(RT')_g^{(e)}}{(RT')_g^{(t)}}} \frac{\Gamma_g^{(t)}}{\Gamma_g^{(e)}} = 1 \quad (11-69)$$

If the local film effectiveness is to remain unchanged between engine and test conditions, the coolant to hot-gas mass-flux ratio  $(\rho u)_c / (\rho u)_g$ , the coolant to hot-gas momentum ratio  $(\rho u^2)_c / (\rho u^2)_g$  (or density ratio  $\rho_c / \rho_g$ ), and the momentum-thickness to film-ejection-hole-diameter ratio  $\theta_g / D$  must be the same in both cases. Since actual-size hardware is presumed, then

$$\frac{\left( \frac{\theta_g}{D} \right)_g^{(t)}}{\left( \frac{\theta_g}{D} \right)_g^{(e)}} = \frac{\theta_g^{(t)}}{\theta_g^{(e)}} = 1 \quad (11-70)$$

and equation (11-69) becomes

$$\frac{\mu_g^{(e)} w_g^{(t)}}{\mu_g^{(t)} w_g^{(e)}} = \frac{\mu_g^{(e)} p_g'^{(t)}}{\mu_g^{(t)} p_g'^{(e)}} \sqrt{\frac{(RT')_g^{(e)}}{(RT')_g^{(t)}}} \frac{\Gamma_g^{(t)}}{\Gamma_g^{(e)}} = 1 \quad (11-71)$$

Equation (11-71) shows that the gas flow rate must vary directly with the viscosity and gives the functional relation between gas pressure and temperature which will provide the same Reynolds number and Mach number distributions for test and engine conditions. Parametric curves of equation (11-71) are shown in figure 11-18 for air.

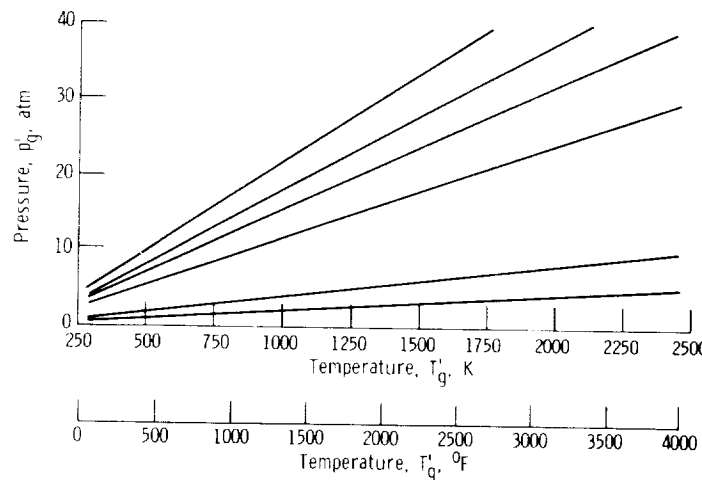


FIGURE 11-18.—Similarity curves of constant Mach number and momentum-thickness Reynolds number distributions around a turbine vane for air properties.

The cooling-air flow rate and temperature are then set by the coolant-to-gas mass-flux ratio and momentum ratio. Requiring

$$\left[ \frac{(\rho u)_c}{(\rho u)_g} \right]^{(t)} = \left[ \frac{(\rho u)_c}{(\rho u)_g} \right]^{(e)} \quad (11-72)$$

implies

$$\left( \frac{w_c}{w_g} \right)^{(t)} = \left( \frac{w_c}{w_g} \right)^{(e)} \quad (11-73)$$

and it is necessary that

$$\left( \frac{t_{c,o}}{t_g} \right)^{(t)} = \left( \frac{t_{c,o}}{t_g} \right)^{(e)} \quad (11-74)$$

to ensure equality of test and engine momentum ratios, since  $p_{c,o} = p_g$ .

Neglecting conduction in the plane of the wall compared to that in the direction normal to the wall, the film ejection temperature  $T_{c,o}$  is related to the supply coolant temperature by

$$\frac{(H_{c,o} - H_{c,in})^{(t)}}{(H_{c,o} - H_{c,in})^{(e)}} = \frac{q^{(t)}}{q^{(e)}} \frac{\mu_g^{(e)}}{\mu_g^{(t)}} \quad (11-75)$$

where the viscosity ratio here represents the mass flow ratio (see eq. (11-71)). Satisfying equations (11-71) to (11-75) ensures that the hot-gas-side heat-transfer coefficient distribution around the vane will

have the same shape for both test and engine conditions. The heat-transfer coefficient in dimensionless Stanton number form is

$$St_g^{(t)} = St_g^{(e)} \left( \frac{Pr^{(e)}}{Pr^{(t)}} \right)_g^{2/3} \quad (11-76)$$

Since the Prandtl number cannot be set independently if all other similarity conditions discussed are met, the departure of the Stanton number ratio from unity depends on the Prandtl number ratio in equation (11-76).

On the coolant side, the heat-transfer coefficient in dimensionless Nusselt number form is given by

$$Nu_c^{(t)} = Nu_c^{(e)} \left( \frac{Pr^{(t)}}{Pr^{(e)}} \right)_c^{1/3} \left( \frac{\mu_g^{(t)} \mu_{c,o}^{(e)}}{\mu_g^{(e)} \mu_{c,o}^{(t)}} \right)^m \quad (11-77)$$

where  $m$  is the power on the Reynolds number for coolant-side convection. The viscosity factor in equation (11-77) is the test-to-engine coolant Reynolds number ratio. As with the Prandtl number, this factor cannot be set independently, although its departure from unity is small. In fact, if the viscosity over the full temperature range  $t_g^{(e)}$  to  $t_{c,o}^{(t)}$  could be approximated by a power law

$$\mu \propto t^w \quad (11-78)$$

then, by equation (11-74), the test-to-engine coolant Reynolds number ratio (based on the film-cooling hole diameter and the ejection temperature) would be 1. The same coolant Reynolds number for actual and simulated conditions is important to ensure the same pressure drop through the internal cooling air passages for the two conditions.

If the cooled blade is to perform the same during a test as it does in the engine, there must be some normalized outer wall temperature which remains invariant between test and engine conditions. The most convenient dimensionless wall temperature includes only those temperatures which are known, namely the coolant supply temperature  $T_{c,in}$  and the effective gas temperature  $T_{g,e}$ . Hence, the dimensionless wall temperature  $\varphi$ , defined as

$$\varphi = \frac{T_{g,e} - T_{w,o}}{T_{g,e} - T'_{c,in}} \quad (11-79)$$

or some similar grouping of these three temperatures, is commonly used as a measure of the cooling performance of a given blade design.

Strict equality in  $\varphi$  for test and engine is, however, impossible with actual hardware, since the temperature drop through the wall is not scaled properly because of the lower heat flux at reduced temperature and pressure. It is easier to cool the blade at the reduced conditions, because the driving potential for convection cooling ( $T_{w,i} - T_c'$ ) is proportionately greater than at high temperature and pressure. How-

ever, for properly scaled test conditions, the difference between  $\varphi^{(t)}$  and  $\varphi^{(e)}$  is well within the range of experimental accuracy in most cases.

An example of similarity states generated by solving equations (11-71) to (11-77) simultaneously is given in table 11-II for a high-pressure, high-temperature gas-turbine-engine environment. Air properties were used rather than those for a given fuel-air ratio gas. For a test condition using ambient cooling air, the dimensionless wall temperature  $\varphi^{(t)}$  is 1 percent higher than what it would be in the actual engine.

Radiation can be a significant component of the total heat flux to a blade under high-temperature and high-pressure conditions and is not directly affected by film cooling with air. Since radiation cannot be conveniently simulated at the low-temperature and low-pressure test conditions, it must be accounted for in the heat-flux ratio  $q^{(t)}/q^{(e)}$  in equation (11-75).

TABLE 11-II.—SIMILARITY STATES

(a) Takeoff condition

Gas total temperature		Gas total pressure, atm.	Coolant temperature		$\varphi^{(t)}/\varphi^{(e)}$
K	°F		K	°F	
1 2200	1 3500	1 33.7	1 848	1 1066	-----
367	200	4.3	145	-199	1.04
478	400	6.0	188	-122	1.03
589	600	7.7	230	-45	1.02
700	800	9.4	273	31	1.01
758	905	10.3	294	70	1.01
811	1000	11.1	315	107	1.01
922	1200	12.9	357	182	1.00
1033	1400	14.6	399	259	1.00
1144	1600	16.4	442	335	1.00
1255	1800	18.2	485	413	1.00
1367	2000	19.9	528	490	1.00
1478	2200	21.7	571	568	1.00
1589	2400	23.5	613	644	1.00
1700	2600	25.3	656	721	1.00
1811	2800	27.1	699	799	1.00
1922	3000	28.9	743	878	1.00
2033	3200	30.9	786	955	1.00
2144	3400	32.8	828	1030	1.00

<sup>1</sup> Reference condition.

TABLE 11-II.—Concluded

(b) Cruise condition

Gas total temperature		Gas total pressure, atm.	Coolant temperature		$\varphi^{(t)} / \varphi^{(r)}$
K	°F		K	°F	
1 2200	1 3500	1 13.8	1 801	1 983	-----
367	200	1.7	139	-209	1.03
478	400	2.5	180	-136	1.02
589	600	3.2	220	-64	1.01
700	800	3.9	259	7	1.01
799	978	4.5	294	70	1.01
811	1000	4.6	299	78	1.01
922	1200	5.3	338	148	1.00
1033	1400	6.0	378	220	1.00
1144	1600	6.7	417	291	1.00
1255	1800	7.4	458	364	1.00
1367	2000	8.2	498	437	1.00
1478	2200	8.9	539	510	1.00
1589	2400	9.6	579	582	1.00
1700	2600	10.4	619	655	1.00
1811	2800	11.1	660	729	1.00
1922	3000	11.8	702	804	1.00
2033	3200	12.7	743	878	1.00
2144	3400	13.4	782	948	1.00

<sup>1</sup> Reference condition.

## REFERENCES

1. ESGAR, JACK B.; COLLADAY, RAYMOND S.; KAUFMAN, ALBERT: An Analysis of the Capabilities and Limitations of Turbine Air Cooling Methods. NASA TN D-5992, 1970.
2. KAYS, W. M.: Convective Heat and Mass Transfer. McGraw-Hill Book Co., Inc., 1966.
3. KESTIN, J.: The Effect of Free-Stream Turbulence on Heat Transfer Rates. Advances in Heat Transfer. Vol. 3. T. F. Irvine, Jr.; and J.P. Hartnett, eds., Academic Press, 1966, pp. 1-32.
4. AMBROK, G. S.: Approximate Solution of Equations for the Thermal Boundary Layer With Variations in Boundary Layer Structure. Soviet Phys.-Tech. Phys., vol. 2, no. 9, 1957, pp. 1979-1986.
5. SPALDING, D. B.; AND PATANKAR, S. V.: Heat and Mass Transfer in Boundary Layers. Chemical Rubber Co., 1968.
6. KERCHER, D. M.; AND TABAKOFF, W.: Heat Transfer by a Square Array of Round Air Jets Impinging Perpendicular to a Flat Surface Including the Effect of Spent Air. J. Eng. Power, vol. 92, no. 1, Jan. 1970, pp. 73-82.

TURBINE DESIGN AND APPLICATION

7. ARTT, D. W.; BROWN, A.; AND MILLER, P. P.: An Experimental Investigation Into Film Cooling With Particular Application to Cooled Turbine Blades. Heat Transfer 1970. Vol. 2. Ulrich Grigull and Erich Hahne, eds., Elsevier Publ. Co., 1970, pp. FC1. 7.1-FC1. 7.10.
8. GOLDSTEIN, R. J.; ECKERT, E. R. G.; ERIKSEN, V. L.; AND RAMSEY, J. W.: Film Cooling Following Injection Through Inclined Circular Tubes. Rep. HTL-TR-91, Minnesota Univ. (NASA CR-72612), Nov. 1969.
9. COLLADAY, RAYMOND S.; AND STEPKA, FRANCIS S.: Examination of Boundary Conditions for Heat Transfer Through a Porous Wall. NASA TN D-6405, 1971.
10. L'ECUYER, MEL R.; AND COLLADAY, RAYMOND S.: Influence of Porous-Wall Thermal Effectiveness on Turbulent-Boundary-Layer Heat Transfer. NASA TN D-6837, 1972.

## SYMBOLS

$A$	surface area of one side of volume element, $\text{m}^2$ ; $\text{ft}^2$
$A_f$	coolant-passage flow area, $\text{m}^2$ ; $\text{ft}^2$
$a$	augmentation factor, eq. (11-31)
$a_1, a_2, a_3$	coefficients in eqs. (11-49) to (11-51)
$B_x$	body-force component in $x$ direction, $\text{N/kg}$ ; $\text{lbf/lbm}$
$b_1, b_2, b_3$	coefficients in eqs. (11-49) to (11-51)
$C$	constants in eqs. (11-8) and (11-57)
$C_f$	friction coefficient, eq. (11-26)
$c_p$	specific heat at constant pressure, $\text{J/(kg)(K)}$ ; $\text{Btu/(lb)(}^{\circ}\text{R)}$
$c_1, c_2$	coefficients in eqs. (11-49) and (11-50)
$D$	diameter of leading-edge circle, impingement hole, or film-injection hole, $\text{m}$ ; $\text{ft}$
$\mathcal{D}$	dissipation term in eq. (11-42), $\text{W/m}^3$ ; $\text{Btu/(ft}^3\text{)(sec)}$
$d$	distance between volume elements (see fig. 11-10), $\text{m}$ ; $\text{ft}$
$F$	ratio of coolant mass flux to hot-gas mass flux
$f$	correction factor used in eq. (11-65)
$G$	mass flux, $\text{kg}/(\text{sec})(\text{m}^2)$ ; $\text{lb}/(\text{hr})(\text{ft}^2)$
$g$	conversion constant, 1; 32.17 ( $\text{lbm}(\text{ft})/\text{lbf}$ ) ( $\text{sec}^2$ )
$H$	total enthalpy, $\text{J/kg}$ ; $\text{Btu/lb}$
$h$	heat-transfer coefficient, $\text{W}/(\text{m}^2)(\text{K})$ ; $\text{Btu}/(\text{hr})(\text{ft}^2)(^{\circ}\text{R})$
$h_v$	internal volumetric heat-transfer coefficient, $\text{W}/(\text{m}^3)(\text{K})$ ; $\text{Btu}/(\text{hr})(\text{ft}^3)(^{\circ}\text{R})$
$h_s$	static enthalpy, $\text{J/kg}$ ; $\text{Btu/lb}$
$I$	term defined by eq. (11-41)
$J$	conversion constant, 1; 778 ( $\text{ft}(\text{lb})/\text{Btu}$ )
$K$	dimensional constant, 1; 3600 sec/hr
$K_t$	turbulent kinetic energy, $\text{J/kg}$ ; $\text{Btu/lb}$
$k$	thermal conductivity, $\text{W}/(\text{m})(\text{K})$ ; $\text{Btu}/(\text{hr})(\text{ft})(^{\circ}\text{R})$
$L$	coolant-passage characteristic length, $\text{m}$ ; $\text{ft}$
$l$	wall thickness, $\text{m}$ ; $\text{ft}$
$M$	Mach number
$m$	exponents used in eqs. (11-8), (11-45), and (11-48)
$Nu$	Nusselt number
$n$	exponents used in eqs. (11-8), (11-45), (11-56), and (11-57)
$Pr$	Prandtl number
$p$	pressure, $\text{N/m}^2$ ; $\text{lb}/\text{ft}^2$
$Q$	heat-generation term, $\text{W}/\text{m}^3$ ; $\text{Btu}/(\text{sec})(\text{ft}^3)$
$q$	heat flux, $\text{W}/\text{m}^2$ ; $\text{Btu}/(\text{hr})(\text{ft}^2)$
$R$	gas constant, $\text{J}/(\text{kg})(\text{K})$ ; $(\text{ft})(\text{lbf})/(\text{lbm})(^{\circ}\text{R})$
$Re$	Reynolds number
$r$	recovery factor, eq. (11-27)
$St$	Stanton number

<i>s</i>	slot width, m; ft
<i>T</i>	temperature, K; °R
<i>t</i>	gas static temperature, K; °R
<i>u</i>	component of gas velocity in direction along surface ( <i>x</i> -direction), m/sec; ft/sec
<i>V<sub>j</sub></i>	volume of <i>j</i> <sup>th</sup> element, m <sup>3</sup> ; ft <sup>3</sup>
<i>v</i>	component of gas velocity in direction normal to surface ( <i>y</i> -direction), m/sec; ft/sec
<i>w</i>	mass flow rate, kg/sec; lb/sec component of gas velocity in direction perpendicular to the boundary layer plane ( <i>x-y</i> plane), m/sec; ft/sec
<i>x</i>	distance along surface from leading edge, m; ft
<i>x<sub>n</sub></i>	center-to-center distance between impingement holes in the direction of flow, m; ft
<i>y</i>	coordinate distance normal to surface, m; ft
<i>z<sub>n</sub></i>	distance between impingement holes and blade inner wall, m; ft
$\alpha$	heat diffusivity, m <sup>2</sup> /sec; ft <sup>2</sup> /sec
$\Gamma$	specific heat ratio correction factor, eq. (11-68)
$\gamma$	ratio of specific heat at constant pressure to specific heat at constant volume
$\Delta$	enthalpy thickness, m; ft
$\epsilon$	ratio of heat transfer coefficient with film cooling to heat transfer coefficient without film cooling
$\eta$	cooling effectiveness
$\theta$	momentum thickness, m; ft
$\mu$	viscosity, (N)(sec)/m <sup>2</sup> ; lb/(ft)(sec)
$\nu$	momentum diffusivity (kinematic viscosity), m <sup>2</sup> /sec; ft <sup>2</sup> /sec
$\rho$	density, kg/m <sup>3</sup> ; lb/ft <sup>3</sup>
$\tau$	local shear stress, N/m <sup>2</sup> ; lb/ft <sup>2</sup>
$\Phi$	angular distance from leading-edge stagnation point, deg
$\varphi$	dimensionless wall temperature
$\varphi_1, \varphi_2$	coefficients in eq. (11-48)
$\psi$	term defined by eq. (11-52)
$\omega$	exponent in eq. (11-78)

Subscripts:

<i>a</i>	adiabatic
<i>CP</i>	constant property
<i>c</i>	coolant
<i>cf</i>	crossflow
<i>conv</i>	convection
<i>crit</i>	critical, referring to transition from laminar to turbulent flow

<i>D</i>	with hole diameter as characteristic dimension
<i>e</i>	effective
<i>film</i>	film
<i>g</i>	hot gas at free-stream condition
<i>h</i>	hole
<i>i</i>	inner
<i>imp</i>	impingement
<i>in</i>	inlet
<i>j</i>	<i>j</i> th element
<i>L</i>	laminar
$\mathcal{L}$	with $\mathcal{L}$ as characteristic length
<i>le</i>	leading edge
<i>o</i>	outer
<i>ref</i>	reference
<i>s</i>	downstream edge of slot
<i>stag</i>	stagnation
<i>T</i>	turbulent
<i>t</i>	transpiration
<i>w</i>	wall
<i>x</i>	{ local value with <i>x</i> as characteristic length}
$\Delta$	with $\Delta$ as characteristic length
$\theta$	with $\theta$ as characteristic length
$\infty$	approaching leading edge

Superscripts:

( <i>e</i> )	engine condition
( <i>t</i> )	test condition
,	{ total state (referring to <i>T</i> and <i>p</i> ) fluctuating component (referring to $\rho$ , <i>v</i> , $\lambda$ , <i>u</i> , and <i>w</i> )}



## **CHAPTER 12**

# **Experimental Determination of Aerodynamic Performance**

**By Edward M. Szanca and Harold J. Schum**

The preceding chapters have been concerned with primarily the theoretical aspects relating to turbines and turbine design. A great deal of consideration has been directed toward turbine blading, since, aerodynamically, the blading is the turbine. Associated hardware for the entire turbine assembly (rotor disks, shafting, bearings, casings etc.) is designed on the basis of mechanical criteria. Once the turbine is designed and built, it must be determined whether or not the aerodynamic design goals have been met. Only by testing the turbine can this be determined.

In addition to the overall performance of a turbine, a breakdown of the separate losses contributing to the overall loss is often desired. The stator loss can be obtained readily from experimental measurements, as discussed in chapter 7 (vol. 2). Rotor losses cannot be obtained easily from direct measurements; they are usually obtained indirectly from the stator loss and the overall performance measurements.

In developing a test facility and program, the researcher must determine which performance parameters he is interested in evaluating. The nature of the test facility, the instrumentation necessary to obtain the desired stator and/or overall performance parameters, and the manner in which these parameters vary with turbine operating conditions are the subject of this chapter.

## TEST FACILITY AND MEASUREMENTS

The manner in which stator performance is expressed and computed is discussed in detail in chapter 7 (vol. 2) and will not be discussed herein. The parameters generally used to define turbine overall performance are mass flow rate, torque, specific work, and efficiency. These parameters are usually determined for ranges of rotative speed and pressure ratio in order to fully define the performance of the turbine. The mass flow rate, torque, rotative speed, inlet and exit pressures, and inlet temperature (needed to determine efficiency) are measured directly in the turbine test facility. Specific work is then calculated from the equation

$$\Delta h' = K \frac{\Gamma N}{Jw} \quad (12-1)$$

where

- $\Delta h'$  turbine specific work, J/kg; Btu/lb
- $K$  conversion constant, 1;  $\pi/30$  (rad)(min)/(rev)(sec)
- $\Gamma$  torque, N-m; lb-ft
- $N$  rotative speed, rad/sec; rev/min
- $J$  conversion constant, 1; 778(ft)(lb)/Btu
- $w$  mass flow rate, kg/sec; lb/sec

Efficiency is obtained by dividing the actual work  $\Delta h'$  by the ideal work. Ideal work is a function of the turbine inlet total temperature and the pressure ratio across the turbine, as shown by equation (2-48b) or (2-49b) of chapter 2 (vol. 1). The inlet pressure is always the total pressure. The outlet pressure used to define ideal work, however, depends on the particular efficiency desired. Total efficiency is based on outlet total pressure and is most meaningful where all of the outlet velocity is useful or recoverable. Static efficiency is based on outlet static pressure and is most meaningful where all of the outlet velocity is lost. Rating efficiency is based on a pressure corresponding to the recovery of only the axial component of outlet velocity and, accordingly, is most meaningful where only the axial component of the outlet velocity is useful. Rating efficiency is not as commonly used as are the total and static efficiencies, which were discussed in chapter 2 (vol. 1).

In this section, a representative test facility will be described, and the types of devices generally used to make the required measurements will be discussed. Data acquisition and reduction systems will not be discussed in this chapter. These can vary from visual reading of manometers and gages with slide-rule computations to completely automatic electronic data acquisition with on-line computer process-

ing. A general discussion of data measurement, acquisition, transmission, and recording systems can be found in texts such as reference 1.

#### Description of Test Facility

A turbine test facility consists of the research turbine, a gas supply, an exhaust system, associated piping with control valves, a power absorber, and the instrumentation needed to make the desired measurements. A schematic diagram of a turbine test facility at the NASA Lewis Research Center is shown in figure 12-1. This facility, a photograph of which is shown in figure 12-2, is used to test single-stage or multistage turbines of about 76 centimeters (30 in.) in diameter. It is generally representative of most turbine test facilities and is used here as an example for this discussion. In such a facility, removal of the turbine rotor gives the room necessary to place survey instrumentation behind the stator and, thereby, transforms the rotating rig into a stator annular cascade.

Most turbine component testing is conducted with air at ambient temperature or slightly heated. This is commonly called cold-air

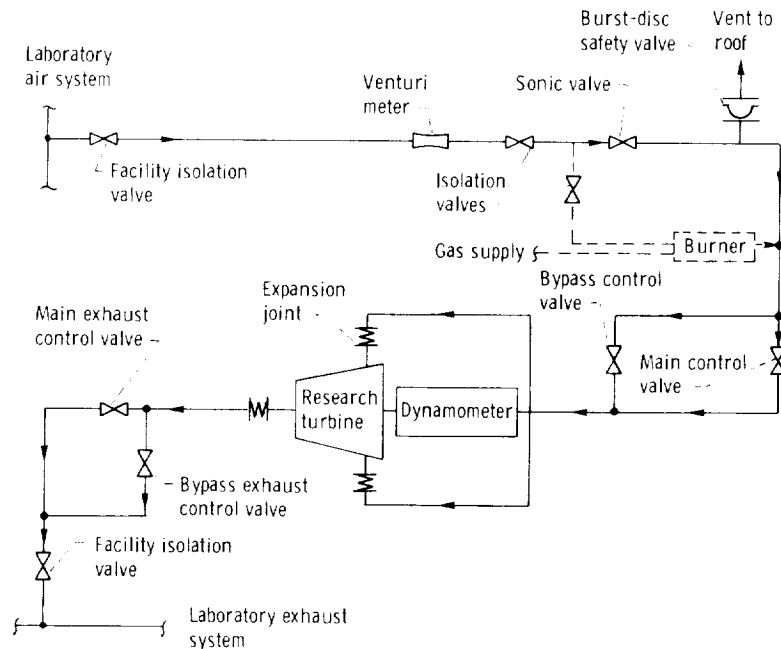


FIGURE 12-1.—Flow schematic of a turbine test facility.



FIGURE 12-2.—Turbine test facility.

testing. Performance parameters are reported in terms of equivalent values based on standard sea-level conditions of pressure (10.133 N/cm<sup>2</sup> or 14.696 psia) and temperature (288.2 K or 518.7° R). This was discussed in chapter 2 (vol. 1). Using turbine-inlet test conditions of pressure and temperature near the standard values results in lower flow and power levels than would be encountered in an actual application and thereby facilitates testing. Yet, the model turbine velocity diagrams are similar to and the Mach numbers are the same as those of the actual turbine. Only Reynolds number, then, can present a dissimilarity; however, for the larger turbines, this effect of Reynolds number on turbine performance was found to be negligible. For smaller turbines, where Reynolds number effects are more important, turbine inlet pressure can be varied to obtain the proper Reynolds number.

Referring to figure 12-1, air for the turbine is supplied by the 27.6-N/cm<sup>2</sup>-gage (40-psig) air system of the laboratory. A calibrated venturi meter is located in a straight section of the 40.6-centimeter (16-in.) air-supply line for the purpose of metering the air flow. This

## EXPERIMENTAL DETERMINATION OF AERODYNAMIC PERFORMANCE

piping is sized (as was all piping) such that the air velocities will not exceed 61 meters per second (200 ft/sec). Location of the air-metering device in the high-pressure supply line affords a relatively constant upstream pressure and may minimize the number of metering devices required for a range of flows. A further discussion of air-metering devices is presented in a subsequent section.

Downstream of the venturi meter is an isolation valve controllable by the turbine operator. A 30.5-centimeter (12-in.) sonic valve provides a high pressure drop to facilitate burner operation and automatic inlet-pressure control. A burst-disc safety valve and vent line provide protection from excessive pressure. Further downstream is the 50.8-centimeter (20-in.) main control valve used to establish the desired turbine-inlet pressure (for the example turbine, this was 76.2 cm (30 in.) of Hg absolute). The 15.2-centimeter (6-in.) bypass control valve permits fine control of the turbine-inlet pressure. The air then diverts into two 50.8-centimeter (20-in.) lines to provide dual entry of lower velocity air to the turbine entry plenum. (These lines can be seen in fig. 12-2.)

After passing through the turbine, the air is discharged to the altitude exhaust system of the laboratory through a 121.9-centimeter (48-in.) main control valve and a 40.6-centimeter (16-in.) bypass control valve. These valves permit the turbine operator to vary the pressure ratio across the turbine while the turbine-inlet pressure is maintained constant by automatic control. This type of pressure-ratio control has been most successful with small turbines. With large turbines, however, there is a slower response because of the large pipe volume between the turbine and the inlet control valve.

A burner installation is shown (in fig. 12-1) in phantom, because its use is optional. The purpose of the burner is to elevate the turbine-inlet temperature so as to avoid icing problems at the turbine exit. In this facility a single commercial jet-engine burner can, modified for operation with natural gas, is used. Some of the high-pressure air is bypassed to the burner and the heated air is then mixed with the remaining air. The desired turbine inlet temperature is maintained by controlling both the amount of bypassed air and the fuel flow. This particular burner has the capability to heat a maximum air flow of 23.6 kilograms per second (52 lb/sec) from ambient temperature to 422 K (300° F).

In general, burners using gasoline, jet fuel, or natural gas provide a relatively simple and inexpensive means of heating the air. However, combustion products are added to the air, and these must be accounted for in the performance calculations. Electrical heaters provide clean heat, but are generally used only where flow rates are low, because of the cost and complexity of large installations.

All turbines and test facilities must be designed with safety features. The following are some of the potentially unsafe conditions that must be guarded against by constant monitoring:

- (1) Low supply of turbine and dynamometer lubricating oil
- (2) Low pressures of turbine and dynamometer lubricating oil
- (3) High temperature in bearings
- (4) High temperature of dynamometer outlet water
- (5) Low pressure of dynamometer water supply
- (6) High temperature of turbine inlet gas
- (7) High (or low) temperature of turbine exit gas
- (8) High pressure of turbine inlet gas
- (9) High pressure of turbine exit gas
- (10) Overspeed of turbine rotor
- (11) Reduced clearance between rotor and casing
- (12) Excessive rig vibration
- (13) Excessive shaft orbit

Interlocks on some of the monitoring systems prevent turbine starting. Some monitors provide for only an audible alarm during operation. Others provide a signal to rapidly shut the valves in the inlet air line as well as in the heater gas system. This quickly stops rotor rotation in order to prevent damage to the turbine and facility.

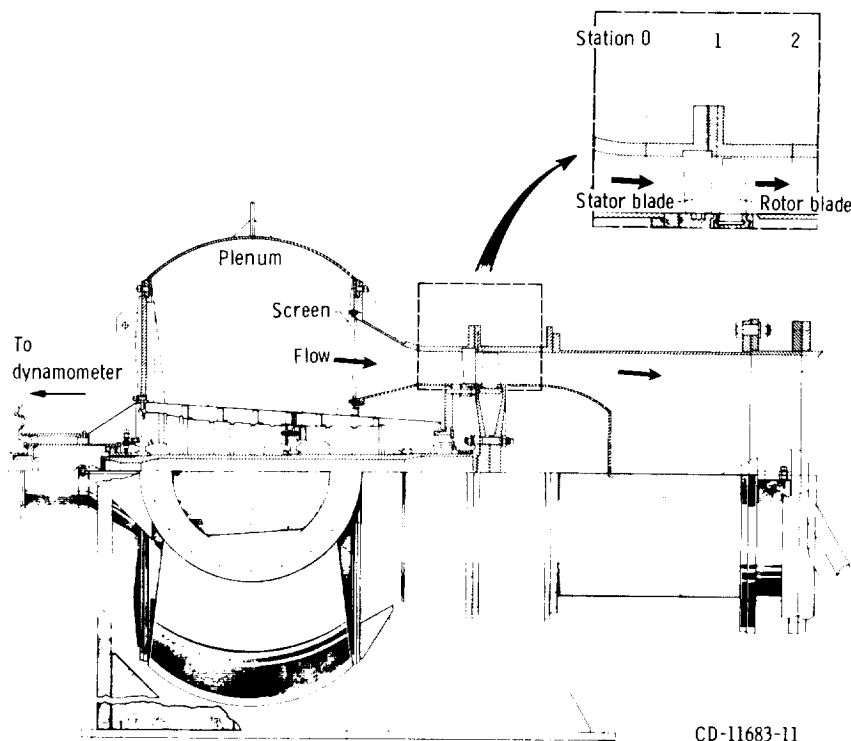
### **Research Turbine**

A schematic diagram of one of the research turbines used in this test facility is presented in figure 12-3. An enlarged view of the test section with instrumentation stations indicated is also shown. As stated previously, the air enters a plenum from two sides; the plenum was designed with as much volume as feasible to provide for minimum velocity and minimum pressure distortion. A screen is shown located upstream of a converging section to further ensure a symmetrical circumferential pressure distribution to the turbine blades. This screen has an approximate 50 percent effective area, giving a pressure drop of 2 dynamic heads.

A short, straight, annular passage is provided between the converging inlet section and the first row of blades for the purpose of installing turbine-inlet pressure and temperature measurement devices. The inlet measuring station (station 0 of fig. 12-3) is located about  $1\frac{1}{2}$  blade chords upstream of the stator blades. Since the inlet velocity is low, the insertion of probes does not significantly disturb the flow entering the blading.

A straight, annular flow passage is also provided downstream of the turbine blades to measure the turbine-outlet air state (measuring station 2, fig. 12-3). Measurements are made about 2 blade-chord

EXPERIMENTAL DETERMINATION OF AERODYNAMIC PERFORMANCE



CD-11683-11

FIGURE 12-3.—Schematic diagram of turbine test section.

lengths downstream of the rotor, where the exit air is relatively stabilized and uniform.

Both the inlet and outlet sections of the test turbine are somewhat idealized as compared to an actual jet-engine turbine installation. The latter has a burner immediately preceding the turbine inlet, and a tail cone immediately following the last row of blades. Flow-passage diameters vary. Also, for the sake of engine weight saving, minimum axial length is required. Accurately measuring the state conditions before and after the turbine blading in varying area passages is extremely difficult, and this is the reason for the use of straight, annular flow passages in the test turbine.

#### Flow-Property Measurements

The flow-property measuring stations are located in the axial positions indicated in figure 12-3. There are numerous types and

- ✖ Temperature rake
- Total-pressure probe
- Static-pressure tap
- Angle probe

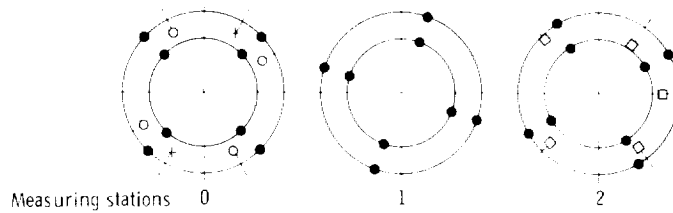


FIGURE 12-4.—Schematic diagram of turbine instrumentation.

varying types of probes available to make the desired measurements. We will discuss primarily the instruments used in the example research turbine to obtain the desired measurements of pressure, temperature, and flow angle. The instrumentation located at the turbine inlet and outlet, as well as at the stator exit, is shown in figure 12-4.

In general, all turbine experimental investigations, irrespective of turbine size or number of stages, require the same overall data. The size of the turbine determines whether duplication of research instrumentation can be afforded. For large turbines, the relative size of the probes with respect to the flow passages can be considered negligible. In small turbines, the presence of the various probes with their associated blockage could have an effect on the turbine expansion process, and, therefore, on the values being measured. This consideration usually limits the number and size of probes.

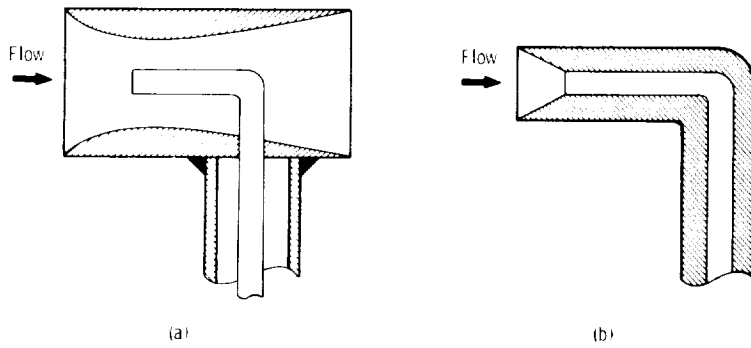
*Static pressure.*—At each measuring station, as shown in figure 12-4, there are four static-pressure taps, diametrically opposed and 90° apart, on both the inner and outer walls. This multiplicity provides a check on the circumferential pressure distribution. In order to minimize the amount of instrumentation and data, multiple taps are often manifolded to provide a single reading. If the individual pressures differ, however, some flow circulation occurs and the observed pressure reading may not be the true average of the individual pressures.

As part of the stator performance test, it is often desired to determine the static-pressure distribution along the blade surface. As explained in a subsequent section, this information is used to calculate the blade surface velocities. Static-pressure taps are installed

## EXPERIMENTAL DETERMINATION OF AERODYNAMIC PERFORMANCE

along the hub, mean, and tip sections of the blade. If the number of tubes that can be installed in any one blade is limited by the size of the blade, then the desired taps can be divided among two or more adjacent blades. For the research turbine being discussed, the blades are hollow and fairly large; thus, installing the taps presented no major problem. The pressure-tap hole size used is approximately 0.0254 centimeter (0.010 in.) in diameter. A small hole is desirable so as not to disturb the flow; however, too small a hole results in a long response time.

*Inlet total pressure.*—Four shielded total-pressure probes, 90° apart, are located at the inlet measuring station (see fig. 12-4) and are all immersed to the area center of the flow passage. One such probe is shown in figure 12-5(a). The shielding, which is about 0.48 centimeter (0.19 in.) in diameter and twice that in length, is such that pressure readings are relatively insensitive to yaw for some 40°. The unshielded probe shown in figure 12-5(b) is also commonly used for total-pressure measurement. This probe has an insensitivity to yaw for about 20°.



(a) Shielded probe. (b) Unshielded probe.

FIGURE 12-5.—Total-pressure probes.

The turbine-inlet total-pressure readings serve as a check on the circumferential pressure distribution and are used during turbine testing to establish and maintain a constant turbine-inlet total pressure. However, the turbine-inlet total-pressure value that is often used to define pressure ratio when reporting turbine performance is a value based on experimental measurements of mass flow rate, static

pressure, and total temperature and obtained by the following equation, with the flow angle  $\alpha$  assumed to be zero at the turbine inlet:

$$p' = p \left[ \frac{1}{2} + \sqrt{\frac{1}{4} + \frac{\gamma-1}{2g\gamma} \left( \frac{w}{pA_{an}} \right)^2 \cos^2 \alpha} \right]^{\gamma/(\gamma-1)} \quad (12-2)$$

where

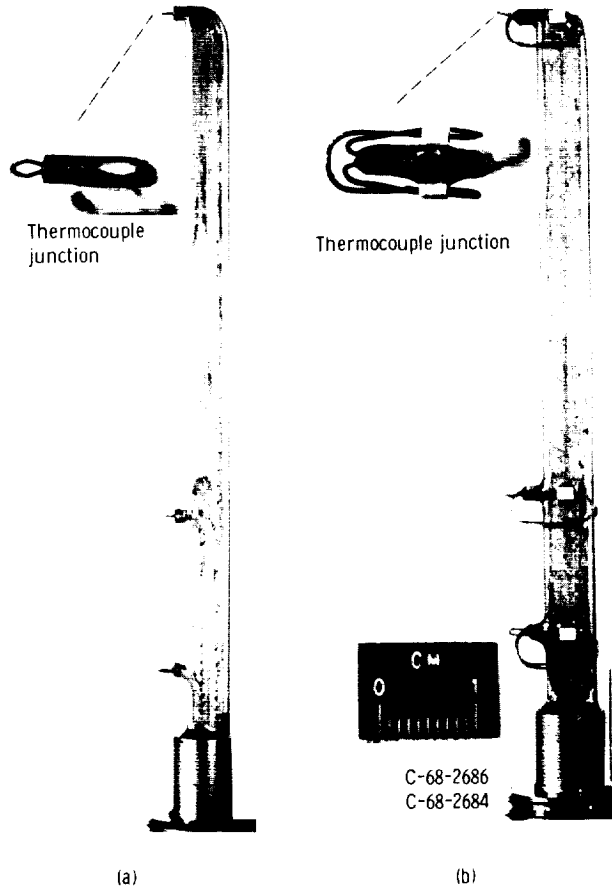
- $p'$  total pressure, N/m<sup>2</sup>; lb/ft<sup>2</sup>
- $p$  static pressure, N/m<sup>2</sup>; lb/ft<sup>2</sup>
- $\gamma$  ratio of specific heat at constant pressure to specific heat at constant volume
- $g$  conversion constant, 1; 32.17 (lbm)(ft)/(lbf)(sec<sup>2</sup>)
- $A_{an}$  annulus area, m<sup>2</sup>; ft<sup>2</sup>
- $R$  gas constant, J/(kg)(K); (ft)(lbf)/(lbm)(°R)
- $T'$  total temperature, K; °R
- $\alpha$  flow angle measured from axial direction, deg

This calculated value of turbine-inlet total pressure is thought to be more representative of the true average value than is the experimental value.

*Inlet temperature.*—Two thermocouple rakes, spaced 180° apart, are located at the turbine inlet measuring station (see fig. 12-4). These rakes, which are of a type similar to that shown in figure 12-6(a), contain a number of thermocouples situated at the area center radii of equal annular areas. The particular rake shown in figure 12-6(a) was used to determine the temperatures at the center, the area-mean radius, and the wall of the outlet duct of a radial-inflow turbine. Provisions are made for individual readings as well as for the average of all the readings. The latter facilitates testing with the burner in operation, where a constant inlet temperature is maintained. Automatic fuel regulation to the burner is provided for this purpose.

Measurement of temperature at low Reynolds number can present a problem due to heat conduction effects. This problem did not exist for the large research turbine being used as an example herein, but was encountered in testing some small turbines as discussed in reference 2. A large amount of bare thermocouple wire must be exposed to the flow in order to make the conduction error negligible. The conventional thermocouple shown in figure 12-6(a) has a ratio of exposed wire length to diameter of about 12, which is inadequate for good accuracy at low Reynolds number. The modified thermocouple shown in figure 12-6(b) has a wire length-to-diameter ratio of about 170. This modified probe gives excellent results.

EXPERIMENTAL DETERMINATION OF AERODYNAMIC PERFORMANCE



(a) Conventional type. (b) Modified type.  
FIGURE 12-6.—Thermocouple rake configurations.

*Stator outlet.*—During turbine testing, the only measurement made at the stator outlet is the previously mentioned static pressure. For stator performance testing, the rotor is removed, and a total-pressure survey probe is installed. Although it is desirable also to obtain stator-outlet radial and circumferential static-pressure surveys, the problems associated with conventional wedge probes, especially the effect of probe blockage on the value being measured, make such measurements



FIGURE 12-7.—Total-pressure survey probe installed in test facility.

unreliable. The required static pressures are obtained by interpolation from the values measured at the hub and tip wall taps. The total-pressure probe used in the test facility is shown in figure 12-7. This probe is fixed at an angle previously determined to be the average flow angle. Note that the probe has two sensing elements; these are required to obtain measurements at both the inner and outer walls.

The total-pressure survey equipment is shown in figure 12-8. The actuator provides for radial movement of the probe, and the motor-driven outer-wall saddle provides for circumferential movement. The probe shown in this figure does not have the same stem configuration as the previously shown probe (fig. 12-7) that was used in the example facility. Considerations regarding the effects of stem blockage, sensing

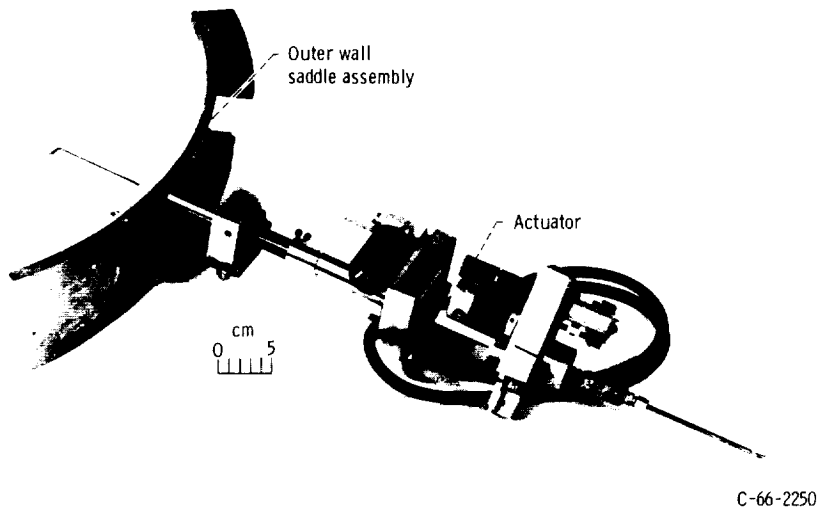


FIGURE 12-8.—Total-pressure survey equipment.

element diameter, and measurement distance behind the blade trailing edge are discussed in reference 3.

Although not used in the particular facility serving as the discussion example herein, optical laser techniques have recently come into use for directly measuring velocity magnitude and direction. A laser Doppler velocimeter, such as described in reference 4, allows the velocity measurements to be made without the use of flow-disturbing probes.

*Turbine outlet.*—Combination probes, with the type of sensing head shown in figure 12-9, capable of measuring total pressure, temperature, and flow angle are located at the turbine exit. Figure 12-4 shows that five of these combination probes are distributed circumferentially at measuring station 2. Each probe is located at the area center radius of one of five equal annular areas. In general, turbine size influences the number of probes permissible.

Measurement of flow angle is accomplished by means of a conventional self-balancing probe system. The probe shown is of a 3-tube design, with the center tube used to measure total pressure. The two side tubes are symmetrically located with respect to the center tube and are exposed to a pressure that ranges between the total pressure and the static pressure. The openings in the side tubes are in planes making an angle of 45° with the center tube. These side tubes are connected to the two sides of a diaphragm in a balance capsule. A

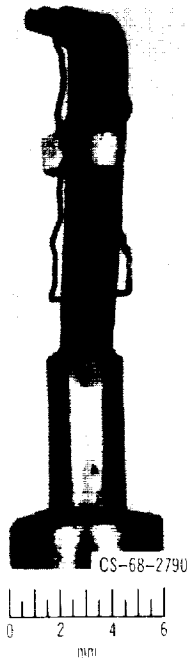


FIGURE 12-9.—Combination-probe sensing head.

differential transformer in the capsule is actuated by the diaphragm, so that an error signal is generated when the pressures in the side tubes of the probe are unequal. A servo-system operates to reduce the error to zero by pointing the probe into the flow.

Exit total-temperature and total-pressure measurements are generally not used for the primary determination of turbine efficiency, but they are used to determine values in order to check for gross discrepancies. It has been found that measurement of torque and use of equation (12-1) provides more reliable values of specific work than does measurement of exit total temperature. This is especially true if the temperature probe is in a fixed position and large variations in flow angle occur over the range of operating conditions. Even with a self-balancing probe, the exit passage would have to be surveyed and the results integrated in order for the specific work to be determined accurately.

Exit total pressure, which is used for the calculation of ideal work, is usually determined from equation (12-2). When the exit flow angle is small, use of equation (12-2) yields more reliable values of exit total pressure than does direct measurement. When the exit flow angle is

large, the radial variations in pressure and angle in the exit passage become large. In this case, unless integrated values can be obtained for use in equation (12-2), the choice between calculation and measurement of exit total pressure is not clear-cut.

### Mass-Flow Measurement

Flows are usually measured with variable-head meters, which depend on the pressure differential caused by a constriction in the fluid pipe. The primary element is a restriction such as a venturi, nozzle, or orifice placed in the pipe through which the fluid is flowing. The secondary element may be a simple U-tube manometer or an intricate pressure recording device. Each of these meters has certain advantages and disadvantages, and the selection of any particular meter depends on the requirements and constraints of the particular application.

All of these variable head meters have the same basic equation for the computation of the rate of flow:

$$W = A_t M C E Y \sqrt{2g\rho_{in}(p_{in} - p_t)} \quad (12-3)$$

where

- $A_t$  flow area of meter throat,  $\text{m}^2$ ;  $\text{ft}^2$
- $M$  approach velocity factor
- $C$  discharge coefficient
- $E$  thermal expansion factor
- $Y$  compressibility factor
- $\rho_{in}$  density at meter inlet,  $\text{kg/m}^3$ ;  $\text{lb/ft}^3$
- $p_{in}$  static pressure at meter inlet,  $\text{N/m}^2$ ;  $\text{lb/ft}^2$
- $p_t$  static pressure at meter throat,  $\text{N/m}^2$ ;  $\text{lb/ft}^2$

The approach velocity factor is

$$M = \frac{1}{\sqrt{1 - \left(\frac{D_t}{D_{in}}\right)^4}} \quad (12-4)$$

where  $D$  is diameter, in m or ft.

The discharge coefficient  $C$  accounts for the difference between the actual flow rate and the theoretical flow rate and is significantly different for each type of meter. Although good approximations for discharge coefficients can be made from published data, a direct calibration of the meter should be made to assure accurate results. The thermal expansion factor  $E$  accounts for the fact that the meter throat area is usually determined from measurements obtained at room temperature, which usually is not equal to the temperature of the fluid flowing through the meter.

The compressibility factor for nozzles and venturi meters is

$$Y = \left\{ \frac{\gamma}{\gamma-1} \left( \frac{p_t}{p_{in}} \right)^{2/\gamma} \left[ \frac{1 - \left( \frac{p_t}{p_{in}} \right)^{(\gamma-1)/\gamma}}{1 - \frac{p_t}{p_{in}}} \right] \left[ \frac{1 - \left( \frac{D_t}{D_{in}} \right)^4}{1 - \left( \frac{D_t}{D_{in}} \right)^4 \left( \frac{p_t}{p_{in}} \right)^{2/\gamma}} \right] \right\}^{1/2} \quad (12-5)$$

The derivation of equation (12-5), along with curves showing  $Y$  as a function of  $p_t/p_{in}$  and  $D_t/D_{in}$ , is presented in reference 5. For most concentric orifices having  $(\Delta p/p_{in}) < 0.3$ , the value of  $Y$  can be determined from the following empirical equation from reference 5:

$$Y = 1 - \left[ 0.41 + 0.35 \left( \frac{D_t}{D_{in}} \right)^4 \right] \frac{(p_{in} - p_t)}{p_{in}\gamma} \quad (12-6)$$

*Venturi tube.*—Figure 12-10 shows the important features of a venturi tube, which consists of a cylindrical entrance section, a converging section, a cylindrical throat section, and a diffuser section. The tubes are usually cast and have machined internal surfaces. The diffuser section usually is made with an included angle of about  $7^\circ$  with the object of accomplishing a maximum recovery of kinetic energy while minimizing friction loss. The total pressure loss from the venturi-tube inlet to exit is from 10 to 20 percent of the differential pressure between the inlet and the throat. The venturi tube has disadvantages in that it is bulky, difficult to construct (particularly so as to provide reproducibility), more expensive than other head meters, and requires a long, straight run of piping.

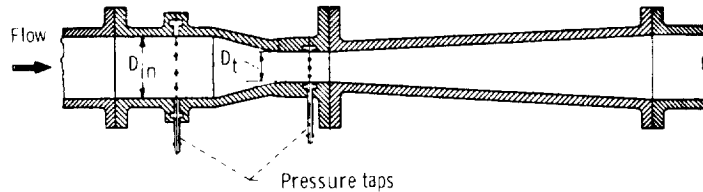


FIGURE 12-10.—Venturi tube.

*Flow nozzle.*—Figure 12-11 shows the shape of a commonly used flow nozzle. The flow nozzle approaches, to some extent, the venturi tube without the diffuser section. The high pressure recovery obtained with the venturi is thus lost, and the nozzle has a pressure loss of 30

Static-pressure taps

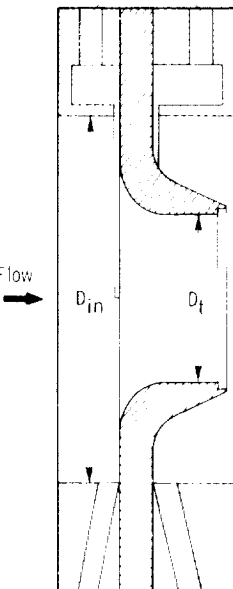


FIGURE 12-11.—Flow nozzle.

percent or more, depending on area ratio, of the differential pressure between the inlet and the throat. The flow coefficient (product of approach factor  $M$  and discharge coefficient  $C$ ) for a nozzle is about 0.98.

*Orifice.*—The sharp-edged orifice (fig. 12-12) is probably the most widely used of the various head meters. Because of the inward flow of the streamlines on the upstream side of the plate, the minimum stream area occurs downstream from the orifice edge. This minimum area is known as the *vena contracta*, and it is at this area that the minimum pressure is obtained. The orifice has a pressure loss somewhat greater than that for a flow nozzle. The flow coefficient for an orifice is about 0.65. This low value is due to the effective minimum area being at the *vena contracta* rather than at the orifice itself.

It is possible to make, in most machine shops, an orifice with which published coefficients may be used. If the hole is carefully made according to specifications, a high degree of reproducibility of flow conditions is possible. The upstream edge must be sharp, and the axial length of the cylindrical portion must not exceed 5 percent of the in-

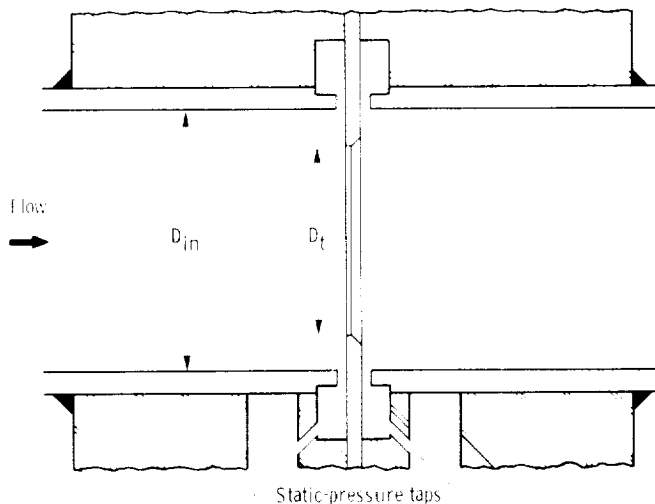


FIGURE 12-12.—Sharp-edged orifice.

side diameter of the pipe. Because it is possible to construct two or more orifices which will have the same coefficients when calibrated, the orifice is extensively used.

#### Torque Measurement

In turbine-component tests, an accurate measurement of torque produced by the turbine is of prime consideration in evaluating turbine performance. The devices most commonly used to determine turbine torque are cradled absorption dynamometers. Simply, the absorption dynamometer converts the energy supplied by the turbine into heat. This heat, in turn, is dissipated to the surroundings, where it generally serves no useful purpose. The dynamometer provides a load for the turbine, and this is used as the turbine speed controller.

Absorption dynamometers to be discussed in this section include (1) hydraulic, or fluid-friction, brakes; (2) electromagnetic brakes; (3) electric generators used as brakes; and (4) airbrakes. In addition, methods for measuring dynamometer force and types of torque meters other than absorption dynamometers are discussed.

*Hydraulic dynamometer.*—These units are frequently called water brakes, since the fluid is almost always water. A typical water brake is shown in figure 12-13, which shows clearly the cradle mounting generally used in dynamometer installations. The shaft is coupled

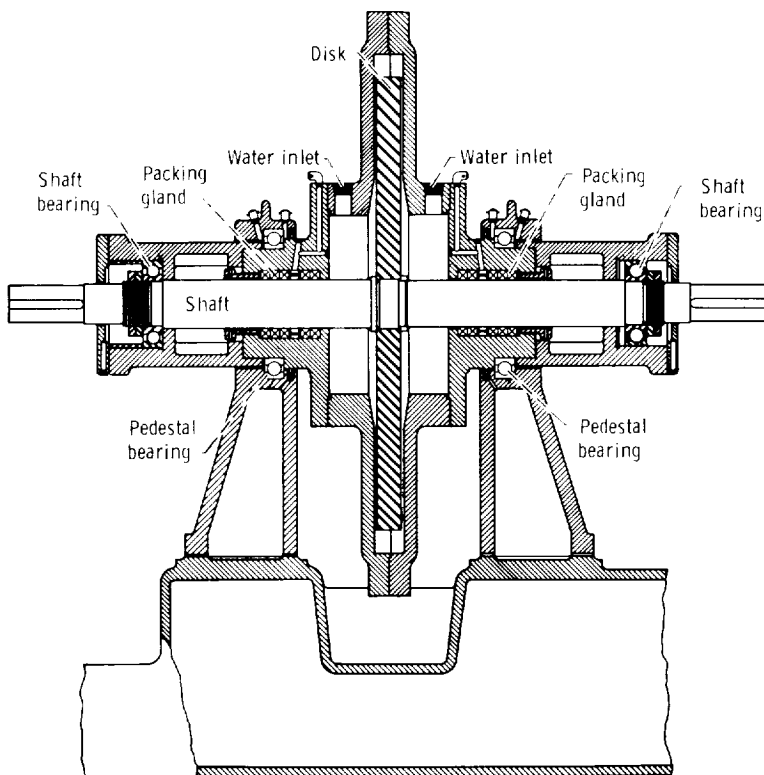


FIGURE 12-13.—Hydraulic dynamometer. (Courtesy of Murray Iron Works Co.)

directly to the test turbine and transmits the developed torque to the housing through the shaft bearings, the packing glands, and fluid friction on the disk. The housing is supported in the pedestal bearings so that it is free to rotate, within limits. As the shaft rotates, the housing tends to rotate with it. A scale attached to an arm on the housing permits determination of the turning moment, and the power absorbed may be computed.

Water fed into the disk compartment is thrown by centrifugal force to the periphery of the disk, where it forms a ring. As the discharge valves are closed or the inlet valves opened further, the water ring depth is increased; this results in greater frictional resistance between the disk and the housing, and a consequently increased absorption capacity of the brake. The amount of water circulated should be sufficient to prevent the formation of steam at any point, since such

action would cause momentary unloading. With a constant water level, the power-absorbing capacity of this brake varies almost as the cube of the speed. This characteristic (i.e., increase of torque with increase of speed, and vice versa) is typical of all fluid-friction and electrical-type dynamometers and makes them particularly desirable for testing nongoverned engines.

Some water brakes are provided with through-holes in the disk near the outer periphery. This tends to further increase the friction, and can increase power absorption by as much as an order of magnitude. Care must be exercised, however, because erosion of the disk can occur, particularly in the vicinity of these holes. Another way to increase power absorption capability is by staging; that is, by using more than one disk.

*Eddy-current dynamometer.*—The eddy-current dynamometer is shown in the two views of figure 12-14. In this device, the stator is supported on the pedestal bearings so that any torque may be transmitted by means of the torque arm and measured by the scale. The rotor is mounted on the shaft, which is supported in the stator in bearings. The stator carries a coil, which, when energized with direct current, magnetizes the stator and rotor. On the rotor are teeth with ends machined to produce a small air gap between them and the opposing face of the stator. The lines of force enter the rotor principally through the ends of the teeth, so that as the rotor is moved by the device being tested, the lines of force are caused to sweep through the

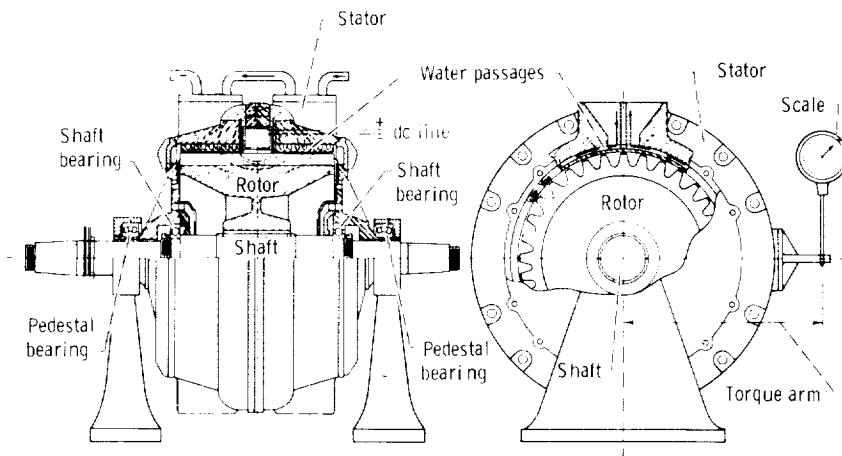


FIGURE 12-14.—Eddy-current dynamometer. (Courtesy of Mid-West Dynamometer and Engineering Co.)

iron of the stator. The magnetic attraction between the rotor and the stator causes the stator to try to turn with the rotor. The lines of force sweeping through the stator induce currents therein; this energy is dissipated to cooling water flowing through passages in the stator.

The dynamometer shown in figure 12-14 is called a dry-gap type, because the coolant water does not contact the rotor. A wet-gap eddy-current dynamometer is also commonly used. The wet-gap type has a cylindrical iron-core rotor, and the water flows from passages in the stator directly onto the rotor. Eddy-current dynamometers can be connected in series to give any required power absorption capability.

*dc dynamometer.*—A dc electric motor-generator, with frame or stator cradled, provides the most versatile dynamometer. It can be used to measure the power required to drive a device (testing a pump or a compressor) as well as to absorb the output of a prime mover (a turbine or a reciprocating engine). When it is driving, the unit acts as a motor; when it is absorbing energy, the unit acts as a generator. The driving capability permits the researcher to determine bearing, seal, and windage losses by removing the turbine rotor, driving the shaft, and measuring the torque as a function of speed. This frictional torque is then added to the torque measured during the turbine tests in order to obtain the true turbine torque. For the smaller turbines, the friction losses may represent an appreciable percentage of the total turbine power. For the larger jet-engine type turbines, these losses are generally small when compared to the total torque output, and hence, they can often be neglected.

*Airbrake dynamometer.*—The airbrake dynamometer is a type of power absorber that was developed at the NASA Lewis Research Center. It is used extensively for testing small turbines (less than about 19 kW (25 hp)). A cross-sectional view of the airbrake dynamometer is shown in figure 12-15. The airbrake consists of a throttle valve, an inlet collector, a stator, a rotor with either a paddle wheel or airfoil type blading, and flow straighteners to ensure axial entry and discharge of the air. After the air enters the inlet collector of the airbrake in an axial direction, it is accelerated through the stator, which gives it tangential momentum in a direction opposite to the direction of rotation of the rotor. The rotor removes tangential momentum from the air and, thereby, absorbs the research turbine power output. After leaving the rotor, the air passes through flow straighteners and is discharged from the airbrake in an axial direction. Therefore, the torque on the rotor is equal to the torque on the casing. The casing is cradled in air bearings, which are designed for radial and axial loads. A torque arm is attached to the casing for measurement of torque.

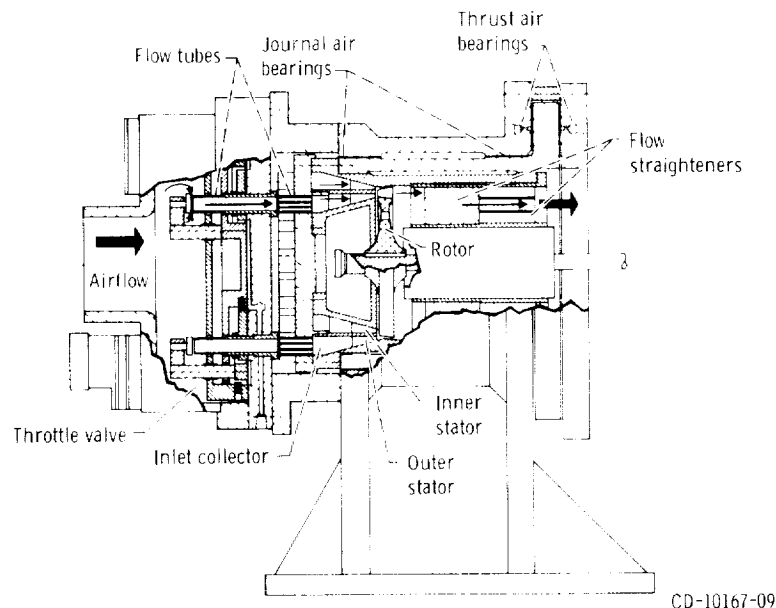


FIGURE 12-15.—Airbrake dynamometer.

It can be noted from figure 12-15 that the stator consists of two sections, an outer and an inner blade row, with independent valving for each blade row. This stator system is well adapted to measure extremely small turbine outputs at low inlet pressures. For example, a stator configuration can be used where one blade row can impart tangential momentum in the same direction of rotation as the rotor while the other stator blade row imparts tangential momentum in a direction opposite to the direction of rotation of the rotor. For this case, the rotor is of the paddle-wheel type design. Thus, the airbrake can be used to absorb turbine power or to drive the turbine. This driving capability, as was the case for the dc dynamometer, permits the measurement of bearing and seal frictional losses.

*Measurement of dynamometer force.*—The dynamometer force measurement can be obtained most simply by a spring-balance scale. Such a scale can be used because the displacements of the power absorber torque arm are very small. Because these scales indicate forces acting vertically, the torque arm should and does remain relatively horizontal, regardless of the magnitude of the force involved. The disadvantages of a spring-balance scale are that the reading is not readily remotely observable (low-power telescopes have been used), and available scales may not have the proper force range.

Hydrostatic devices with either a liquid (e.g., mercury) or a gas (e.g., air) as the fluid have been used to measure force. The principle of operation is that the force to be measured is impressed on the fluid, with the fluid being held in a confined space. The greater the force on the fluid, the greater becomes the pressure on the fluid. This fluid pressure can be calibrated in terms of the load or force required to produce it.

Most current turbine test facilities are equipped with calibrated strain-gage load cells to measure torque. These devices provide an electrical output signal which, with appropriate electronics, can provide direct torque readings on a digital voltmeter. This signal is particularly suitable for automatic digital data recording.

*Strain-gage torquemeter.*—Sometimes, in turbomachinery component testing, it is impractical to cradle the equipment as required for conventional torque measurement. The situation may arise wherein the turbine rotative speed is higher than the capability of the absorber, which would necessitate the use of an intermediate gear box. To circumvent this problem, a high-speed, strain-gage torquemeter, which operates on the principle that shaft torque and shaft surface strain are proportional, can be used. A bonded wire strain gage is mounted on the shaft, between the turbine and the power absorber. The fine wire has the property that its resistance is very nearly a unique function of the strain applied. Readings are transmitted through slip rings, onto brushes, and to appropriate electronic equipment, where the shaft torque is indicated. Problems encountered with this type of torquemeter include short brush life and the occurrence of induced voltages that interfere with the measurements.

*Optical torquemeter.*—An optical torquemeter basically consists of a shaft with polished parallel and flat reflecting surfaces at each end. A stationary optical unit measures the twist of the shaft. The optical system projects the illuminated image of a slit, by successive reflection from each of the reflecting surfaces on the shaft, onto two photocells separated by a hairline gap. Shaft twist produces unbalanced illumination on the two photocells. A servomechanism thereupon repositions the photocells to restore the null-balance condition. Photocell position is a measure of shaft twist.

Experience has indicated that the reflecting surfaces of the optical torquemeter must be kept highly polished to maintain accuracy. This may be difficult, because these surfaces are usually close to the turbine bearings and/or gearbox bearings and oil mist tends to cloud these surfaces. A higher intensity light source, such as a laser beam, may possibly facilitate accurate torque readings. The design of both the optical and the strain-gage torquemeters must provide for adequate torsional twist under load. Both systems have been operated in con-

junction with dynamometers, with good correlation. There are other types of torquemeters that are commercially available that also could be used for turbine testing.

#### **Rotative-Speed Measurement**

One of the simplest and most accurate measurements in turbine testing is that of rotative speed. The electric tachometer can be used to give a continuous indication of speed. A dc generator, with a permanent magnetic field and a rotating armature, is driven by the shaft the speed of which is to be measured. Since the field is constant, the voltage output of the generator is proportional to its speed. The usually remote indicator is a voltmeter graduated to read rotative speed.

For greater accuracy in speed measurements, a positively driven revolution counter should be used. A means is provided for engaging and disengaging it simultaneously with a timer. Commercial units, called chronotachometers, are available. These units are advantageous because they yield an average rotative speed for a given time (usually 1 minute).

The currently most accepted method of measuring speed is through the use of an electromagnetic or electronic pulse counter. It is particularly suited for high-rotative-speed machines. For this method, a sprocket with a given number of teeth is secured to the turbine shaft. An electronic pickup accurately counts the teeth (or impulses) for a given time and displays the count directly as rotative speed.

Rotative speed varies somewhat during turbine tests when the air supply pressure varies. Since mass flow rate and, therefore, power are directly proportional to pressure, an increase in supply pressure tends to drive the turbine faster. The absorber tends to correct for this, and there result accelerations and decelerations within the accuracy of the control system. It is, therefore, ideal to have a steady air supply to provide greater accuracy when taking data.

### **TURBINE PERFORMANCE**

The performance characteristics of turbines are usually presented by means of performance maps. Such a performance map shows, on one figure, the turbine flow and work as functions of the operating conditions of speed and pressure ratio. Also shown on the map are contours of efficiency. The flow, work, and speed are shown in terms of equivalent conditions so that the map can be readily used for any inlet conditions of temperature and pressure. The concept and nature of equivalent conditions are discussed in chapter 2 (vol. 1).

In brief review, the equivalent conditions are

$$w_{eq} = w \frac{\sqrt{\theta}}{\delta} \epsilon \quad (12-7)$$

$$\Delta h'_{eq} = \frac{\Delta h'}{\theta} \quad (12-8)$$

and

$$N_{eq} = \frac{N}{\sqrt{\theta}} \quad (12-9)$$

where the subscript *eq* refers to the equivalent condition. The correction factors are defined as

$$\theta = \left( \frac{V_{cr,0}}{V_{cr,std}} \right)^2 \quad (12-10)$$

$$\delta = \frac{p'_0}{p'_{std}} \quad (12-11)$$

and

$$\epsilon = \frac{\gamma_{std} \left( \frac{2}{\gamma_{std} + 1} \right)^{\gamma_{std}/(\gamma_{std}-1)}}{\gamma \left( \frac{2}{\gamma + 1} \right)^{\gamma/(\gamma-1)}} \quad (12-12)$$

where the square of the critical velocity  $V_{cr}$  is

$$V_{cr}^2 = \frac{2\gamma}{\gamma+1} gRT' \quad (12-13)$$

The subscript *std* refers to the standard sea-level air conditions of pressure (10.133 N/cm<sup>2</sup> or 14.696 psia), temperature (288.2 K or 518.7° R), molecular weight (29.0), and specific heat ratio (1.4).

An example performance map is presented in figure 12-16. Equivalent specific work is plotted against the product of the equivalent mass flow and the equivalent rotative speed. This product conveniently spreads out the data because, as will be shown in the discussion to follow, there may be little or no variation in the mass flow rate with variations in rotative speed. Lines of constant pressure ratio (total pressure ratio in this case) and constant speed are presented on the map. Also, contours of efficiency are included for completeness.

Although a great deal of information can be obtained from the performance map, a better understanding of the turbine performance can be obtained if some of the performance parameters are plotted independently as functions of pressure ratio for a range of speed. The curves of this type to be presented in the following sections are not

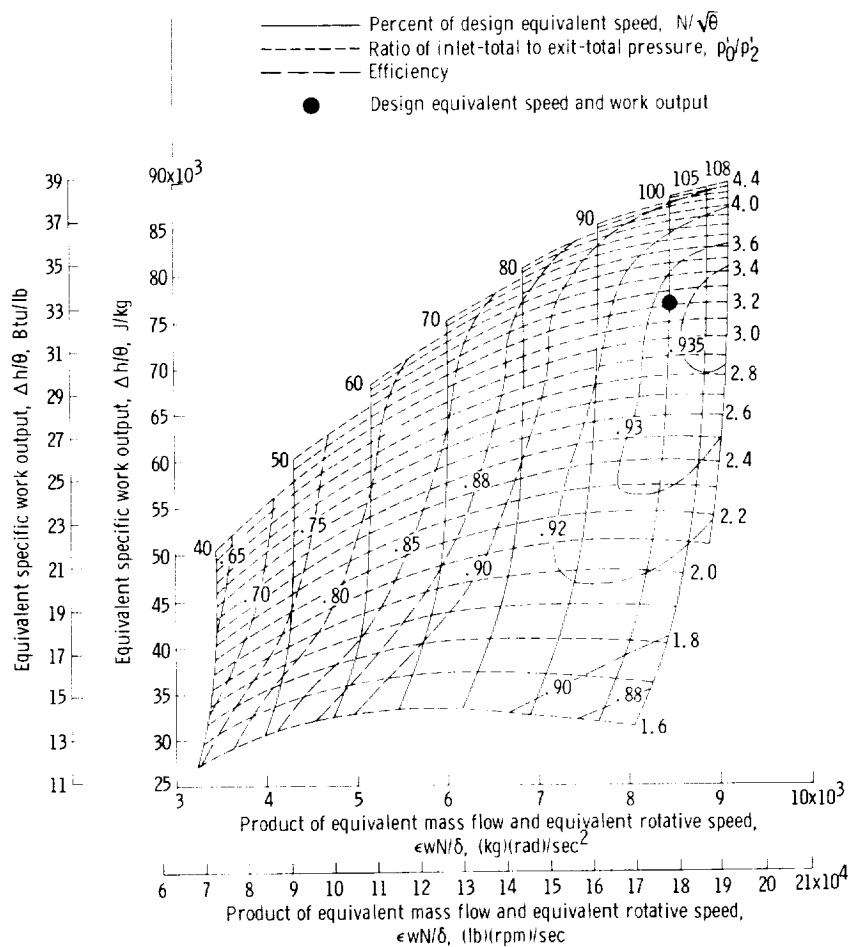


FIGURE 12-16.—Turbine performance map.

for the same turbine whose map is shown in figure 12-16, but were selected to illustrate certain points.

#### Mass Flow

Variations in mass flow rate with turbine pressure ratio and speed are shown in figures 12-17 and 12-18 for a single-stage turbine operated with two different stators. Figure 12-17 was obtained with a stator having a large stagger angle (small stator-throat area), and figure 12-18 was obtained with a stator having a small stagger angle

## EXPERIMENTAL DETERMINATION OF AERODYNAMIC PERFORMANCE

(large stator-throat area). For both cases, the stator blades were identical, and the same rotor was used.

In both figures it can be seen that for a given speed, the mass flow rate increases as the pressure ratio increases until some maximum value is reached. A further increase in pressure ratio produces no increase in mass flow. The reason for this maximum in mass flow is that either the stator or the rotor has choked.

In figure 12-17, which is for the small stator-throat area, the maximum value of mass flow rate is unaffected by the rotational speed; this indicates that the stator is choked. In figure 12-18, the maximum mass flow rate is influenced by the rotational speed, which indicates that the rotor is choked. For the case of the choked rotor, the maximum mass flow rate increases with decreasing rotational speed. This is the usual behavior and is due to an increase in the rotor inlet relative total pressure with decreasing speed. In some cases, however, the occurrence of very large incidence losses causes a decrease in maximum flow with decreasing speed.

The foregoing discussion has been for the case of a single-stage turbine. In a multistage turbine, the flow variation shown in figure 12-17 would indicate a first-stage stator choke. A flow variation of

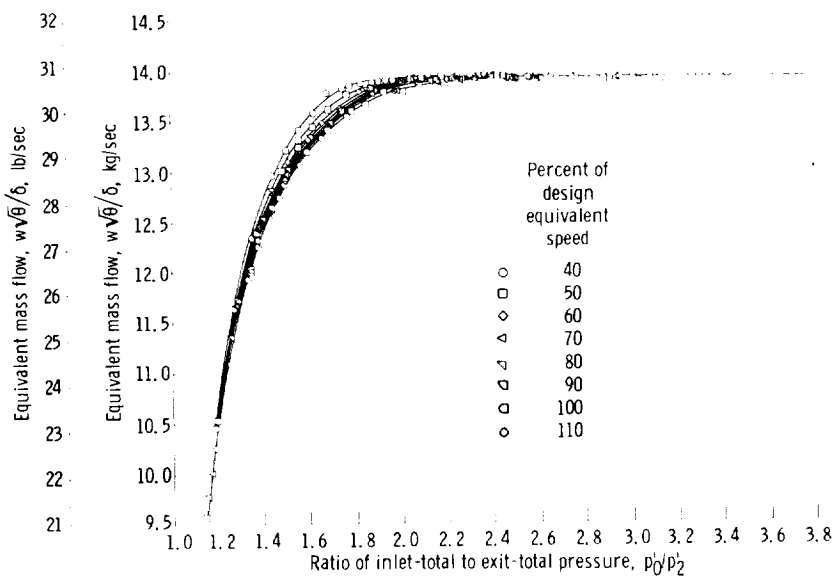


FIGURE 12-17.—Variation of equivalent mass flow with total-pressure ratio for turbine with small stator-throat area.

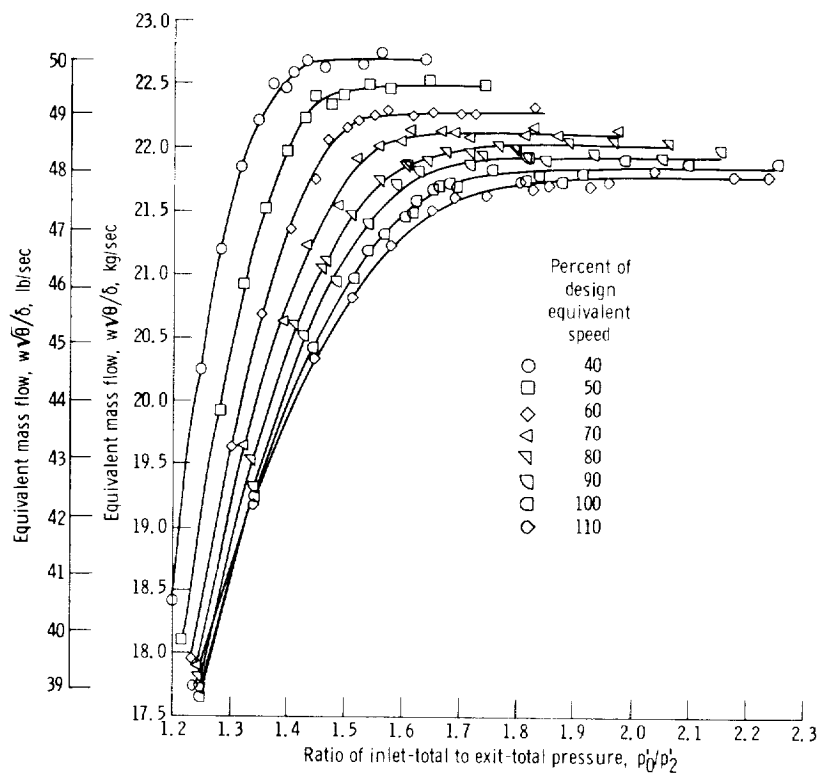


FIGURE 12-18.—Variation of equivalent mass flow with total-pressure ratio for turbine with large stator-throat area.

the type shown in figure 12-18 would indicate choking in some downstream blade row, either a rotor or a stator. To determine exactly where this choking occurred, static-pressure measurements between the blade rows would have to be obtained. Such data are illustrated in figure 12-19, where the variation in hub static pressure with turbine pressure ratio (at constant speed) is shown for each blade row exit of a two-stage turbine. As the turbine pressure ratio increases, choking in any given blade row is indicated by the static pressure upstream of that blade row remaining constant while the downstream static pressure continues to decrease. For the particular case illustrated in figure 12-19, choking occurs first in the second stator at a turbine pressure ratio of about 3.2. As turbine pressure ratio continues to increase, the second rotor then chokes at a turbine pressure ratio of about 3.7. It is, of course, the first choke that establishes the maximum flow rate for the turbine.

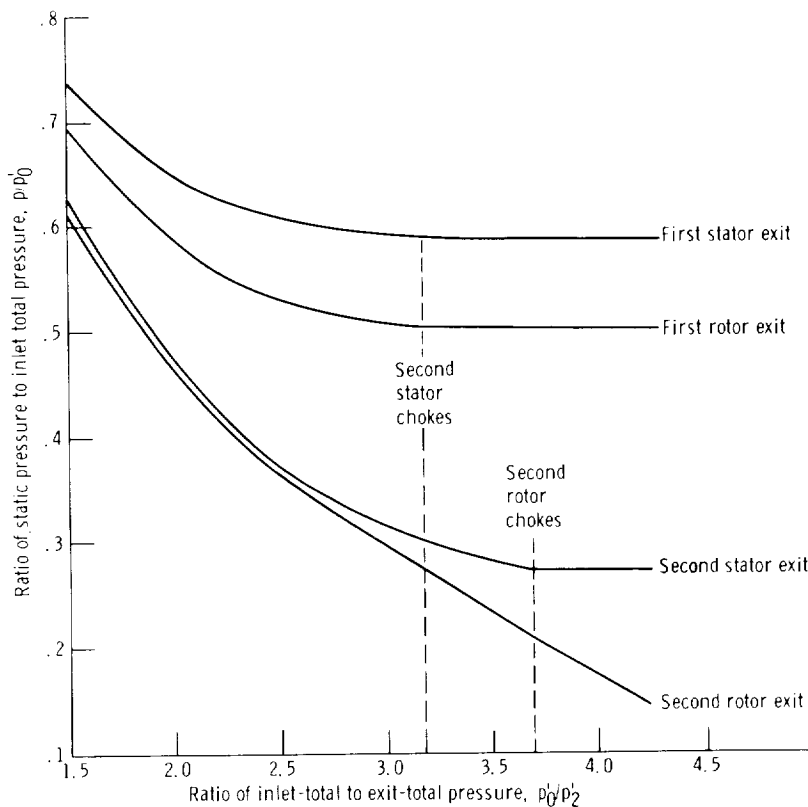


FIGURE 12-19.—Effect of turbine total-pressure ratio on hub static pressure in a two-stage turbine.

### Torque

As indicated by equation (2-9) of chapter 2 (vol. 1), the torque should vary directly with the mass flow rate and with the change in tangential component of absolute velocity ( $\Delta V_u$ ) between rotor inlet and exit for any constant radius. The manner in which torque varies experimentally with turbine pressure ratio and speed is shown in figure 12-20. For a given speed, increasing the pressure ratio increases the torque due to a higher mass flow rate and higher values of  $\Delta V_u$  resulting from the high velocities and increased turning (absolute) in the rotor. At a given pressure ratio, the torque decreases with increasing speed. This is due to a decrease in the amount of turning in the rotor (exit absolute flow angle becomes more positive as speed increases) and a possible decrease in mass flow rate.

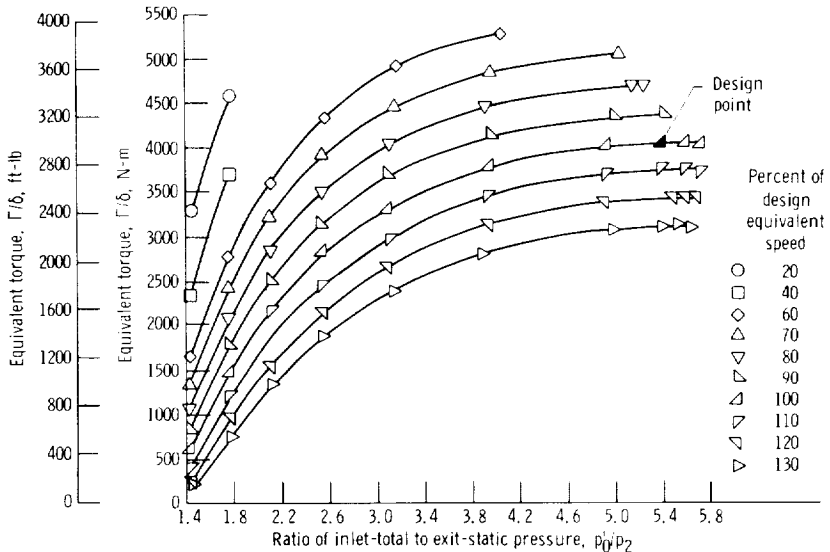


FIGURE 12-20.—Variation of equivalent torque with turbine pressure ratio and speed.

Figure 12-20 shows that as the pressure ratio increases for a given speed, the torque tends to level off and reach a maximum value. Above this limit, any further increase in pressure ratio results in no additional torque. This phenomenon is termed "limiting loading" and is indicated on a performance map by the lines of constant pressure ratio converging to yield a maximum value of equivalent specific work for each speed. In figure 12-16, limiting loading is being approached but has not been reached. Limiting loading occurs when the annulus area at the turbine exit is choked; that is, when the exit axial Mach number is unity.

The mass flow and torque curves just discussed can be plotted from measured data. These curves are then used to construct the turbine performance map. The usual procedure in constructing a performance map is to select the mass flow and torque at even increments of pressure ratio for the various speeds. Specific work, ideal specific work, and efficiency are then calculated, and the performance map can be drawn.

### Efficiency

Another convenient and widely used method of presenting turbine

## EXPERIMENTAL DETERMINATION OF AERODYNAMIC PERFORMANCE

performance is to plot efficiency as a function of blade-jet speed ratio  $\nu$ , which is given by the equation

$$\nu = \frac{U}{\sqrt{2gJ\Delta h_{id}}} \quad (12-14)$$

where

$U$  blade mean-section speed, m/sec; ft/sec

$\Delta h_{id}$  ideal specific work based on ratio of inlet-total to exit-static pressure, J/kg; Btu/lb

This was discussed in chapter 2 (vol. 1), where a correlation was shown mathematically for an idealized case. For that case, efficiency was shown to vary parabolically with blade-jet speed ratio.

Experimentally obtained static efficiencies are plotted against blade-jet speed ratio in figure 12-21 for a two-stage axial-flow turbine over a

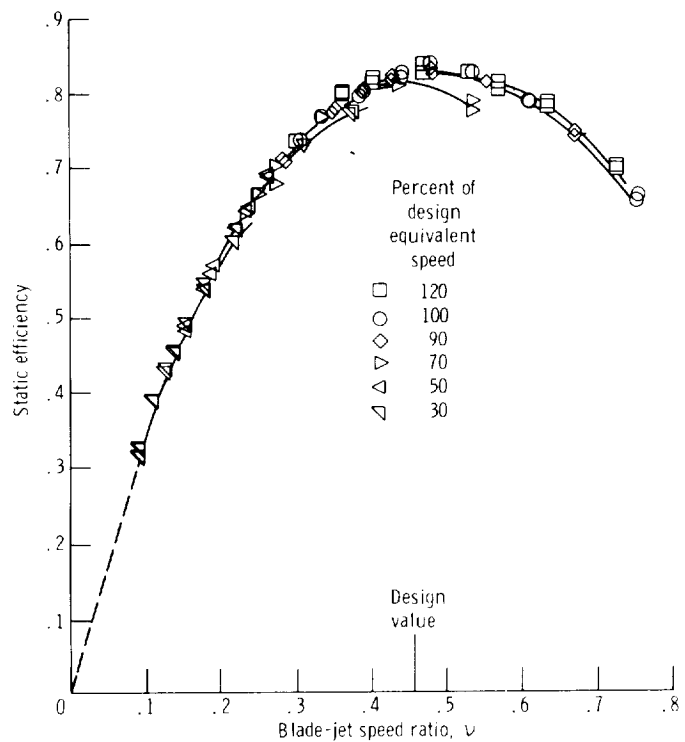


FIGURE 12-21.—Variation of efficiency with blade-jet speed ratio.

wide range of speed and pressure ratio. The total efficiencies for this turbine, because of the two stages and very low exit velocities, were only very slightly (1 or 2 percent) higher than the static efficiencies and are, therefore, not presented. Figure 12-21 shows that the blade-jet speed ratio serves very well to correlate turbine efficiency in a generalized manner for a real turbine as well as for an ideal turbine. It should be noted, however, that the correlation is not always as good as for the turbine represented by this figure. For operating conditions where limiting loading is approached, the speed lines tend to separate somewhat, especially at the lower blade-jet speed ratios.

### Flow Angles

Although flow angles are not considered as turbine performance parameters, we should understand how they vary over the turbine

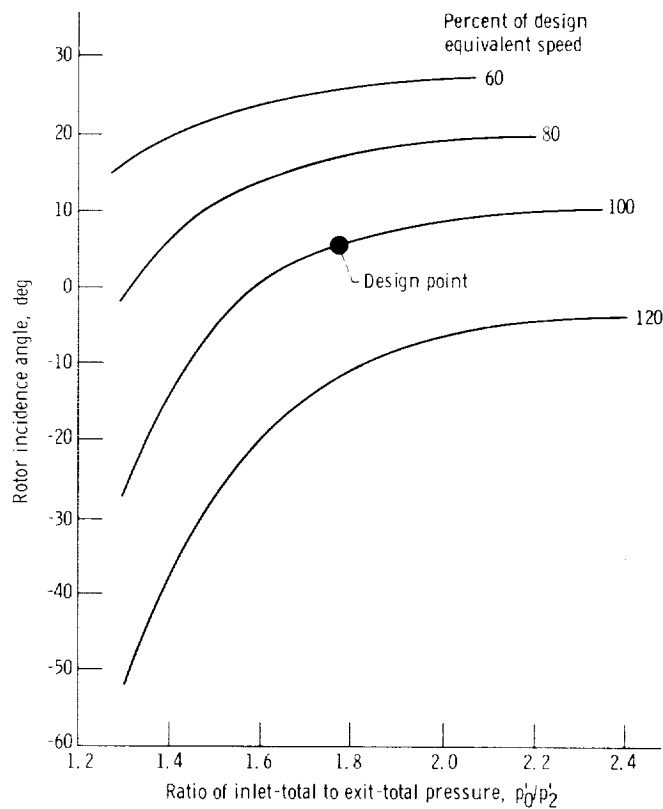


FIGURE 12-22.—Variation of rotor incidence angle with turbine pressure ratio and speed.

operating conditions. The direction of the flow entering each blade row determines the incidence loss, which is an important contributor to off-design losses, as discussed in chapter 8 (vol. 2). The rotor incidence angle, which is defined as the difference between the rotor-inlet relative flow angle and the rotor blade inlet angle, was calculated over a range of speed and pressure ratio for a typical single-stage turbine, and the resultant values are presented in figure 12-22. Flow angles are herein defined as being positive when the tangential component of the velocity vector is in the same direction as the blade velocity. The following generalized observations can be made from this figure: (1) a large variation in incidence angle occurs over the potential operating range of a turbine, (2) the change in incidence angle

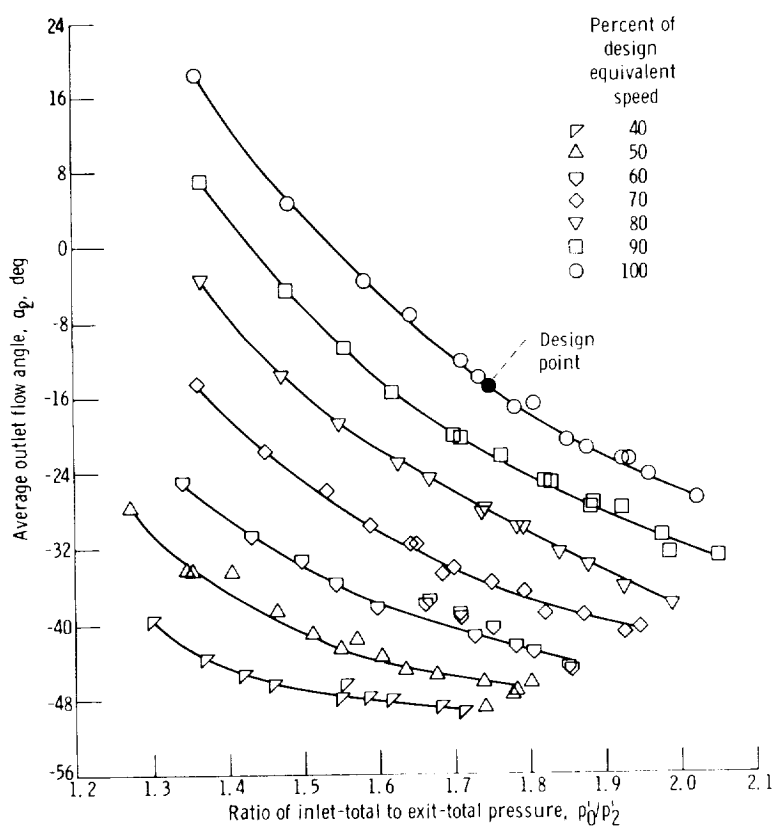


FIGURE 12-23.—Variation of outlet flow angle with turbine pressure ratio and speed.

with pressure ratio becomes greater as speed increases, and (3) the rotor incidence angle becomes more positive as the pressure ratio increases and speed decreases.

The turbine outlet flow angle is important with respect to the design of whatever component may be downstream of the turbine or to the amount of thrust that can be obtained from the outlet flow. Outlet flow angle is plotted over a range of speed and pressure ratio in figure 12-23 for the same single-stage turbine referred to in the last paragraph. The trends observed and generalizations made for the incidence angle also apply to the outlet flow angle, the only difference being that the change in outlet flow angle with pressure ratio and speed is in the direction opposite to that for rotor incidence angle.

### Stator Loss

Stator loss is directly measurable in terms of total pressure by means of a total-pressure probe and survey equipment such as that previously shown in figures 12-7 and 12-8. A typical circumferential total-pressure loss survey taken at one radius just behind the stator trailing edge is shown in figure 12-24. It can be plainly seen that all of the loss occurs in the wake region. A composite of many such circumferential traces yields contours of stator total-pressure ratio such as shown in figure 12-25. The majority of the traces were concentrated near the hub and tip regions, where measurements were greatly affected by the end-wall boundary layers. The increased pressure loss with increasing critical velocity ratio (and flow) and the end-wall boundary-layer buildup can be noted. The total-pressure loss data can be converted to kinetic-energy loss coefficients as described in chapter 7 (vol. 2). Integration of the losses over the area of one full passage gives the total loss for the stator. Once the turbine and stator perform-

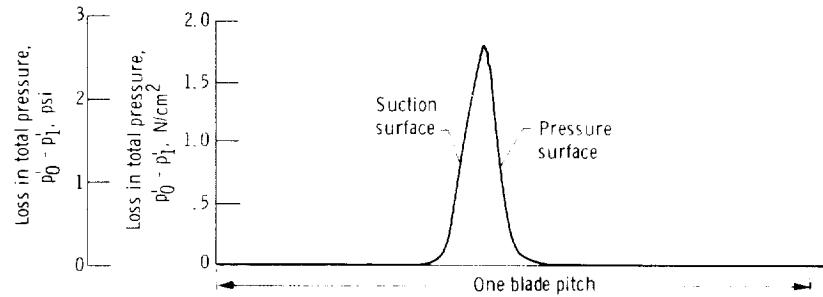


FIGURE 12-24.—Typical total-pressure loss survey data at blade exit.

## EXPERIMENTAL DETERMINATION OF AERODYNAMIC PERFORMANCE

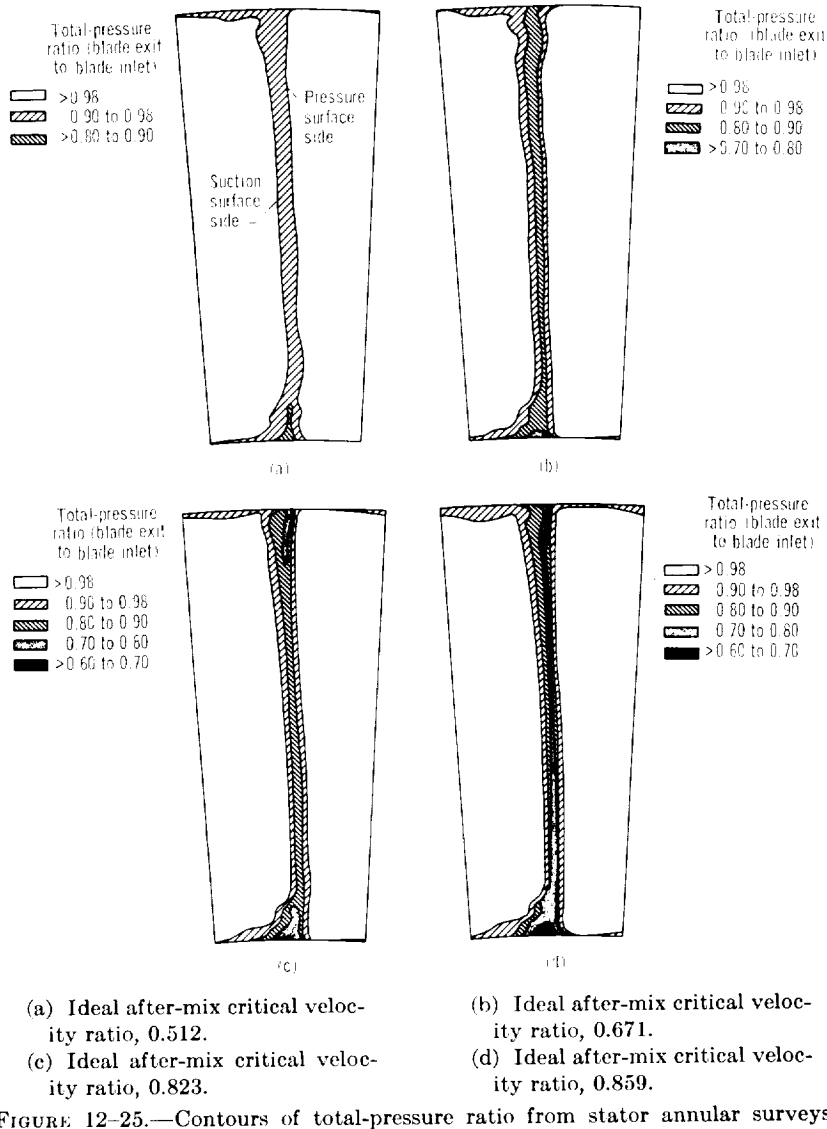


FIGURE 12-25.—Contours of total-pressure ratio from stator annular surveys.

ance have been obtained experimentally, a turbine loss breakdown can be made.

### Surface Velocity

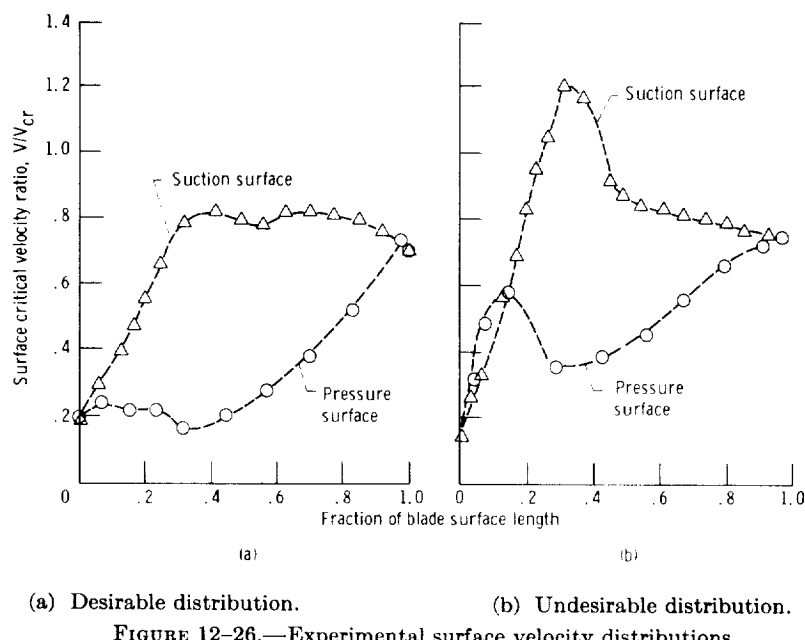
An important part of the blading design is the selection of the blade surface profiles that yield favorable surface velocity distributions.

Analytical methods for calculating surface velocities were discussed in chapter 5 (vol. 2). During the test program, it is of interest to determine whether the "designed for" surface velocities were actually achieved. To obtain the velocity distribution along a blade surface, static-pressure measurements are made along the blade surfaces in the manner discussed previously in the section on static-pressure measurements. With the static pressure distribution along the blade surfaces known, the velocity distribution can be determined from the relation

$$\frac{V}{V_{cr}} = \left\{ \frac{\gamma+1}{\gamma-1} \left[ 1 - \left( \frac{p}{p_0} \right)^{(\gamma-1)/\gamma} \right] \right\}^{1/2} \quad (12-15)$$

Figure 12-26 shows the experimentally determined surface velocity distributions for two stators tested under similar conditions. The distribution shown in figure 12-26(a) is considered to be a desirable one. Acceleration on the suction surface to the maximum velocity is smooth, and the maximum velocity is maintained subsonic. There are no large flow decelerations (diffusions) on either surface. The loading (force on blade) is well distributed along the blade.

Figure 12-26(b), on the other hand, shows a velocity distribution considered to be undesirable. Flow on the suction surface accelerates



(a) Desirable distribution.

(b) Undesirable distribution.

FIGURE 12-26.—Experimental surface velocity distributions.

## EXPERIMENTAL DETERMINATION OF AERODYNAMIC PERFORMANCE

to a supersonic velocity ( $V/V_{cr}=1.2$ ) and then undergoes a rapid deceleration back to a subsonic velocity. Such a deceleration causes a thickening of the boundary layer with an associated increase in loss and could possibly lead to separation of the flow off the suction surface. A deceleration is also observed on the pressure surface, but this is not as critical, because it is followed by an acceleration that would result in reattachment of any separated flow. In general, velocity distributions with sharp peaks and valleys should be avoided when the blades are being designed.

## REFERENCES

1. DOEBELIN, ERNEST O.: Measurement Systems: Application and Design. McGraw-Hill Book Co., 1966.
2. FUTRAL, SAMUEL M.; KOFSKEY, MILTON; AND ROHLIK, HAROLD E.: Instrumentation Used to Define Performance of Small Size, Low Power Gas Turbines. Paper 69-GT-104, ASME, Mar. 1969.
3. MOFFITT, THOMAS P.; PRUST, HERMAN W.; AND SCHUM, HAROLD J.: Some Measurement Problems Encountered When Determining the Performance of Certain Turbine Stator Blades from Total Pressure Surveys. Paper 69-GT-103, ASME, Mar. 1969.
4. WISLER, D. C.; AND MOSSEY, P. W.: Gas Velocity Measurements Within a Compressor Rotor Passage Using the Laser Doppler Velocimeter. Paper 72-WA/GT-2, ASME, Nov. 1972.
5. ASME RESEARCH COMMITTEE ON FLUID METERS: Fluid Meters, Their Theory and Application, 5th ed., The American Society of Mechanical Engineers, 1959.

## SYMBOLS

<i>A</i>	area, m <sup>2</sup> ; ft <sup>2</sup>
<i>C</i>	discharge coefficient
<i>D</i>	diameter, m; ft
<i>E</i>	thermal expansion factor
<i>g</i>	conversion constant, 1; 32.17 (lbm)(ft)/(lbf)(sec <sup>2</sup> )
$\Delta h_{id}$	ideal specific work based on ratio of inlet-total to exit-static pressure, J/kg; Btu/lb
$\Delta h'$	turbine specific work, J/kg; Btu/lb
<i>J</i>	conversion constant, 1; 778 (ft)(lb)/Btu
<i>K</i>	conversion constant, 1; $\pi/30$ (rad)(min)/(rev)(sec)
<i>M</i>	approach velocity factor, defined by eq. (12-4)
<i>N</i>	rotative speed, rad/sec; rev/min
<i>p</i>	absolute pressure, N/m <sup>2</sup> ; lb/ft <sup>2</sup>
<i>R</i>	gas constant, J/(kg)(K); (ft)(lbf)/(lbm)(°R)
<i>T</i>	absolute temperature, K; °R
<i>U</i>	blade mean-section speed, m/sec; ft/sec
<i>V</i>	absolute gas velocity, m/sec; ft/sec
$\Delta V_u$	change in tangential component of absolute velocity between rotor inlet and exit, m/sec; ft/sec
<i>w</i>	mass flow rate, kg/sec; lb/sec
<i>Y</i>	compressibility factor, defined by eq. (12-5) or (12-6)
<i>a</i>	absolute flow angle, measured from axial direction, deg
$\Gamma$	torque, N-m; lb-ft
$\gamma$	ratio of specific heat at constant pressure to specific heat at constant volume
$\delta$	ratio of turbine-inlet total pressure to standard sea-level pressure
$\epsilon$	function of specific-heat ratio, defined by eq. (12-12)
$\theta$	squared ratio of critical velocity based on turbine-inlet temperature to critical velocity based on standard sea-level temperature, defined by eqs. (12-10) and (12-13)
$\nu$	blade-jet speed ratio, defined by eq. (12-14)
$\rho$	density, kg/m <sup>3</sup> ; lb/ft <sup>3</sup>

## Subscripts:

<i>an</i>	annulus
<i>cr</i>	critical condition (at Mach 1)
<i>eq</i>	equivalent
<i>in</i>	meter inlet
<i>std</i>	standard sea-level condition
<i>t</i>	meter throat
0	measuring station at turbine inlet

EXPERIMENTAL DETERMINATION OF AERODYNAMIC PERFORMANCE

1        measuring station at stator outlet  
2        measuring station at turbine outlet

Superscript:

'        absolute total state

